VACUUM ULTRAVIOLET ABSORPTION MEASUREMENTS OF ATOMIC OXYGEN IN A SHOCK TUBE

A DISSERTATION
SUBMITTED TO THE DEPARTMENT OF AERONAUTICS AND ASTRONAUTICS
AND THE COMMITTEE ON GRADUATE STUDIES
OF STANFORD UNIVERSITY
IN PARTIAL FULFILLMENT OF THE REQUIREMENTS
FOR THE DEGREE OF
DOCTOR OF PHILOSOPHY

Scott Andrew Meyer
December 1995

I certify that I have read this dissertation and that in my opinion it is fully adequate, in scope and quality, as a dissertation for the degree of Doctor of Philosophy.

Prof. Daniel Bershader

I certify that I have read this dissertation and that in my opinion it is fully adequate, in scope and quality, as a dissertation for the degree of Doctor of Philosophy.

Prof. Donald Baganoff

I certify that I have read this dissertation and that in my opinion it is fully adequate, in scope and quality, as a dissertation for the degree of Doctor of Philosophy.

Prof. Ronald K. Hanson

I certify that I have read this dissertation and that in my opinion it is fully adequate, in scope and quality, as a dissertation for the degree of Doctor of Philosophy.

Dr. Surendra P. Sharma

Approved for the University Committee on Graduate Studies.

Abstract

The absorption of vacuum ultraviolet light by atomic oxygen has been measured in the Electric Arc-driven Shock Tube (EAST) Facility at NASA-Ames Research Center. This investigation demonstrates the instrumentation required to determine atomic oxygen concentrations from absorption measurements in impulse facilities. A shock wave dissociates molecular oxygen, producing a high temperature sample of atomic oxygen in the shock tube. A probe beam is generated with a Raman-shifted ArF excimer laser. By suitable tuning of the laser, absorption is measured over a range of wavelengths in the region of the atomic line at 130.49 nm. The line shape function is determined from measurements at atomic oxygen densities of 3×10^{17} and 9×10^{17} cm^{-3}. The broadening coefficient for resonance interactions is deduced from this data, and this value is in accord with available theoretical models.

Acknowledgements

I would like to thank Prof. Daniel Bershader for providing the opportunity to perform this research. The sudden loss of Prof. Bershader saddened the friends and colleagues he left behind, and he will be remembered not only for his contributions to aerophysics, but for his love of teaching. I would also like to thank the rest of the department and my reading committee for their help in completing this thesis. I am especially grateful to Prof. Donald Baganoff for his assistance in the final stages of my work.

This research was performed under Interchange Numbers NCA2-494 and NCA2-273 at the NASA-Ames Research Center, and I am grateful to many friends and colleagues there. I am grateful to my main collaborator at Ames, Dr. Surendra Sharma, who encouraged this research and worked to maintain support for it in a difficult environment. I am indebted to Richard Exberger for his assistance with the experimental hardware and to William Warren for operation of the shock tube and his expertise with vacuum systems. Thanks to my fellow students, Walt Gillespie, for blazing a trail before me, and John Gilmore, for help with my experiments. Many others took time to help me, especially within the Reacting Flow Environments Branch. I am especially grateful for the assistance of Doug Fletcher with the ArF laser, Ellis Whiting with radiative transport calculations, Greg Wilson for boundary layer calculations, and to Chul Park and Winifred Huo for discussions on line broadening. Mark Dyer and Dave Huestis of SRI International graciously loaned a Raman cell for preliminary work, and Mark provided invaluable advice for Raman-shifting into the VUV.

I am happy to have family and friends to thank for their support during this process. Thanks to my friends from campus and from Ames, the "Watson clan," the 9:15 group, and many terrific teachers. Thanks to Jen for listening, Mark for commiserating, Eric for his enthusiasm, to Mom, Pat and Cara for their patience, and to Dad for his encouragement. Most importantly, my undying thanks and admiration to Crystal:

You are truly unbelievable.

Table of Contents

List of Figures

List of Tables

Chapter 1
Introduction

Chemical reactions involving oxygen are vital to many important processes. Oxygen consumption via respiration powers most life, and replenishment occurs through photosynthesis in plants. Interaction of oxygen with sunlight is a driving force in atmospheric chemistry and atmospheric dynamics, and ozone produced in the upper atmosphere absorbs potentially harmful ultraviolet light before it reaches Earth's surface. Many industrial processes as well, such as combustion, rely on oxygen. Details of these processes, and their interdependence, are active fields of research.

Despite their importance, reactions involving oxygen are not always easy to study. Oxygen is sometimes difficult to detect directly because it is colorless, even when evidence for its presence is clear. Advances in spectroscopy, however, have shown that oxygen is not always "colorless" to laboratory devices. Under certain conditions, oxygen interacts with light in unique and predictable ways, rendering it visible. For example, atomic oxygen absorbs specific wavelengths of vacuum ultraviolet (VUV) light very strongly. The presence of atomic oxygen can be detected by a measurement of this absorption. A further characterization of this absorption and the development of equipment required to measure this absorption are the subject of this study.

1.1 Thermochemistry in hypervelocity flight

Chemical reactions involving oxygen are important in hypervelocity flight. Various processes involving conversion between chemical and thermal energy in a flowfield are collected under the heading of thermochemical effects. These effects can be put into perspective by understanding how they arise and how they are modeled.

The interaction of a moving body with the air around it depends on its speed. Air resistance is negligible for a hammer dropped to the floor, but not for a curveball which is

moving faster. As speed increases, compressibility of air becomes important. The mass and momentum conservation equations are coupled to the energy conservation equation by equations of state. Simple relations for an ideal gas are remarkably successful, and the resulting equations are valid for supersonic as well as subsonic flows.

At even higher speeds, typical of transatmospheric flight and meteors, the chemical structure of air is important. Stagnation temperatures are tremendous, and additional internal energy modes, like vibrational and electronic energy, become active. Nitrogen and oxygen molecules dissociate, ionize, and form radical molecules. Clearly, the ideal state equations must be replaced with a more detailed model.

This model is complicated by the finite rates at which thermochemical changes occur. The time required for a certain change, such as dissociation or vibrational excitation, is typified by a "characteristic time." Collisions driving the processes are less frequent at high altitudes where the air is thin, and this increases characteristic times. The flowfield around a body is also described by a characteristic time, the "flow residence" time. Flow residence time is loosely defined as the time required for a particle to traverse a significant portion of the flowfield.

The importance of finite rates is assessed by comparing characteristic times for the processes to flow residence time. A typical process is redistribution of vibrational energy, called vibrational relaxation. If the flow residence time is much greater than the characteristic time for vibrational relaxation, then the rate of vibrational relaxation is not important, and vibrational energy can be predicted from other properties at that point (Boltzmann distribution). On the other hand, if the flow residence time is much less than the vibrational relaxation time, then vibrational energy is "frozen" at its upstream value. In the most complicated situation, the two time scales are of the same order. Vibrational energy of a molecule then depends not only on local conditions, but also on the molecule's history: where the molecule came from and what the vibrational relaxation rates were. Note that characteristic times for different processes can be dramatically different. For example, rotational levels may be in a Boltzmann distribution at the local temperature even if the vibrational population distribution is frozen.

For aerothermodynamic problems, there are three possible situations. In the first, the flow property is defined at a point, and a Boltzmann distribution of states is appropriate. In the second, the flow property is "frozen" at an upstream value, and so is a constant through the flow. In the third, the finite rates and the flow equations are coupled, and they must be solved together. Rates for the various properties must be known to solve the coupled equations. However, before assuming the property can be found from a

Boltzmann distribution or a frozen value, the rates must at least be *estimated* to verify that the chosen model is valid.

Atomic oxygen is important in reacting flowfields for several reasons:

1) Molecular oxygen has a binding energy of only 5.1 eV. Dissociation into atoms occurs for even low atmospheric entry speeds.
2) Oxygen atoms may recombine in the expansion regions around a body, converting chemical energy back into thermal energy.
3) Oxygen atoms may also recombine at the surface of the body. Chemical energy is then transferred to the body, increasing the heating load.
4) The radiative properties of atomic oxygen are very different from those of molecular oxygen. The distribution of atomic oxygen directly affects radiative heat transfer within the flowfield and heat load to the body.

Thus, experimental analysis of oxygen thermochemistry is important for accurate modeling of hypersonic flowfields. Experimental approaches for studying this chemistry depend on the properties of oxygen atoms, which are reviewed below.

1.2 Properties of atomic oxygen

The physical properties of oxygen are well established. The nucleus is composed of eight protons and eight neutrons, producing an atomic mass of 16. The ground state electron configuration is $1s^2 2s^2 2p^4$. Four valence electrons can be arranged in fifteen different combinations, leading to ^1D, ^3P, and ^1S states. The ^3P is the lowest of the three energy levels. Spin splitting of the ^3P state yields three sublevels j=2, 1, 0. These features are shown in the Grotrian diagram, Fig. 1.1.

No visible wavelength transitions are dipole-allowed from the ground state. Transitions to ^1D and ^1S are not allowed because they are formed from the same electron configuration. The lowest energy transition promotes a 2p electron to n=3, into the $2p^3 3s\,^3S^o$ level at 76795 cm^{-1}. This transition produces the 130.2-130.6 nm triplet in the vacuum ultraviolet.

Visible transitions are observed only under special circumstances. For example, the forbidden transition ^3P - ^1D can be observed with extremely long path lengths. At high temperatures, visible transitions occur between different excited levels. Emission spectra recorded in this study exhibit some of these transitions. For ordinary conditions, however, oxygen appears "colorless."

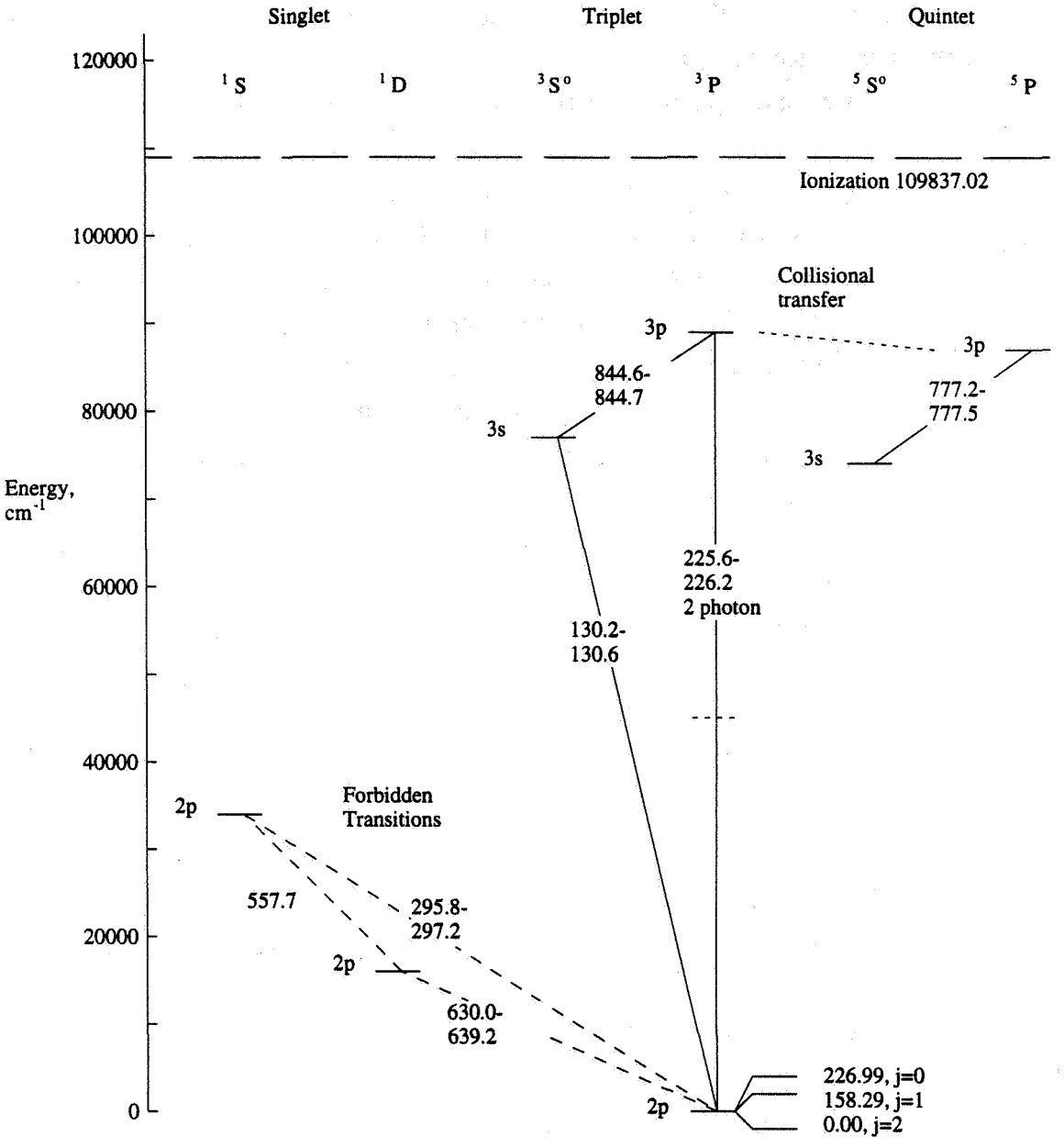

Figure 1.1 Partial energy level diagram for atomic oxygen showing relevant transitions for optical diagnostics. Transition wavelengths are in nm, and energies are in wavenumbers, cm^{-1}. A 200 nm photon has an energy of 50,000 cm^{-1}, or 6.2 eV.

1.3 Literature review

The atomic absorption measurements outlined in the next section are an important first step in developing this technique as a concentration diagnostic for ground state oxygen atoms. Before proceeding, however, various atomic oxygen detection schemes are reviewed

below, followed by a review of the vacuum ultraviolet generation technique employed here, stimulated Raman scattering.

1.3.1 Oxygen atom detection

Many optical diagnostics have been developed to measure atomic oxygen number density. Improvements have come from advances in both technology and in understanding of the relevant physical phenomena. The emergence of monochromatic laser sources, especially tunable lasers, revolutionized optical diagnostics. Simultaneously, models of phenomena such as collisional quenching, line broadening, and nonlinear mixing have been developed to interpret newly available data. Demonstrated techniques are described below, and are summarized in Table 1.1.

Recording spontaneous emission from excited states is perhaps the simplest technique to measure the concentration of atomic oxygen, although not always the most accurate. Oxygen atoms in excited states spontaneously emit photons as they decay to lower energy levels. The absolute intensity of line radiation is measured, and the population of excited states can be deduced given transition probabilities (Einstein A coefficients) of the transitions observed. If the line is not optically thin, then re-absorption must be included in the analysis.

Excited state populations can be related to the ground state population in one of two ways. The fraction of oxygen atoms in the excited state may be described by an electronic excitation temperature, which is equal to the translational temperature in thermodynamic equilibrium. The Boltzmann fraction for the excited state is then used to calculate the total oxygen number density. Alternatively, rate equations for excitation and de-excitation of the state may be solved to determine the fraction in that excited state. Both types of calculations can be performed with the NEQAIR5 code described later. The success of this technique hinges on the accuracy of transition probabilities for highly excited states and on knowledge of excitation temperature and/or rates.

Atomic resonance absorption spectroscopy (ARAS) is still commonly applied to measure oxygen number density (for example, Pamidimukkala, *et al*, 1981, Fujii, *et al*, 1989, and Patterson, *et al*, 1989). Line-of-sight absorption at 130 nm is measured with a microwave discharge lamp as the light source. Lamps typically operate with oxygen diluted in helium at a pressure of 1-5 torr to minimize self-absorption. Oxygen emission lines of the lamp are Doppler broadened at temperatures around 700 K. Pamidimukkala, *et al* (1981) measured emission lineshapes at high-resolution to derive calibration curves. More commonly, however, absorption measurements on oxygen at known temperatures and concentrations provide calibration standards.

This technique suffers from two major drawbacks. First, it is limited to low concentrations of oxygen in bath gases such as argon or helium. For example, Pamidimukkala, *et al*, (1981) report 95% absorption by 10^{14} cm^{-3} of atomic oxygen over a 7.5 cm path. Second, other species in the test gas can contaminate the measurement if they exhibit significant absorption at the resonance wavelengths. Noble gases, such as argon and helium, are common bath gases because they are transparent at 130 nm.

Three different techniques proposed for monitoring ground state populations with visible lasers have emerged from General Motors Research Laboratories: Spontaneous Raman scattering (Dasch and Bechtel, 1981), coherent anti-Stokes spectroscopy, CARS, (Teets and Bechtel, 1981), and intracavity absorption (Harris and Weiner, 1981). Both spontaneous Raman and CARS transitions are observed between the various j-levels of the ground state, $2p^4\,{}^3P$. In both cases, the spectra also show rotational Raman from O_2. Atomic and molecular components are spaced about 3 cm^{-1} apart and 230 cm^{-1} from the laser line. The required resolution and stray light rejection may be difficult to achieve in a transient facility.

The third technique, intracavity absorption, enhances absorption of the forbidden lines at 630 nm. A flow cell is placed inside the cavity of a dye laser. The presence of weak absorption introduces a loss within the laser cavity, resulting in a measurable drop in laser power at the absorption wavelength. The dye laser is not mode-locked, so a high resolution spectrometer is required to scan the laser emission for the absorption. If a cw laser is used, then temporally-resolved measurements may be possible. Depending on the strength of absorption, the output power of a mode-locked dye or diode laser with an external cavity might be monitored without a spectrometer.

Bischel, *et al* (1981, 1982) report two-photon LIF on the $2p\,{}^3P - 3p\,{}^3P$ transition. The upper state for this transition is 88630 cm^{-1} above the ground state. The upper state is accessed with two photons at 226 nm, so a VUV source is not required. The upper state population is monitored with fluorescence at 845 nm or, after collisional transfer to $3p\,{}^5P$, fluorescence at 777 nm. Alternatively, absorption of a third photon results in ionization which can be detected as well (Bamford, *et al*, 1986). In some cases the excitation is sufficient to produce a population inversion on the 845 nm transition, opening up the possibility of coherent techniques (amplified spontaneous emission, stimulated gain). An excellent overview is given by Westblom, et al (1990); Brown and Jeffries (1995) recently reported atomic concentrations deduced from stimulated gain measurements. Two-photon excitation occurs within the focal volume of the pump laser, so the technique offers good spatial resolution. Finally, interference from other species in the VUV is not an issue.

Quantitative measurements are possible if several important effects can be accounted for and if adequate signals are available. The two-photon pumping rate depends on the spatial and temporal properties of the beam as well as on the beam energy. Careful measurements of the pumping rate agree with calculations based on *ab initio* cross-sections for two-photon absorption (Bamford, *et al*, 1986). The measurement can instead be calibrated by comparison to a known atom source for a specific laser and pumping geometry. No uncertainty is introduced by branching ratios because radiative decay of the upper state is only allowed via fluorescence at 845 nm. If collisions occur, however, the collisional quenching rates must be known. Single-shot measurements may be difficult to make if efficient collision partners are present. Fluorescence signals increase when the laser intensity is increased, but this may lead to photochemical effects (Miziolek and DeWilde, 1984). The signals can also be boosted with coherent techniques, which are a subject of ongoing research. Since its introduction, two-photon LIF has found application in many systems where signal averaging is possible, for example Dyer, *et al* (1990).

Vacuum ultraviolet light can be generated by third-harmonic generation on the $2p\,^3P - 3s\,^3S^o$ transition (Celii, *et al*, 1990). The authors note that the incident 390 nm photons can be generated from a dye laser without doubling, mixing, or Raman shifting, and suggest that lower photon energies reduce the possibility of photochemical effects. The laser frequency for peak conversion depends on the ground state number density, and scans near resonances yield this information. The frequency-tripled signal is at 130 nm, so the test gas must transmit VUV near the resonance lines. This technique has been demonstrated in a flow cell.

Absorption from excited states can be detected with semiconductor lasers. The population of $3s\,^5S^o$ has been measured in a plasma torch (Baer, *et al*, 1993) and behind a reflected shock (Chang, *et al*, 1993). By scanning the laser frequency across the transition, the entire lineshape is recorded. The excited state number density is deduced from the absorption, and the translational temperature from the Doppler width. Additional information is available from the Lorentzian component. If the flow time is shorter than the scan time, the laser frequency can be fixed to record the time history of line center absorption. Two requirements are placed on the test flow. First, the temperature must be high enough to populate the absorbing level at 73768 cm^{-1}. Second, the population of the excited state must be related in a known way (*i.e.*, Boltzmann fraction or rate equations) to the ground state population. If these two conditions are established, then atomic oxygen number density can be monitored with this technique.

Table 1.1. Summary of optical diagnostics for atomic oxygen detection.

Technique	Advantages	Disadvantages
Spontaneous emission	Simplicity	Excited state population Line of sight
Resonance absorption	Ground state population Single-shot	Low number density VUV generation VUV propagation Line shape uncertainties Line of sight
Spontaneous Raman	Ground state population UV/Visible laser	Weak signal Spectral interferences
Intracavity absorption	Ground state population CW measurement	Absolute calibration Weak signal Line of sight
CARS	Ground state population UV/Visible laser	Spectral interferences
Two-photon LIF	Ground state population Good spatial resolution No VUV generation No VUV propagation	Weak transition Absolute calibration Quenching Quenching uncertainties Induced photochemistry
Third-harmonic generation	Ground state population Coherent signal Good spatial resolution	Scanning required VUV propagation
Diode laser absorption	Solid-state lasers Near-IR transitions CW/scanning	Excited state population High temperature only CW/scanning Line of sight
Single-photon LIF	Ground state population Good spatial resolution	VUV generation VUV propagation Quenching Quenching uncertainties Radiation trapping

Advances in VUV generation have made single photon LIF possible on the resonance transition. Raman-shifted UV lasers can excite $2p^3P - 3p^3S^o$ at 130 nm. This approach has been demonstrated in a low pressure test cell (Döbele, *et al*, 1986) and by monitoring the velocity distribution of sputtered oxygen atoms (Goehlich, *et al*, 1991). If the number density between the excitation region and detector is too high, then radiation trapping and resonance scattering effects make data interpretation difficult. Otherwise, spatial resolution is typical of single photon LIF. The effect of quenching depends on collision rates, but the short lifetime of the $3p^3S^o$ state enhances fluorescence yield.

1.3.2 Stimulated Raman scattering

Stimulated Raman scattering (SRS) generates coherent beams at wavelengths different from that of the incident laser beam. Minck, *et al* (1963) first observed SRS in gaseous media by focusing a ruby laser beam into H_2, D_2, and CH_4. The output beams were dispersed, and various Stokes and anti-Stokes orders were identified. Raman shifting, as the process became known, generates several different wavelengths with a single laser.

Development of other lasers has opened up new wavelength regions, and these can also be extended by Raman shifting. Tunable UV radiation is generated by Raman-shifting of frequency-doubled dye lasers (Wilke and Schmidt, 1979). The efficiency of SRS for high orders increases dramatically if the Raman medium is cooled to liquid nitrogen temperatures (Brink and Proch, 1982). A dye laser beam can be Raman-shifted to the ArF excimer wavelength, amplified, and used to pump a cooled hydrogen cell (Döbele, *et al*, 1987). The sixth anti-Stokes component overlaps the atomic oxygen resonance triplet, serving as the light source for LIF in flow cells (Döbele, *et al*, 1986) and sputtering experiments (Goehlich, *et al*, 1991). Faris and Dyer (1993) report measurements of pumping directly with an ArF laser. The authors also summarize parameters relevant to SRS in H_2, HD, and D_2.

1.4 Statement of the problem

In this study, a modified version of atomic resonance absorption is explored. Absorption from the $^3P_{2,1,0}$ state at 130 nm is a direct indication of ground state number density, and has only a secondary dependence on temperature and total number density. In previous experiments, atomic oxygen resonance lamps provided the narrowband VUV. These lamps emit light very near the center of the resonance line where the strength of the absorption leads to complete attenuation for moderate number densities.

By tuning the wavelength of the light source from the line center into the line wings, absorption measurements can be made at higher number densities. With a hydrogen Raman shifter, the sixth anti-Stokes shift from an ArF excimer laser overlaps the $^3P_1$ - $^3S^o$ transition. The ArF excimer can be injection locked to provide narrowband radiation over a modest tuning range. Thus, an ArF-pumped hydrogen Raman shifter can be used in place of the resonance lamp as a light source. With a tunable source, higher number densities can be measured. In this study, we demonstrate absorption measurements in a shock tube at atomic oxygen number densities of 3×10^{17} and 9×10^{17} cm^{-3}.

The spectral distribution of absorption is described by the line shape function, *i.e.* absorption at a given wavelength is proportional to the line shape function at that wavelength. Mechanisms leading to the line shape function are described in later chapters. For the present discussion, it is sufficient to note two different mechanisms. The first is Doppler broadening, which arises from the thermal motion of the oxygen atoms. The second is collisional broadening, which is caused by collisions of the oxygen atoms with nearby atoms or molecules. Broadening mechanisms are often characterized by the full width at half maximum (FWHM), that is the width of the line shape function where the value is half of the maximum.

Line shape functions are plotted in Fig. 1.2 for two different conditions, a low density typical of previous ARAS measurements, and a high density typical of the current test conditions. The line shapes are plotted as a function of frequency relative to the center frequency of the line. In the low density case, collisional broadening is almost negligible. The line shape function is determined by Doppler broadening. In the high density case the collisional width is no longer negligible, although it is still much smaller than the Doppler width. For small detunings, Doppler broadening is dominant. The two broadenings have a different functional form, however, and Doppler broadening decreases exponentially with detuning. In the far wings, therefore, collisional broadening is dominant and Doppler broadening is negligible.

Transmission profiles for the two cases are shown in Fig. 1.3. At low density, absorption is dominated by Doppler broadening. At high density, the gas absorbs completely at the line center. Only in the far wings can meaningful absorption measurements be made. Tuning the laser frequency away from the line center accesses this spectral region. As noted above, collisional broadening dominates this spectral region, which is a thousand halfwidths from the line center. The laser linewidth is 0.9 cm^{-1}, which is narrow enough to resolve the line shape in this region.

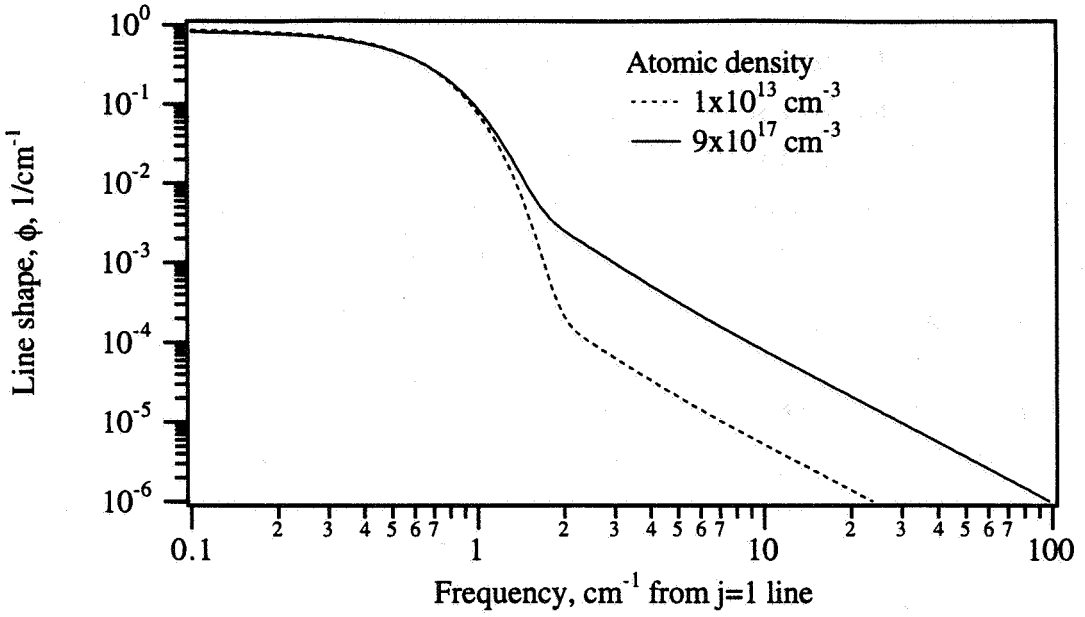

Figure 1.2 Line shape functions for O atom line at 130.49 nm for two number densities at 6000 K.

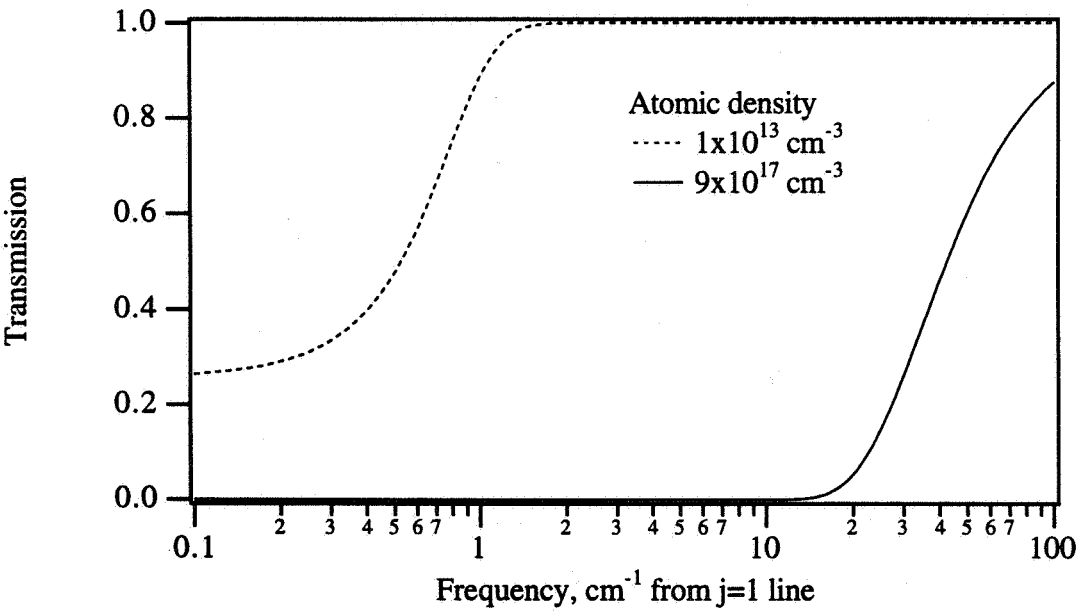

Figure 1.3 Transmission through a 10 cm pathlength for two number densities with the line shapes in the previous figure.

There are thus two objectives in this study:

1) Demonstrate atomic resonance absorption spectroscopy with a Raman-shifted laser in a shock tube flow.
2) Measure the spectral distribution of absorption, *i.e.*, the line shape function, under known thermodynamic conditions where collisions with other oxygen atoms are the dominant broadening mechanism.

1.5 Overview

The theory of line broadening is presented in Chapter 2. After a brief introduction to line broadening, classical results for lifetime and Doppler broadening are discussed. The correlation function is introduced, providing a valuable tool for analyzing collisional broadening. Results for various types of collisional broadening are given, and the results are specialized to the atomic transitions at 130 nm.

The experimental design is discussed in Chapter 3. The Electric Arc Shock Tube generates the atomic oxygen required for the measurement, and the characteristics of the facility as well as instrumentation are described. Details of the Raman cell are documented, as well as the overall layout of the vacuum ultraviolet absorption equipment.

Chapter 4 presents the experimental measurements. Performance of the light source is first described. Characterization of the test gas follows, including emission spectra and shock speed measurements. Computations of the composition based on shock speed and of the expected radiation compare favorably with the emission measurements. Vacuum ultraviolet absorption measured at various wavelengths is then presented for atomic number density of 9×10^{17} cm^{-3} (Case A) and 3×10^{17} cm^{-3} (Case B).

Chapter 5 contains an analysis of the absorption measurements. The resonance broadening coefficient is deduced from these measurements, and sources of experimental error are evaluated. Results are compared to resonance broadening measurements made with other species. Limitations of the approximate broadening models employed here are discussed and possible refinements are suggested. Application of the empirical line shape to absorption diagnostics as well as radiative transfer are discussed, including suggestions for future work.

Results of the study are summarized in Chapter 6, followed by conclusions and suggestions for future study. Finally, descriptions of stimulated Raman scattering and high-temperature absorption of molecular oxygen and printouts of the data analysis routines are included in appendices.

Chapter 2
Line Broadening Theory

Spectral absorption and emission lines are caused by transitions between discrete energy levels of the atom. When observed under low resolution, the lines can appear very sharp, but with higher resolution the lines exhibit a finite width due to line broadening. Sometimes the distribution of energy in the line, or the line shape, is symmetric about the center of the line. Other times, the line shape is asymmetric, and the line center is shifted from its unperturbed position.

The line shape plays an important role in radiative transport. The amount of light absorbed at a given wavelength depends not only on the strength of the transition, but also on the line shape. In a gas that is strongly radiating, emission lines may become so intense that some of the emitted light is re-absorbed. The gas is then "optically thick" at this wavelength, and the degree of re-absorption in the line depends on the line shape.

2.1 Introduction to line shapes

A simple model illustrates how a spectral line becomes broadened. A radiating atom can be described classically as an oscillator, radiating at its unperturbed frequency ω_0. After a certain time, this oscillation might be terminated by some process, such as a collision with another atom. The resulting oscillation is the finite wavetrain shown in Fig. 2.1. A Fourier transform of the oscillation shows that the *finite* wavetrain is not described by a single frequency, but by a *spectrum* of frequencies. This spectrum can be determined by comparing the oscillation to various frequencies near the original frequency ω_0. Two frequencies are shown in the figure. Frequency ω_1 is very close to ω_0 and is virtually indistinguishable in this short time. Frequency ω_2 is slightly farther from ω_0, and it makes a smaller contribution to the frequency spectrum than ω_1. Formally, the contribution of all frequencies is found from the Fourier transform of the wavetrain.

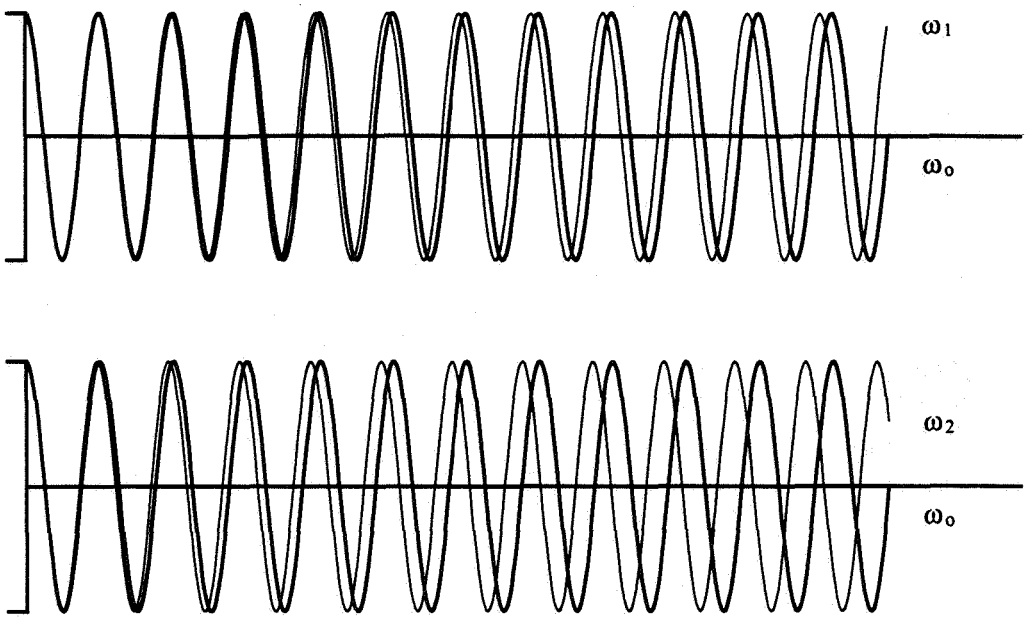

Figure 2.1 Effect of finite wavetrain on apparent frequency of oscillation.

Termination of the oscillation provides a simple demonstration of line broadening, but complete termination of the wavetrain is not required. Many types of collisions merely change the phase of the oscillation, and these collisions cause a similar broadening. In general, any process that causes the oscillation to deviate from an infinite wavetrain causes broadening.

The cumulative effect of all broadening is collected in a single function, the line shape (or line profile) function, ϕ. Application of the line shape function can be illustrated with the Beer-Lambert Law for absorption* The transmission of monochromatic light through a uniform slab of path length, L, is given by

$$\frac{I}{I_o} = \exp[-\alpha L] = \exp[-n\sigma L] \tag{2.1a}$$

In many cases the absorption cross section, σ, is the result of a bound-bound transition. Variation of the cross section as the light frequency is tuned near the resonant frequency is described by the line shape function and a frequency-integrated cross-section

---

* In some cases, the theory can be described most conveniently with the circular frequency, ω, in rad/sec. Results can be converted to energy units of cm^{-1} by dividing by $2\pi c$, with c in cm/sec. The final equations are presented in this way.

$$\frac{I(\bar{\nu})}{I_o(\bar{\nu})} = \exp[-\alpha(\bar{\nu})L] = \exp[-\phi(\bar{\nu})n\sigma_o L] \qquad (2.1b)$$

Variation of the transmitted intensity $I(\bar{\nu})$ at each frequency depends on the absorption coefficient at that frequency, $\alpha(\bar{\nu})$, and on the path length, L. Frequency dependence of $\alpha(\bar{\nu})$ is accounted for by the line shape function, $\phi(\bar{\nu})$. The frequency-integrated absorption cross section σ_0 is a constant that can be computed from either the A coefficient or the oscillator strength for any given transition.† Once σ_o is known, the absorption coefficient can be calculated for any thermodynamic condition where the line shape function and the number density of absorbers, n, are known. In the shock tube measurement, the intensity ratio is measured for a known number of absorbers over a range of frequencies. The line shape is deduced from the measurements with the Beer-Lambert Law.

Line broadening theory is described in the following sections. The simple cases of lifetime and Doppler broadening are presented first. Then the correlation function is introduced, which transforms the problem from the frequency domain to the time domain to facilitate the application of time-dependent perturbation theory. The correlation function is then used to derive the Lorentzian and Gaussian profiles. Finally, collision broadening is described, with an emphasis on resonance interactions, and the results are specialized to the atomic oxygen lines at 130 nm. Broadening of emission lines is considered throughout because this simplifies the analysis; the results should apply equally well for absorption lines.

Numerous articles describing line broadening theory have been written, and further details can be found in them. Specifically, the article by Traving (1968) provides a good overview of line broadening, and additional details on collision broadening are given in the book by Griem (1964). Where applicable, semi-classical methods are used, and these are supplemented by the corresponding quantum mechanical approach where necessary. Details of the correspondence between the semi-classical and fully quantum mechanical approaches are described in Traving (1968).

---

† Hilborn (1982) provides a convenient reference which reviews the details of converting between these different forms, although the definitions are in terms of the circular frequency, ω.

2.2 Lifetime broadening

Lifetime broadening is intrinsic to the radiation process, and it is described completely in terms of atomic properties. In a classical picture, lifetime broadening is a consequence of energy conservation. The radiating atom is modeled as an electron oscillator whose equation of motion includes a damping term for the energy radiated by the oscillating charge. The resulting equation can be approximated by a second-order, damped oscillator whose amplitude decays with time. Although the oscillation frequency is fixed, the effect of the finite wavetrain is a broadening of the frequency spectrum. In this model, the broadening is caused by "radiation damping," and the strength of the actual transition is accounted for with the oscillator strength. Although the electron oscillator model explains lifetime broadening classically, it does not apply directly to an atom with more than two levels.

Quantum mechanically, lifetime broadening is a consequence of the Heisenberg Uncertainty Principle. Atoms do not remain in an excited state indefinitely, but instead decay spontaneously to lower levels. The random lifetime of the upper state leads to an uncertainty in the energy of the excited state, and thus, the energy of the emitted photon.

The linewidth for lifetime broadening can thus be found from the lifetimes of the two energy levels involved in the transition. The Einstein A_{ij} coefficient gives the probability that an atom in any excited energy level i will spontaneously decay to a lower energy level j. The probability of decay from i is found by summing over all possible lower states j. The atom may also undergo transitions due to stimulated absorption or emission of a photon, so similar summations are performed for stimulated processes. The lifetime τ_i of the state i is then given by

$$\frac{1}{\tau_i} = \sum_{j<i} A_{ij} + \sum_{j<i} B_{ij} u_\nu + \sum_{k>i} B_{ki} u_\nu \tag{2.2}$$

The stimulated emission and absorption terms are written in terms of the Einstein B coefficients and u_ν, the energy density of the radiation field. The sums for the emission terms are over all levels, j, which are below i, and the sum for the stimulated absorption term is over all levels, k, which are above i. For transitions in the visible and ultraviolet regions, however, the energy density is rarely high enough for stimulated processes to affect the lifetime appreciably.

Assuming only spontaneous radiative processes, lifetime broadening produces a Lorentzian profile

$$\phi_{Lorentzian}(\bar{\nu}) = \frac{1}{\pi} \frac{\bar{\nu}_L/2}{\left(\bar{\nu} - \bar{\nu}_o\right)^2 + \left(\bar{\nu}_{Lifetime}/2\right)^2} \tag{2.3}$$

with the full width of the line between the half-intensity points (FWHM) given by

$$\bar{\nu}_{Lifetime} = \frac{1}{2\pi c}\left[\frac{1}{\tau_1} + \frac{1}{\tau_2}\right] \approx \frac{1}{2\pi c}\left[\sum_{i<2} A_{2i} + \sum_{i<1} A_{1i}\right] \tag{2.4}$$

The summations are carried out for all levels, i, below levels 2 and 1, respectively.

2.3 Doppler broadening

The motion of atoms relative to the observation frame produces Doppler broadening. For an atom moving through space, the apparent frequency of a photon emitted by the atom is Doppler-shifted by an amount proportional to the relative velocity between the atom and the observer. The random thermal motion of the individual atoms results in a different Doppler shift for each atom. The observed line broadening is a result of photons emitted at different frequencies, so Doppler broadening is sometimes called an inhomogeneous broadening mechanism.

If the velocity distribution of the atoms is Maxwellian, Doppler broadening produces a Gaussian line profile

$$\phi_{Gaussian}(\bar{\nu}) = \sqrt{\frac{4\ln 2}{\pi \bar{\nu}_{Doppler}^2}} \exp\left[-4\ln 2\left(\frac{\bar{\nu} - \bar{\nu}_o}{\bar{\nu}_{Doppler}}\right)^2\right] \tag{2.5}$$

with a Doppler linewidth (FWHM) given by

$$\bar{\nu}_{Doppler} = \frac{1}{\lambda c}\sqrt{\frac{8\ln 2 kT}{M}} \tag{2.6}$$

The Doppler width depends only on the temperature, T, and on the atomic mass, M. In cases of nonequilibrium where a Maxwellian velocity distribution of atoms exists, the translational temperature of the atoms is used. When the velocity distribution is no longer described by a Maxwellian, a non-Gaussian line profile is produced.

This model must be modified at high pressures to account for the effects of collisions on the Doppler broadening process (Traving, 1968). For typical conditions where the emission wavelength is smaller than the mean free path, however, the relations given here are valid.

2.4 The correlation function

Collisional broadening is more complicated than either lifetime or Doppler broadening, and the introduction of a new function, the correlation function, provides a theoretical framework to describe it. Lifetime and Doppler broadening can be modeled with a mix of classical mechanics and elementary quantum theory, providing very useful results. A complete description of collisional broadening, however, is not as simple. Collisional broadening necessarily includes the effects of all atoms in the system, requiring a solution for the wavefunction for all atoms as well as for the radiation field. Finding the complete wavefunction is extremely difficult, and various approximations reduce the problem to a more tractable one. The correlation function arises in both the quantum mechanical and semi-classical treatments, so it provides a convenient form for comparing different approaches.

The advantage of the correlation function lies in its ability to transform the line shape from the frequency domain to the time domain. With time-dependent perturbation theory, the analysis of collisional broadening is simplified enormously. Consequently, the perturbations to the radiating atom can be written as functions of time and the correlation function can be determined. Since the correlation function is the Fourier transform of the line shape, finding the correlation function is sufficient to determine the effect of collisional broadening.

The correlation function can be defined semi-classically by considering an atom oscillating at the frequency ω_o. At time zero, the undisturbed oscillation is

$$f(t) = \exp(i\omega_o t) \tag{2.7}$$

Suppose that perturbations to the oscillation produce a temporary shift in frequency, $\Delta\omega(t)$. The shift in frequency may last for only a short time, such as during a collision, or over a long time, such as that caused by the Doppler effect. In either case, a phase shift will accumulate

$$\eta(t,0) \equiv \int_0^t \Delta\omega(\tau)d\tau \tag{2.8}$$

and the resulting oscillation becomes

$$f(t) = \exp[i\omega_o t + i\eta(t,0)] \tag{2.9}$$

Disturbed and undisturbed oscillations are initially in phase. As the phase shift, η, increases, however, the degree of coherence between them decreases. When η becomes of order one, the coherence between the two oscillations is completely lost. The degree of coherence can be quantified by defining the correlation function, *C(s)*, (Traving, 1968)

$$C(s) \equiv \lim_{\tau\to\infty} \frac{\int_{-\tau/2}^{\tau/2} f^*(t)f(t+s)dt}{\int_{-\tau/2}^{\tau/2} f^*(t)f(t)dt} e^{-i\omega_o s} = \left\langle e^{-i\eta(t+s,t)} \right\rangle \tag{2.10}$$

The product in the numerator is integrated over all time to determine the average phase shift, and the denominator normalizes the result. The factor *exp(-iω$_o$s)* is included to shift the zero of the frequency scale to the undisturbed frequency.

As defined above, the correlation function has the properties that one expects. Initially *C*(0)=1, indicating complete coherence, and perturbations gradually destroy all correlation with the original oscillation. With increasing *s*, the phase shift term oscillates between 0 and 2π, but the expectation value approaches zero. Thus, *C(s)* decreases and approaches zero in the limit as *s* approaches infinity.

The Fourier transform of *C(s)* gives the line shape function

$$\phi(\Delta\omega) = \mathbf{Re}\frac{1}{\pi}\int_0^{+\infty} C(s)\exp(-i\Delta\omega s)ds \tag{2.11}$$

The line shape is given in terms of $\Delta\omega \equiv \omega - \omega_o$.

Two sample cases illustrate the use of the correlation function. *C(s)* can be expanded in a power series in *s* so that

$$C(s) = \exp\left(-a_1 s - a_2 s^2 \ldots - ib_1 s - ib_2 s^2 \ldots\right) \tag{2.12}$$

As an example, consider only the linear term.

$$\phi(\Delta\omega) = \mathbf{Re}\frac{1}{\pi}\int_0^{+\infty}\exp(-a_1 s - i\Delta\omega s)ds = \frac{1}{\pi}\frac{a_1}{\Delta\omega^2 + a_1^2} \tag{2.13}$$

The resulting shape is a Lorentzian profile. If the quadratic term is retained instead, the resulting shape is a Gaussian profile:

$$\phi(\Delta\omega) = \mathbf{Re}\frac{1}{\pi}\int_0^{+\infty}\exp(-a_2 s^2 - i\Delta\omega s)ds = \frac{1}{\sqrt{4\pi a_2}}\exp\left(-\frac{\Delta\omega^2}{4a_2}\right) \tag{2.14}$$

Other shapes are produced by different correlation functions. As shown in Traving (1968), a combination of the first two terms produces the Voigt function. Imaginary terms in $C(s)$ produce asymmetries and shifts away from the center frequency, ω_o.

To summarize, the correlation function, $C(s)$, is the Fourier transform of the line shape function. By transforming the line broadening problem to the time domain, the correlation function provides a method for determining the line shape from time-dependent perturbation theory. The value of $C(s)$ decays from one to zero, and with simple forms of $C(s)$, the Lorentzian and Gaussian profiles are produced.

2.5 Collisional broadening

Interactions between the radiating atom and other particles cause collisional broadening of spectral lines. In this section, theoretical models of collisional broadening are presented. Analysis is performed with a semi-classical model in which the perturber and the atom follow classical paths, and the effect on the atom is treated quantum-mechanically. The perturber is assumed to follow a straight-line path, so that its motion is unaffected by the interaction. This approximation is reasonable for collisions in which the interaction energy is very much smaller than the relative translational energy of the collision. For very strong collisions, the perturber does not follow a straight line path; however, complete dephasing occurs in these collisions, so that the details of the collision are not important. Collisions are assumed only to perturb the phase of the oscillation, so transitions caused by inelastic collisions are neglected. Inelastic collisions produce non-radiative decay, or quenching, which reduces the lifetime of the levels. This effect can be included as an added term to the lifetime broadening (Demtröder, 1982, pg. 84), but it is neglected here.

The interaction potential is modeled with a spherically symmetric function of the separation which is independent of the relative energy of the collision. This assumption is similar to the Born-Oppenheimer approximation for the vibration of diatomic molecules. Finally, the analysis is restricted to include only interactions with the nearest neighbor. When interactions with multiple perturbers are important, they are assumed to occur as separate events.

With these assumptions, the behavior of the radiating atom can be modeled with perturbation theory, and the perturbed Hamiltonian can be written as a function of time. Implementation of these assumptions is discussed in Traving (1968). The results of the semi-classical analysis can be written as a correlation function to compare with the results obtained with a quantum mechanical analysis.

Various collisional broadening models are characterized by the types of interactions and by the line broadening model. Approximate interaction laws are described in the next section. The following sections describe two limiting cases for line broadening theories:

1) Impact approximation, which is valid near the center of the line.
2) Quasi-static approximation, which is valid in the line wing regions.

2.5.1 Interaction laws

Analyzing the interaction between two atoms requires the solution of the Schrödinger equation for the isolated atoms and the Coulomb interactions between the charges in the two atoms. The solution for the isolated atoms is generally known, at least to within some approximation. The interaction potential between the two atoms, V(r), can be expanded in a power series in 1/r (see for example Margenau and Kestner, 1971), and the effect on the radiation field determined by perturbation theory. Various terms in the power series expansion can be assigned to different multipole interactions. At interatomic separations, r, which are large relative to the atomic size, the leading term can provide a fair approximation to the potential. As the separation is decreased, higher order terms are required. Overlap between the electron clouds of the two atoms becomes important, and the appropriate quantum numbers become those for a diatomic molecule. Inclusion of more realistic interaction potentials is an obvious avenue to improve line broadening predictions.

When a single term of the expansion is sufficient, the interaction leads to a shift in frequency given by the general form

$$\Delta\omega = \frac{C_p}{r^p} \tag{2.15}$$

The value of p depends on the type of interaction, and the strength of the interaction is given by C_p. When comparing different models, it is important to note that the units of the interaction energy are implicit in the expression for C_p. Stark, van der Waals, and resonance interactions can all be modeled with this approximate potential.

Stark broadening: Collisions with charged particles cause Stark broadening. Charged particles produce long-range Coulomb forces which perturb the radiating or absorbing atom. Even when charge neutrality exists on a macroscopic scale, microfields are generated by the distribution of positive and negative particles. The microfield at the atom is the vector sum of the fields produced by all local perturbers. The analysis is frequently simplified by assuming that the field is constant over the entire electron cloud. For many-electron atoms, such as oxygen, the interaction leads to a potential with p=4; values of the interaction constant are derived from linewidth measurements (Konjevic and Roberts, 1976, Park, 1985). Broadening by electrons and ions are often modeled separately because electrons typically move much faster than the relatively massive ions.

Van der Waals broadening: Interactions with neutral particles are characterized by shorter range forces than those with charged particles. The interaction potential can be expanded in terms of dipole-dipole interactions. If atom and perturber are not resonant with each other, then the first order term disappears, and the second order term gives p=6. The value of the interaction parameter is generally not available from theory, but is related to the polarizabilities of the atom and the perturber. The van der Waals interaction accounts for the attractive portion of the Lennard-Jones 6-12 potential.

Resonance broadening: When the atom of interest (A) and the perturber (B) are of the same type, then a resonance exists between the two particles. The resulting state is a superposition of degenerate states in which either A or B is excited, and the interaction potential is given by the dipole-dipole interaction (Ali and Griem, 1965)

$$V_{dd} = \left[\frac{\boldsymbol{d}_A \cdot \boldsymbol{d}_B}{|\boldsymbol{r}|^3} - 3\frac{(\boldsymbol{d}_A \cdot \boldsymbol{r})(\boldsymbol{d}_B \cdot \boldsymbol{r})}{|\boldsymbol{r}|^5} \right] \tag{2.16}$$

where $\boldsymbol{d}_A$ and $\boldsymbol{d}_B$ are the dipole moment operators of the radiating and perturbing atoms, respectively, and $\boldsymbol{r}$ is the position vector between the perturber and the radiating atom. The interaction arises from a quantum-mechanical resonance which exists between two like atoms in which the atoms are exchanging "virtual" photons. This interaction occurs for

collisions in which the perturber (B) is in an energy level connected by a dipole-allowed transition to either the upper or lower energy level of the transition of atom A. Resonance broadening is commonly only important for those lines whose upper or lower levels are dipole-connected to the ground state because, in many cases, most perturbers are in the ground state.

2.5.2 Impact approximation

In the impact approximation, the atom is assumed to oscillate at the transition frequency ω_o until a collision with a perturber. The impact causes a phase shift in the oscillation, and the subsequent oscillation is not coherent with the original wavetrain. The correlation function can be found by dividing the exponential into real and imaginary terms

$$C(s) = \left\langle e^{-i\eta(t+s,t)} \right\rangle = \left\langle \cos \eta(t+s,t) \right\rangle - i \left\langle \sin \eta(t+s,t) \right\rangle \tag{2.17}$$

The expectation values can be found by analyzing the properties of the phase shift function. The effect of a collision is assumed to be an instantaneous phase shift, so that $\eta(t+s,t)$ for a given atom is a series of step functions. Individual collisions are assumed to be statistically independent, so the phase shifts are random. Statistically, then, $\eta(t+s,t)$ is a function whose value is initially zero, and whose expected value remains zero as the RMS value increases with time, if both positive and negative shifts are equally likely.* The expected value of the real term approaches zero, because when the RMS value of $C(s)$ becomes much larger than π, the expected value of the cosine term approaches the average value of zero. Initially, however, η=0, and the cosine term is unity. The imaginary term is initially zero, and its expected value remains zero. Thus, the correlation function for this case is real, and gradually decays to zero.

The form of this decay is exponential, as illustrated by the case of strong collisions. Initially the atom is undisturbed, and the oscillation is coherent. After a random period of time a collision occurs which destroys the coherence. The expected value for the ensemble at a given time is determined by the fraction of atoms that have not yet experienced a collision, and this is given by an exponential distribution

---

* If positive and negative shifts are not equally likely, the imaginary term is not identically zero and the center frequency is shifted, as shown in Traving (1968). The resulting line shape is still Lorentzian, but with a shift in the center frequency.

$$C(s) = \exp(-s / \tau) \tag{2.18}$$

This form of the correlation function is discussed in the previous section, where it is shown that a Lorentzian line profile is produced. Thus, the impact approximation yields a Lorentzian profile whose linewidth is determined by the dephasing time for collisions.

This result is valid under conditions where the impact approximation can be made. The duration of the collisions is assumed to be much shorter than the time between collisions. A validity criterion can be derived by estimating the collision duration and collision frequency; an appropriate criterion for the resonance interaction is given in Section 2.6.2.

2.5.3 Quasi-static approximation

In the quasi-static approximation, nearby perturbers shift the energy levels of the atom so that the transition frequency is different from that of an unperturbed atom. The distribution of perturbed frequencies for different atoms forms the line profile. The model is developed by first assuming that the positions of the perturbers, and not the velocities, determine the perturbation in the line frequency. The shift in energy levels caused by any configuration of perturbers is calculated and the probability distribution of possible configurations is then used to assign probabilities to each shift. The resulting line profile maps out the probability of any given shift. If the probability distribution is normalized, then the line shape is normalized automatically.

A general form of the line shape can be derived classically after making two approximations (Traving, 1968). The first is the "nearest neighbor approximation," in which the perturbation is caused only by interactions with the nearest perturber. This approximation is only necessary if the forces from different perturbers do not add linearly, such as in resonance broadening. This approximation is justified for interactions where the separation, r, is much less than the average spacing because the probability of two perturbers at such small r is very low. The second approximation is a spherically symmetric interaction potential. This simplifies the mathematics of the derivation because averaging over angles is unnecessary.

The probability W of finding the nearest perturber between r and $r+dr$ depends on the probability W_+ that a particle is in the region and W_- that a particle is not at a smaller r.

$$W(r)dr = W_+\left(4\pi r^2 dr\right)W_-\left(\frac{4\pi r^3}{3}\right) \tag{2.19}$$

If n is the number density of perturbers, then the probability of finding the nearest perturber between r and $r+dr$ is

$$W(r)dr = 4\pi n r^2 \exp\left[\frac{-4\pi n r^3}{3}\right]dr \tag{2.20}$$

The probability function $W(r)$ is analogous to the density matrix in a quantum mechanical treatment.

If the interaction can be modeled with an inverse power law,

$$\Delta\omega = \frac{C_p}{r^p} \tag{2.21}$$

then the line shape is

$$\phi(\Delta\omega) = \frac{3}{p}\left(\frac{\Delta\omega_o}{\Delta\omega}\right)^{\frac{p+3}{p}} \exp\left(-\left|\frac{\Delta\omega_o}{\Delta\omega}\right|^{\frac{3}{p}}\right)\frac{1}{\Delta\omega_o} \tag{2.22}$$

where

$$\Delta\omega_o \equiv \frac{C_p}{r_o^p} = C_p\left(\frac{4\pi n}{3}\right)^{\frac{p}{3}} \tag{2.23}$$

is the shift due to a perturber at the mean distance between particles.

Finally, consider the situation where the interaction is orientation dependent. As an example, imagine that two interactions are possible, each with a different likelihood: $\Delta\omega = C'_p\, r^{-p}$ with a probability of ξ' and $\Delta\omega = C''_p\, r^{-p}$ with a probability of ξ''. The probabilities are normalized so that $\xi'+\xi''=1$. Each generates a line shape function $\phi'(\Delta\omega)$ and $\phi''(\Delta\omega)$, both based on the total number density, n. Since the line shape function expresses the probability of a given shift, the net line shape is the sum of the shapes for each orientation weighted by the probabilities of each orientation:

$$\phi(\Delta\omega) = \xi'\phi'(\Delta\omega) + \xi''\phi''(\Delta\omega) \tag{2.24}$$

2.6 Results for atomic oxygen

In this section, theoretical absorption shapes for the ^3P-$^3S^o$ triplet at 130 nm are calculated using the equations given in the previous sections. Relevant characteristics of the transition are presented, including line strengths and line positions. Details of the line shape calculation are then presented in two parts: first, calculation of the resonance width, followed by calculation of the other widths which are then combined into a single line shape function. These results are then used to calculate the theoretical absorption shape for the high density test condition.

2.6.1 Oxygen triplet characteristics

Spin-orbit coupling produces a splitting of the ^3P ground state into three sub-levels, each denoted by their j-values. The resulting triplet consists of lines at 130.21685, 130.48576, and 130.60286 nm (Moore, 1993). Relevant transition properties are shown in the following table (Hibbert, *et al*, 1991). Note that the absorption cross sections in the table must be used with the number density in the absorbing state, not the total atomic number density.

Table 2.1 Characteristics of the atomic oxygen triplet at 130 nm

λ, nm	130.21685	130.48576	130.60286
$\bar{\nu}$, cm^{-1}	76794.978	76636.713	76568.001
E_{lower}, cm^{-1}	0.000	158.265	226.977
j_{lower}	2	1	0
g_{lower}	5	3	1
A, sec^{-1}	3.55×10^8	2.12×10^8	0.706×10^8
f_a	0.0542	0.0542	0.0542
f_e	0.0903	0.0542	0.0181
σ_o, $cm^2\ cm^{-1}$	4.80×10^{-14}	4.80×10^{-14}	4.80×10^{-14}

2.6.2 Resonance width

Resonance broadening of the lines can be calculated with the impact approximation (Ali and Griem, 1965). This model assumes a $1/r^3$ potential, and that the linewidth

depends on the oscillator strengths for both absorption and emission. The resulting line shape is a Lorentzian with the linewidth (FWHM)*

$$\omega_{Resonance} = 4\pi\sqrt{\frac{7g_a}{3g_e}}\frac{e^2 f_a}{8\pi\varepsilon_o m\omega_o}n = 4\pi\sqrt{\frac{7}{3}}\frac{e^2 f_a}{8\pi\varepsilon_o m\omega_o}\sum_{j=0}^{2}\sqrt{\frac{g_a}{g_e}}n_j \qquad (2.25)$$

where the lower (absorbing) level is denoted *a*, and the upper (emitting) level is denoted *e*.

The summation is required to account for collisions with atoms in each of the three different *j*-levels of the ground state. This differs from the calculation by Park (1985), in which only collisions with atoms in the same *j*-level are included. The role of collisions with atoms in different *j* in absorption can be understood by first considering their role in emission. The emission process begins with an excited state atom in $^3S^o$. If this atom collides with a ground state atom in *j*=2, for example, the collision produces a resonance interaction since a dipole transition is allowed between these two states. Despite the interaction, however, the atom can still decay into any of the three *j*-levels. In the reverse process, then, an atom can begin in the *j*=1 level, for example, and transition into $^3S^o$. If a collision with a *j*=2 atom occurs during this process, a resonance interaction will occur and the absorption line is broadened.

The linewidth can be rewritten in terms of the spontaneous transition probability of any of the lines, after accounting for the degeneracies. Choosing the probability for the line at 130.49 nm, and converting from the circular frequency to wavenumber units

$$\overline{\nu}_{Resonance} = \sqrt{\frac{7}{3}}\frac{\lambda^3 A_{130.49}}{16\pi^3 c}\sum_{j=0}^{2}\sqrt{\frac{g_a}{g_e}}n_j = 4.84x10^{-20}\sum_{j=0}^{2}\sqrt{\frac{g_a}{g_e}}n_j \; cm^3 cm^{-1} \qquad (2.26)$$

For atomic oxygen, the summation is required to account for collisions between an excited atom and an atom in any of the three lower *j*-levels. This summation gives the average strength of the interaction, and can be determined approximately by assuming that the relative populations in the *j*-levels are given by the degeneracies of the levels. This ratio is exact in the limit of very high temperatures, and is a good approximation at temperatures

* This equation differs in two ways from that given in the original reference. The width is multiplied by two to give the FWHM, and the units for the electron charge have been changed from electrostatic units.

high enough to dissociate oxygen.† By noting that the absorption oscillator strength is the same for all three sub-levels, the summation becomes

$$\sum_{j=0}^{2}\sqrt{\frac{g_a}{g_e}}n_j=\left[\sqrt{\frac{1}{3}}\frac{1}{9}+\sqrt{\frac{3}{3}}\frac{3}{9}+\sqrt{\frac{5}{3}}\frac{5}{9}\right]n_l=1.1147n_l \tag{2.27}$$

With this approximation, the Lorentzian width for resonance broadening is

$$\overline{\nu}_{Resonance}\approx\left(4.84x10^{-20}\right)\left(1.1147n_l\right)\,cm^3cm^{-1}=5.39x10^{-20}n_lcm^3cm^{-1} \tag{2.28}$$

The resonance linewidth thus depends only on the number density of colliding atoms in the lower state, n_l. The lower state is the ^{3}P ground state, so for most cases, n_l is nearly equal to the total number of oxygen atoms.

Two requirements must be fulfilled for the impact approximation to be valid. First, the collision duration must be much shorter than the time interval between collisions. Second, the line shape applies only to frequency separations from the line center for which the inverse of the separation is much longer than the duration of a collision. Consequently, impact theory is valid near the center of the line and is subject to the following criterion (Ali and Griem, 1965)

$$\left|\overline{\nu}-\overline{\nu}_o\right|\ll\frac{1}{2\pi c}\left(\frac{g_e}{g_a}\right)^{1/4}\left(\frac{4\pi\varepsilon_o m\omega_o}{e^2f_a}\right)^{1/2}\left(\frac{kT}{M}\right)^{3/4} \tag{2.29}$$

The region of applicability depends only on the (translational) temperature and on the given transition. At 6000 K, the term on the right hand side is 13 cm^{-1}. Experimental line shape measurements are made over a frequency range of approximately 2 - 60 cm^{-1}. In this intermediate region, neither the impact nor the quasi-static theories are expected to be strictly valid. As shown below, however, both theories give nearly equivalent results, so that they *might* be expected to provide a good description in the intermediate region as well.

---

† The value of this factor decreases monotonically with temperature, and can be modeled by 0.176 exp(-T/550K) + 1.1147. This approximation is accurate to within 2%, and has the correct limiting behavior at high temperature.

The quasi-static theory is commonly applied in the line wing region. The interaction constant, C_3, is required to calculate the width parameter for resonance broadening. In general, the interaction constant is given by

$$C_3 = \zeta \frac{e^2 f_a}{8\pi\varepsilon_o m\omega_o} \tag{2.30}$$

The value of ζ is on the order of one, and depends on the orientation of the dipole moments relative to the line between radiator and perturber. In addition, both positive and negative frequency shifts are possible, depending also on the orientation. An estimate of ζ can be obtained from the result for hydrogen (Traving, 1968). The width parameter as defined in Eqn. 2.23 (*not* the FWHM) is

$$\Delta\omega_o = \frac{e^2 f_a n_l}{9\varepsilon_o m\omega_o} = \frac{1}{36\pi^2}\lambda^3 n_l A_{130.49} \tag{2.31}$$

As in the impact approximation, the width depends on the transition probability and on the number density of atoms in the lower (*i.e.*, ^{3}P) level. Substituting in the required constants and converting to wavenumber units,

$$\Delta\bar{\nu}_o = \frac{1}{72\pi^3 c}\lambda^3 n_l A_{130.49} = 7.038x10^{-21} n_l \; cm^3 cm^{-1} \tag{2.32}$$

Thus, the quasi-static line shape is

$$_{Q.S.}\phi_{Resonance}(\Delta\bar{\nu}) = \frac{|\Delta\bar{\nu}_o|}{\Delta\bar{\nu}^2}\exp\left[-\left|\frac{\Delta\bar{\nu}_o}{\Delta\bar{\nu}}\right|\right] \approx \frac{|\Delta\bar{\nu}_o|}{\Delta\bar{\nu}^2} \tag{2.33a}$$

$$\Delta\bar{\nu} \equiv \bar{\nu} - \bar{\nu}_o \tag{2.33b}$$

The exponential term is nearly equal to one in the far wings; neglecting it leads to the simple quadratic profile which is valid only in the line wings.

Although the impact and quasi-static models are very different, line shapes calculated with the two models are nearly the same in the line wings. For example, the linewidth for a number density in the ^{3}P state, n_l, of $9x10^{17}$ cm^3, can be calculated in the impact approximation with Eqn. 2.28. The resulting shape is a Lorentzian profile

$$_{Impact}\phi_{Resonance}(\bar{\nu}) = \frac{1}{\pi}\frac{0.0485/2}{(\bar{\nu}-\bar{\nu}_o)^2+(0.0485/2)^2} \approx \frac{7.72x10^{-3}}{(\bar{\nu}-\bar{\nu}_o)^2} cm^{-1} \qquad (2.34)$$

The line shape for the quasi-static model is given by Eqns. 2.32 and 2.33. At this number density, the line shape is

$$_{Q.S.}\phi_{Resonance}(\bar{\nu}) = \frac{6.33x10^{-3}}{(\bar{\nu}-\bar{\nu}_o)^2}\exp\left[-\left|\frac{6.33x10^{-3}}{\bar{\nu}-\bar{\nu}_o}\right|\right] cm^{-1} \approx \frac{6.33x10^{-3}}{(\bar{\nu}-\bar{\nu}_o)^2} cm^{-1} \qquad (2.35)$$

The line shapes given by Eqns. 2.34 and 2.35 are plotted in Fig. 2.2 as a function of the distance from the center of the line. The Lorentzian profile is almost constant near the line center, then exhibits an inverse quadratic dependence on frequency. The quasi-static profile behaves differently near the line center, but it also has an inverse quadratic dependence in the wings. However, both of these curves have been extrapolated far beyond the regions in which they are valid. According to Eqn. 2.29, the impact approximation is valid at frequencies much less than 13 cm^{-1} away from the line center. At very large separations, the assumption that the broadening collisions are "instantaneous" fails. On the other hand, the quasi-static theory is valid for frequencies much more than 13 cm^{-1} away. Near the center of the line, the assumption that broadening is independent of the colliding particle motion breaks down. Neither theory is strictly valid in the intermediate region where the absorption measurements are made; however, the two models give virtually the same results. Comparing the approximate relations in Eqns. 2.34 and 2.35 reveals that the two profiles have the same functional form and agree to within about 20% in this region.

2.6.3 Absorption profile calculation

Calculations are presented in this section for the test conditions in Case A, which are summarized in Table 4.1. Absorption by atoms in the three different *j*-levels each produce a separate line, and all three components of the resulting triplet are included explicitly in the calculation:

$$\frac{I(\bar{\nu})}{I_o(\bar{\nu})} = \exp\left[-n_{j=2}\sigma_o L\phi(\bar{\nu}-\bar{\nu}_{j=2}) - n_{j=1}\sigma_o L\phi(\bar{\nu}-\bar{\nu}_{j=1}) - n_{j=0}\sigma_o L\phi(\bar{\nu}-\bar{\nu}_{j=0})\right] \qquad (2.36)$$

All three lines have the same absorption cross-section, which is listed in Table 2.1, along with frequencies of the three line centers. Number density in each j-level is given by a Boltzmann distribution at 6100 K, determined from the energy levels and degeneracies also listed in Table 2.1. The path length is the internal diameter of the shock tube, 10 cm.

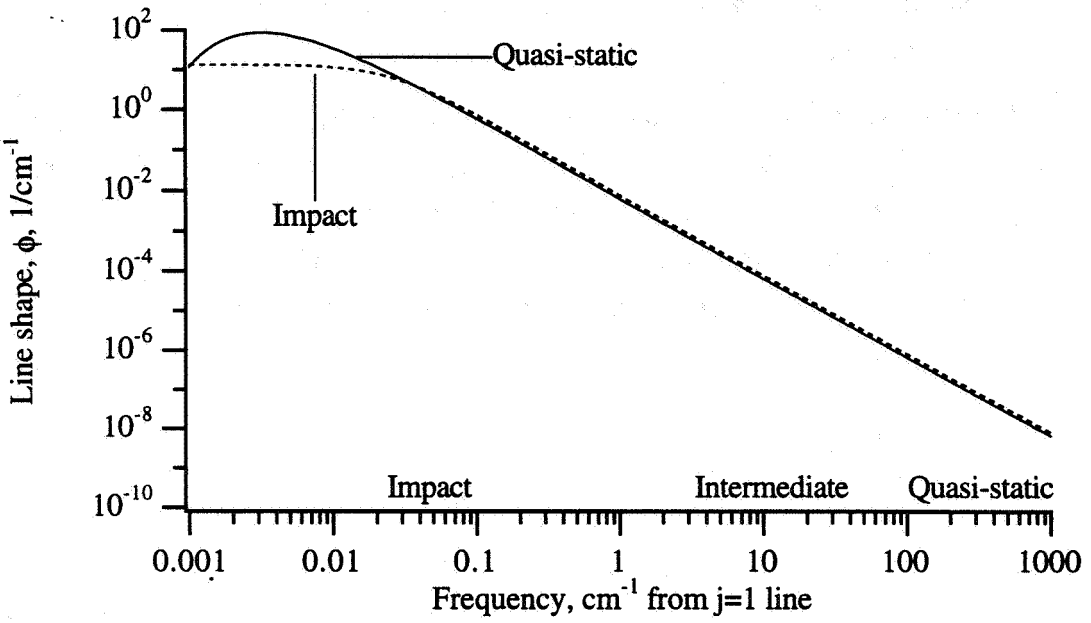

Figure 2.2 Line shapes for impact and quasi-static models of resonance broadening for the j=1 line at a perturber density of $9x10^{17}$ cm^{-3}. The impact model is applicable near the center of the line, and the quasi-static in the far wings.

Variation of the absorption with frequency is calculated from the line shape function. Expressions for the linewidths due to various broadening mechanisms are given in previous sections, and results are listed in Table 2.2. The Gaussian width for Doppler broadening is calculated from Eqn. 2.6, and the Lorentzian width for lifetime broadening from Eqn. 2.4. The Stark linewidth for broadening by electrons is given by (Park, 1985)

$$\overline{\nu}_{Stark} = 9.21x10^{-18}\left[\frac{T_e}{10^4 K}\right]^{0.38} n_e \; cm^3 cm^{-1} \tag{2.37}$$

where T_e is the electron temperature and n_e is the number density of electrons. Stark broadening by ion collisions is modeled with the rough approximation that it produces a Lorentzian component with the same width.

A common method for combining various broadening mechanisms is convolution into a Voigt profile (Traving, 1968, Park, 1985). To do this, however, the resonance line

shape must be modeled with a Lorentzian profile, and this requires the following approximation:

> *The impact approximation, which produces a Lorentzian, is invalid in the intermediate line wing region. However, the quasi-static model which is applicable in the far wings has the same frequency dependence and is only 20% lower. Therefore, the resonance line shape is modeled with a Lorentzian profile.*

The resonance linewidth is calculated from Eqn. 2.28, which is derived from the work of Ali and Griem (1965), given by Eqn. 2.25. The resonance width is determined by the number density of perturbers, which is 98.7% of the atomic number density since most atoms are in the ground state. Since collisions with atoms in all three j-levels are assumed to cause broadening, the resonance widths of all three lines are equal. Widths for the other mechanisms are also essentially the same for all three lines, so the calculated line shape function is the same for all three lines.

Table 2.2 Linewidths due to various broadening mechanisms

Mechanism	Profile	FWHM	Conditions
Doppler	Gaussian	1.07 cm^{-1}	T=6100 K
Resonance	Lorentzian	0.0479 cm^{-1}	n_l=8.88x10^{17} cm^{-3}
Lifetime	Lorentzian	0.00339 cm^{-1}	
Stark, electrons	Lorentzian	0.00053 cm^{-1}	n_e=7x10^{13} cm^{-3}

The resulting theoretical absorption profile is plotted in Fig. 2.3. Frequencies are plotted relative to the center of the j=1 line at 76636.713 cm^{-1}. Contributions to the absorption profile from various broadening mechanisms are calculated approximately, and are shown for comparison. Although the Doppler width is largest, its contribution is a Gaussian profile which decays very rapidly with frequency. In the wings, where the absorption is not complete, resonance broadening is the dominant mechanism. Thus, an empirical line shape for resonance broadening can be deduced from the experimental absorption measurements. Data is analyzed in Chapter 5 by fitting profiles calculated with Eqn. 2.36. The resonance broadening is characterized by a Lorentzian width, derived from the empirical width after small corrections for the other broadening mechanisms.

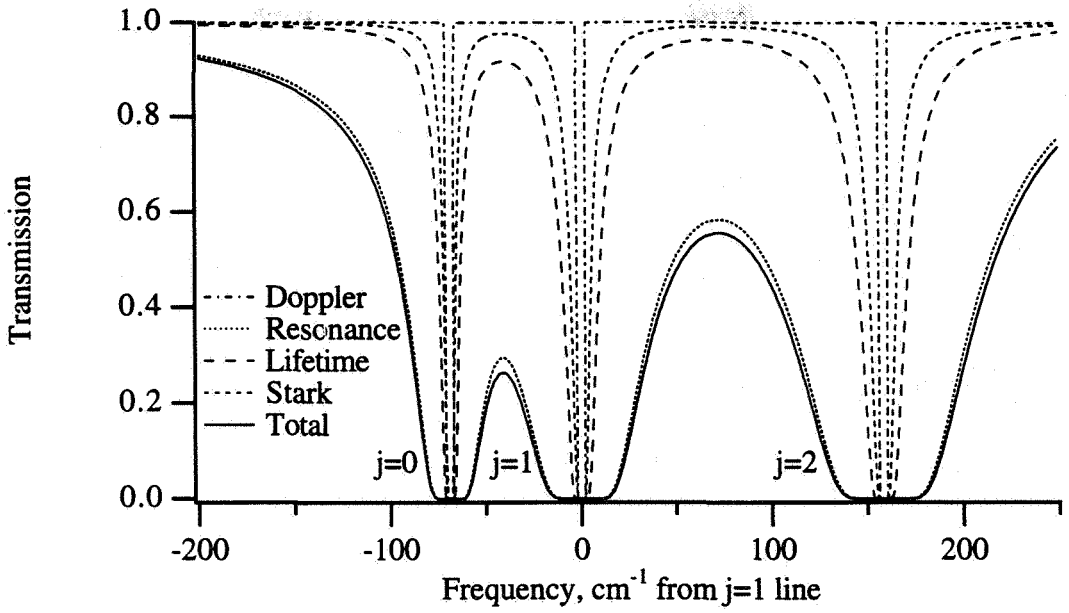

Figure 2.3 Theoretical absorption profile for test conditions of Case A showing approximate contributions of the various broadening mechanisms.

Chapter 3
Experimental Design

This chapter describes the experimental approach followed to measure the absorption line profile for the atomic oxygen resonance triplet. First, the facility and instrumentation for generating the test flow are discussed. Second, the design of the excimer-pumped Raman shifter and associated equipment for the vacuum ultraviolet measurement are presented.

3.1 Description of the facility

This study was performed at the Electric Arc-driven Shock Tube (EAST) Facility at NASA-Ames Research Center. The facility can generate high shock speeds (>10 km/sec) by depositing electrical energy into the driver gas via an arc discharge. A strong shock wave produces atomic oxygen by dissociating molecular oxygen. Although the shock tube is an impulse facility, flow conditions are monitored to characterize the thermodynamic state of the test gas. Thus, absorption measurements are made in a well-characterized flowfield.

3.1.1 Shock tube driver section

The conical driver generates strong shocks with low driven tube pressures. The conical driver has a maximum internal diameter of 10 cm, and is approximately 25 cm long (Fig. 3.1). A tungsten wire is stretched along the axis of the driver and is grounded at one end. The facility is fired by pulling the wire toward a high-voltage electrode which is connected to a capacitor bank. When the circuit is completed, the capacitors begin to discharge through the wire. The wire essentially explodes, leaving a high-temperature column of gas along the axis of the driver and initiating breakdown in the driver gas (Sharma, et al, 1988). Electrical energy in the capacitor bank is then transferred to the driver gas, dramatically raising the temperature and pressure. With the conical driver, the diaphragm bursts at the beginning of the discharge (Dannenberg, 1972). By allowing the

driver gas to expand into the driven tube during energy addition, more energy can be added to the gas for a given peak temperature.

The unique nature of the driver section also has implications for the expansion fan which eventually overtakes the shock front. When the diaphragm bursts in a (traditional) cylindrical driver, a shock wave propagates into the driven section and an expansion fan heads back into the driver section. When the expansion fan encounters the end wall, it reflects back on itself and eventually overtakes the shock front. If this reasoning is applied to the conical driver, a complicated axially-symmetric flowfield is expected, with some portion of the expansion fan being almost immediately reflected and quickly overtaking the shock front. Instead, the addition of energy after the diaphragm bursts effectively delays the reflection of the expansion fan during the discharge (Milton and Dannenberg, 1983). To a rough approximation, the expansion fan enters the driven section when the average driver pressure begins to decrease. The decrease begins when either the driver gas is depleted or the energy addition is completed. The latter case applies to the present test condition. Measurements of the discharge current show that the bulk of the energy addition is completed 50 μsec after the diaphragm bursts. If the shock speed is high enough, the shock wave passes the test section before the expansion fan reaches it.

3.1.2 Shock tube driven section

The driven section of the shock tube is composed of a series of aluminum segments. Each segment has an internal diameter of 10 cm, and an outer diameter of 17.8 cm. The layout is shown in Fig. 3.2. The shock wave propagates through two 244 cm (8 foot) segments before reaching the test section segment. After the test section segment are two more segments, each with optical access to make shock speed measurements downstream of the test section. These are followed by the segment containing the vacuum manifold, and a long segment to the dump tank. The vacuum manifold provides access to the tube through a 7.6 cm (3 inch) port with a customized poppet valve. The surface of the valve facing the shock tube is machined to the same radius of curvature (5 cm) as the driven tube to minimize disturbance to the flow. An ionization gauge measures the pressure at the manifold. Accuracy of this pressure measurement was verified by placing a second gauge in the driven tube, at Station B. Comparison to the driven tube ultimate pressure measured at Station B indicates that the pressure in the tube is a factor of two higher than measured at the manifold. However, the amount of residual gas is determined by the outgas rate, and the rates measured at Station B and the manifold were the same.

Optical access is provided at various stations along the driven section, detailed in Table 3.1. Diametrically-opposed ports at each station allow simultaneous measurements

with two different transducers, such as an ionization probe and a pressure transducer. All shock tube port plugs have the same radius of curvature as the driven tube. VUV absorption measurements are made at the test section, Station F, which has four ports instead of two. Steel reinforcements have been press-fitted over port locations to compensate for stress concentrations at the ports, although the post-shock pressures obtained in the present tests are less than atmospheric pressure.

Table 3.1. Position of observation ports in the driven section, measured relative to the diaphragm.

Station	Distance from diaphragm	Distance from previous station
A	1056 mm	1056 mm
B	2199 mm	1143 mm
C	3189 mm	991 mm
D	4408 mm	1219 mm
E	5221 mm	813 mm
F	5323 mm	102 mm
G	5831 mm	508 mm
H	6745 mm	914 mm

3.1.3 Instrumentation

The test gas is monitored to determine shock arrival, test conditions, and flow quality. Ionization probes and pressure transducers detect shock arrival, and emission measurements characterize the test gas.

The shock front is detected with ionization probes (Dannenberg and Humphry, 1968). Probes consist of two Kovar electrodes embedded in a glass insulator. The insulator is mounted in a port plug so that the electrodes are flush with tube walls and the electrode gap is perpendicular to the flow direction. The electrodes do not extend into the flow. Probes are placed in series with 500 Ω resistors, and an open circuit voltage of about 11.5 V is applied across them. Current flowing between the electrodes is measured with an amplifier which has a frequency response of DC to 3 MHz. When the electrodes are exposed to an ionized flow, probe resistance drops and a larger current flows. In principle, current flow can be related to electron number density. In practice, however, the traces are difficult to interpret, and the current pulse is generally used to detect arrival of the

shock wave. An automated system is available for recording shock arrival time, but in this study the current traces are digitized and the arrival times determined by inspection.

High-frequency pressure transducers also detect arrival of the shock front. Two different transducers are used in this study, PCB Piezotronics models 113A21 (50 mV/psi) and 113A24 (5 mV/psi). The quartz transducers are coupled to the flow via an Invar diaphragm 0.553 cm in diameter, and are acceleration compensated to reduce ringing. Amplifiers inside the transducers provide a voltage signal to drive 100 Ω directly. The resonant frequency of the transducer limits the rise time to about 1 μsec. A 7 mm/μsec shock wave passes over the diaphragm in 0.8 μsec, so the uncertainty in shock arrival time due to finite transducer size and finite frequency response are approximately the same. For identical transducers, however, the response is similar and time intervals can be measured more precisely than shock arrival time.

Pressure transducers exhibit a thermal response. The positive temperature coefficient eventually drives the measured signal up. However, on time scales of 1 msec or less, the thermal response leads to negative pressure readings. The thermal nature of this response has been verified by exposing transducers to radiative heating pulses at atmospheric pressure (Smith, et al, 1992). Although the mechanism for this behavior is not known, thermal distortions of the diaphragm have been suggested. Coating the diaphragm with white RTV appears to delay the onset of the thermal distortion without adversely affecting the frequency response. Therefore, most transducers are coated with a thin layer of RTV to differentiate between the expansion fan and the thermal distortions.

Photomultiplier tubes (PMT's) provide time-resolved broadband emission measurements. Three different PMT's, each in a different configuration, monitor three spectral regions. A solarblind CsTe PMT views the flow through a quartz window, with approximately 2° field of view. The spectral response is limited by the transmission of the window and the spectral response of the PMT to about 250-350 nm, the hot bands of the Schumann-Runge system. The solarblind KBr configured for VUV absorption measurements is also sensitive to test gas emission (see below). The spectral response is approximately 125-165 nm, and includes both molecular (Schumann-Runge) and atomic (resonance triplet) emission. Finally, a side-on PMT (Hamamatsu R456) with a 0.25 mm (0.010 inch) slit provides a time-resolved measurement of the emission entering the spectrometer/OMA described below. With a long-pass filter (RG780 Schott glass) placed in front of the PMT, the spectral bandpass is 750-900 nm. The emission in this region of the infra-red is dominated by atomic oxygen lines.

In the first series of measurements, a spectrometer with a gated intensifier records the spectra at various time delays behind the incident shock at Station E (Fig. 3.3). A

500 mm focal length MgF_2 lens images the test section onto the spectrometer entrance slit. The 50 mm diameter lens operates at f/20, and chromatic aberration is thus minimized by a large depth of field and the small dispersion of MgF_2. The 0.3 m McPherson 218 spectrometer contains a 150 ln/mm grating. A long-pass filter (OG530 Schott glass) discriminates against second-order lines. The entrance slit is 50 microns and an intensified diode array (Princeton IRY-700) is mounted at the exit. Diode array elements are spaced at 25 microns, but the intensifier smears the signals out over adjacent pixels so the effective resolution is about 1.5 nm. A beamsplitter just before the spectrometer directs a sample of the beam onto the slit of the R456 PMT described above.

A gated intensifier acts as a shutter for the spectrometer. The port across from the spectrometer at Station E contains a window to verify alignment, so neither a pressure transducer nor an ionization probe is available at E to detect the shock arrival. Consequently, the ionization probe at D triggers a delay generator (Stanford Research Systems) which then triggers a high-voltage pulse generator (Princeton Instruments FG100). A 200 V pulse from the FG100 gates the intensifier for 2.8 μsec. A trace from the pulse monitor output records the timing of the gate pulse.

A tungsten filament lamp (Eppley Laboratories) provides an absolute intensity calibration for the spectrometer/OMA and collection optics. A glass lens images the tungsten filament at unit magnification on the center of the shock tube so that a subsequent image is formed on the entrance slit of the spectrometer. The image of the filament overfills the slit in both height and width. Calibrations are performed with a shock tube window installed between the shock tube and the collection optics, but with no window between the lamp and the shock tube. Calibration data is corrected for fresnel losses (8%) of the glass lens. Emission from the lamp is weaker than from the shock tube, so measurements of lamp emission are accumulated over 1000 gate intervals. Measurements with the diode array show accumulated spectra are 30-40% higher than single-shot spectra, apparently due to image persistence on the detector (Snelling, et al, 1989). Consequently, single-shot measurements are also made to correct for this effect.

All data is collected by a CAMAC data acquisition system controlled by a Macintosh computer. Three banks of four A/D channels are available. The 4208 channels are 8-bit digitizers with amplifiers. Traq H channels are similar, but have more storage capacity and sample at 200 Msamples/s. The Traq I channels do not have amplifiers and only sample at 2 Msamples/s, but have 12-bit resolution. The CAMAC crate is controlled by a Macintosh operating under LabView. Binary data files are stored on the Macintosh, and data is analyzed with Igor, a graphics and analysis package from Wavemetrics.

The most appropriate arrangement of instrumentation was reached by incremental changes between shock tube runs, and is shown in Table 3.2. Differences between the arrangements for the first series of measurements (Case A) and the second series (Case B) are due to differences in testing requirements and facility test conditions.

Table 3.2. Summary of shock tube instrumentation.

Station	Case A		Case B	
A	Ion probe	Broadband PMT	Ion probe	Broadband PMT
B	Ion probe		Ion probe	
C	Ion probe		Ion probe	PCB 113A24*
D	Ion probe	PCB 113A24	Ion probe	PCB 113A24*
E	CsTe PMT	OMA, R456 PMT	CsTe PMT	PCB 113A24*
F	VUV	VUV	VUV	VUV
	Ion probe	PCB 113A21	Ion probe	PCB 113A24*
G	Ion probe	PCB 113A24*		

* Indicates a pressure transducer with RTV coating.

3.1.4 Facility operation

The driver conditions for this test are well within the normal operating range for the conical driver. The driver is loaded to 100 psia with 99% pure helium. An 1100, "0"-temper aluminum diaphragm, 0.30 mm (0.012") thick, initially separates the driver and driven sections. The capacitor bank is configured for 861.3 μF and charged to 10.5 kV for Case A and to 6.0 kV for Case B. A 0.17 mm (0.0065") diameter tungsten trigger wire initiates the discharge.

Operational procedures for the driven tube are designed to provide a high purity test gas. The driven tube is pumped out overnight (16-18 hours) by a turbo pump backed by a mechanical pump to an ultimate pressure of typically 2×10^{-5} torr, limited by an outgassing rate of typically 10^{-4} torr/min. The test gas is 99.993% pure oxygen from Liquid Carbonics. Impurity concentrations in the test gas are typically $N_2 < 10$ ppm, $H_2O < 3$ ppm, and THC < 1 ppm. Initial pressure in the driven section (P_1) is 1.00 torr for Case A and 0.30 torr for Case B. Loading is completed within a minute after the pumps are valved off, and the facility is fired approximately five minutes later. After each shot, glass and quartz windows are removed and cleaned in an ultrasonic bath. The MgF_2 windows used for VUV measurements are also cleaned in an ultrasonic bath, then wiped with spectroscopic-grade acetone and alcohol. The driven tube is swabbed repeatedly with

alcohol using lint-free rags. After re-assembling the driver and replacing the diaphragms, the shock tube is closed up and pumped out for the next shot. The time required to rebuild the driver, clean the driven section, and pump out the driven section limit facility operations to one shot per day.

3.2 VUV absorption measurement

The equipment for the VUV absorption measurement consists of the pump laser, Raman shifter, optics for beam delivery, and detectors. The Raman shifter is discussed first, and then the implementation of the system.

3.2.1 Raman shifter

The appeal of Raman shifting for wavelength conversion is the relative simplicity of the equipment. Preliminary work with a doubled Nd:YAG laser was performed with an atmospheric-pressure hydrogen cell. The cell was simply a steel tube with a fill line welded to the middle and quartz windows glued to the ends with TorrSeal. Although optimum conversion occurs at much higher pressures, the fifth anti-Stokes component was readily observed on a fluorescent card with this arrangement.

The cell design is more complicated if liquid nitrogen cooling and vacuum ultraviolet operation are required. Water will condense on cold windows exposed to air, so either the windows must be kept warm or held at vacuum. By cooling the center of the cell only, the windows at the ends remain near room temperature. Temperature gradients lead to circulation and beam steering effects. For vacuum ultraviolet applications, a vacuum is required for the exit window, so the entire cell is cooled and placed in a vacuum chamber.

Details of the Raman cell and vacuum enclosure are described in the following paragraphs and Fig. 3.4. All components are 304 stainless steel, except for the brass Belleville washers holding the cell windows. Windows are sealed to the cell with indium wire, 0.5 mm in diameter. The distance between cell windows is 69.6 cm, and the inside diameter is 3.8 cm. The entrance window is 50 mm in diameter by 9.5 mm thick and is Suprasil 2. The exit window is 5 mm thick and is single crystal MgF_2. To prevent back reflections, the front window is tilted 6° and the exit window is tilted 2°. The cell is wrapped in a liquid nitrogen jacket, filled from a line beneath the entrance window and vented through a line above the exit window. Three type-T thermocouples in 0.5 mm stainless steel sheaths monitor the temperature of the hydrogen in the cell. All feedthroughs are stainless tubing with 3.2 mm internal diameter.

The entire cell is housed in a vacuum enclosure, and is supported by the feedthroughs for the thermocouples and the liquid nitrogen purge. The cell is mounted in the enclosure by first sliding the enclosure flange over the feedthroughs on that side. The bulkhead fittings for the liquid nitrogen lines are carefully secured with a modified socket. Bulkhead fittings are attached to the lines via a thin bellows so that the O-rings at the bulkhead remain near room temperature. This positions the two thermocouple feedthroughs in their Cajon UltraTorr fittings. The cell, now mounted to the entrance flange, is inserted into the enclosure so that the third thermocouple feedthrough protrudes from the far end. This feedthrough slides through the UltraTorr bulkhead fitting on the exit flange. Both entrance and exit flanges are bolted to the enclosure to compress the O-rings, and finally the UltraTorr fitting on the exit flange is tightened.

Outside the enclosure, all feedthroughs are mated to UltraTorr fittings. The thermocouples are sealed with modified VCR fittings. The thermocouple is inserted through a hole drilled in the fitting, a small cross-section of a Viton O-ring, and a blank gasket with a hole punched in it. After inserting the thermocouple into the cell until it protrudes a few millimeters, the fitting is secured. One of the thermocouple feedthroughs on each end is a tee, and the third side of each tee is connected to the hydrogen fill panel or to a vacuum valve. The liquid nitrogen feedthroughs are connected to fill and vent lines via UltraTorr fittings. Although the fittings do not provide a vacuum seal when cold, the seal is sufficient to prevent liquid nitrogen from leaking.

Thermal cycling of the cell produces small leaks at the indium window seals. Varying rates of thermal expansion/contraction probably cause failure of the cold-welded joints between the indium and the steel cell or windows. Depending on the leak rate and pumping speed of the system, several problems can arise. Hydrogen pressure in the cell drops over time, but the leak rate is usually too small to be significant. If the pumping speed is insufficient to keep the vacuum pressure fairly low, convective heating of the cell becomes significant, and the photomultiplier tubes can be damaged by arc discharges between the high-voltage cathode and vacuum flanges at ground potential.

In a second seal design, a single-use indium gasket with a cross-section of 1 mm diameter is compressed by about 50%. This gasket is much thicker than the first design, under the assumption that it would be more resilient to differential contraction. To facilitate seal and/or window replacement, the custom brass Belleville washers are replaced by commercially-available washers on each bolt. Under repeated cycling, these seals also developed leaks. By cooling the cell slowly (at least one hour), the seal degradation is reduced substantially. Under further cycling, the leak rate increases and the ultimate pressure obtainable in the vacuum chamber increases. When the ultimate vacuum pressure

with the cell cooled approached 10^{-3} torr, the flange bolts are tightened slightly to further compress the gasket. Seal performance might be improved by using the pressure differential to continuously compress the gasket. Some additional complexity is involved, however, because the window must seal to the retaining flange which is then sealed to the cell.

3.2.2 Setup and operation

The layout for the VUV absorption measurement is shown in Fig. 3.5. The Raman shifter is pumped with an excimer laser. The collimated output beam is dispersed, and a reference measurement made before the beam passes through the tube. Transmitted light intensity is measured on the opposite side of the tube.

The pump source is an ArF excimer laser (Lambda Physik Model EMG-150ET). It has two chambers, and is operated in the standard injection-locked configuration. Three prisms and a grating serve as tuning elements for the laser. Oscillator wavelength is tuned by tilting the grating with a micrometer. The oscillator output coupler is coated for 50% reflectivity, and a pair of turning mirrors steer the beam into the amplifier through a hole drilled in the center of M5. The beam is expanded by reflection off of meniscus lens M6, and is re-collimated by mirror M5. When operating with other laser gases, such as KrF, M6 has a reflective spot in the center. Due to the lower damage threshold of coatings for ArF emission, M6 is uncoated and instead relies on fresnel reflection. The unstable resonator configuration injection locks the amplifier output, producing 100-125 mJ/pulse with relatively low divergence. The output beam profile is rectangular, approximately 22 x 9 mm, and has a diffraction spot in the center from the hole in M5.

The laser is typically operated at low repetition rates or in single shot mode, mitigating some of the common inconveniences associated with operation at 193 nm. Laser gas fills last a week or longer without an external gas processor. When the gas fill is replaced, however, the performance gradually improves over the first few hours before the slower deterioration begins. Color-centering of the chamber windows is not observed. Magnesium fluoride windows are recommended for the laser chambers because of their resistance to color-centering. However, stimulated Raman scattering is polarization sensitive, and the birefringence of MgF_2 can alter the polarization of the laser beam unless their orientation is carefully adjusted (Faris and Dyer, 1993). Calcium fluoride windows, which are not birefringent, are used instead. The fluorescence associated with color-center formation in calcium fluoride has not been observed.

The laser is triggered by the arrival of the shock front at Station F. The signal from the pressure transducer is fed to a digital oscilloscope (Tektronix 2440). When the shock

arrives, the pressure rise triggers the scope. A TTL level signal from the scope triggers a delay generator (Stanford Research Systems DG535). After a 5 μsec delay, a 35 V trigger pulse is sent to the laser. A small capacitor is placed across the pulse to increase the pulse duration. The delay generator also triggers the data acquisition channels for the two solarblind photomultipliers. In Case B, the pressure signal is lower and is more susceptible to false triggers from facility-generated RF interference; triggering from the ion probe at Station F is more reliable for these measurements.

All optics before Raman shifting are Suprasil 2, and those after are single crystal MgF_2 with the c-axis directed parallel to the beam.* A dielectric mirror directs the excimer beam through a focusing lens (f=460 cm at 193 nm) and into the Raman shifter. The window on the vacuum enclosure is 9.5 mm thick and is anti-reflection coated at 193 nm. The cell window is of the same dimension, but is not coated because the coating would be damaged if the window were removed. In the focal volume inside the Raman cell, various Stokes and anti-Stokes beams are generated. The emerging beams are collimated by a MgF_2 lens (f=500 mm at 250 nm, f≈361 mm at 130 nm). Ideally, the distance between the two lenses is selected to collimate the sixth anti-Stokes beam. Due to design changes, however, the minimum possible distance between the lenses is about 50 mm larger than desired. The ArF beam is still diverging, and the sixth anti-Stokes is mildly converging and comes to a focus about 3 m after the cell. Although this is not an optimal arrangement, the effect on the absorption measurements is probably small because the focus occurs beyond the shock tube and also because intentional tilting of the entrance lens and aberrations prevent the beam from focusing sharply. After the cell, a 30° prism provides dispersion. The beams pass through a series of apertures to select the sixth anti-Stokes component, and then through a second prism and additional apertures to eliminate scattered light.

Once separated from the other orders, the sixth anti-Stokes component goes to the shock tube. A VUV mirror steers the beam to the test section. An uncoated MgF_2 beamsplitter samples the beam before it enters the test section. This beamsplitter is slightly wedged to minimize etalon effects. The remaining beam passes through the shock tube windows, which are 8 mm thick. Slots in the port plugs holding the windows limit the field of view. Each slot is 7.9 mm wide and 17.0 mm high.

Both the reference and transmitted intensities are measured with solarblind photomultipliers (Thorn-EMI). The photocathode material is KBr, whose quantum

---

* Index of refraction and absorptivity data for magnesium fluoride are reported by Williams and Arakawa (1979).

efficiency at 193 nm is about two orders of magnitude smaller than for 130 nm. High-speed preamplifiers inside the photomultiplier housings reduce the effect of RF noise from the laser. The signals are sent to the data acquisition system via double-shielded cables, terminated at 50 Ω, and sampled at 5 nsec intervals. In the second series of measurements (Case B), the traces are recorded on a digital oscilloscope (Tektronix 2440), providing several advantages. Primarily, amplifiers and digitizers are integrated in a single package, substantially reducing susceptibility to RF noise from the laser. Additionally, the scope samples at 2 nsec intervals and provides 100 and 20-MHz filters to further reduce high-frequency noise.

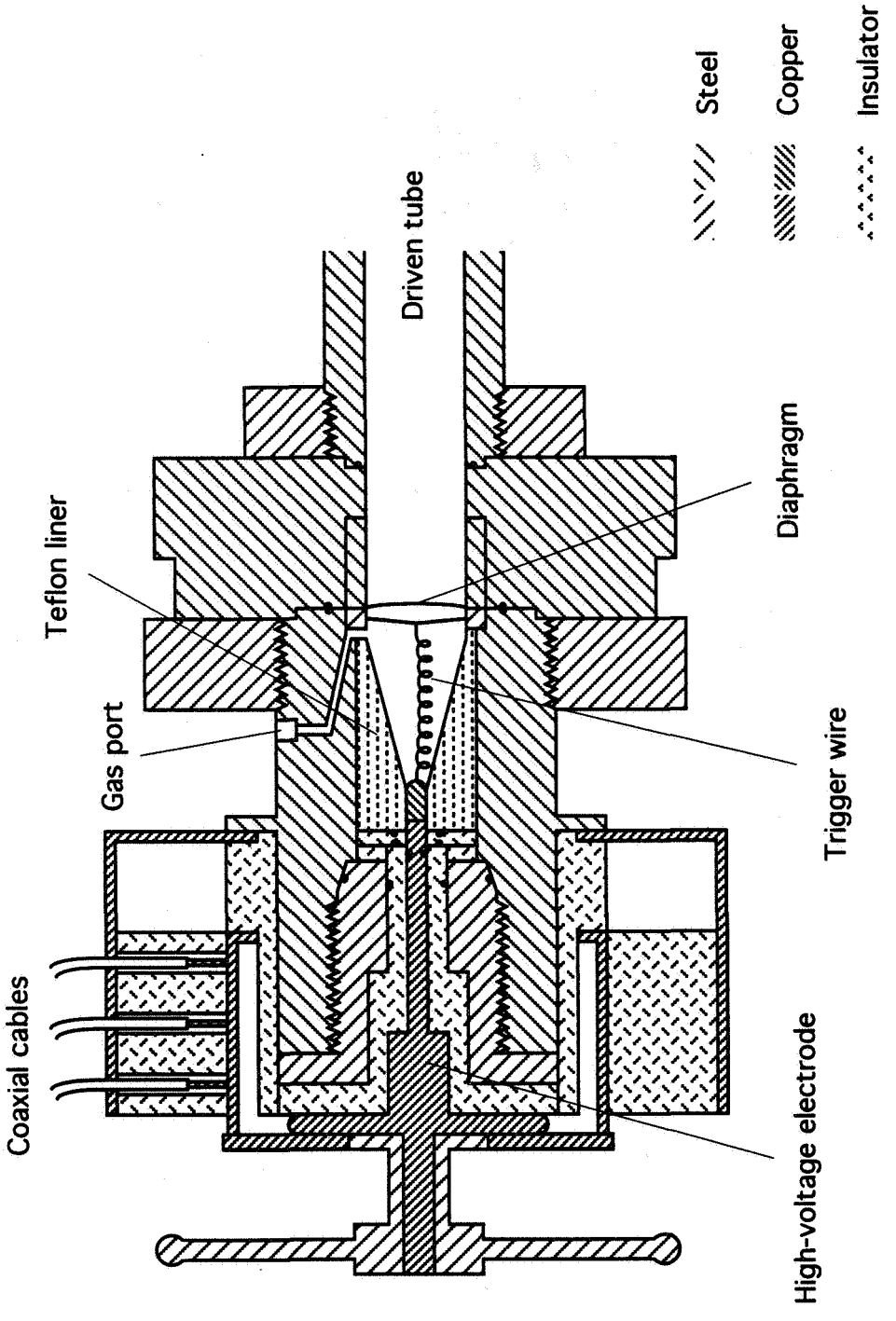

Figure 3.1 Schematic drawing of conical driver section.

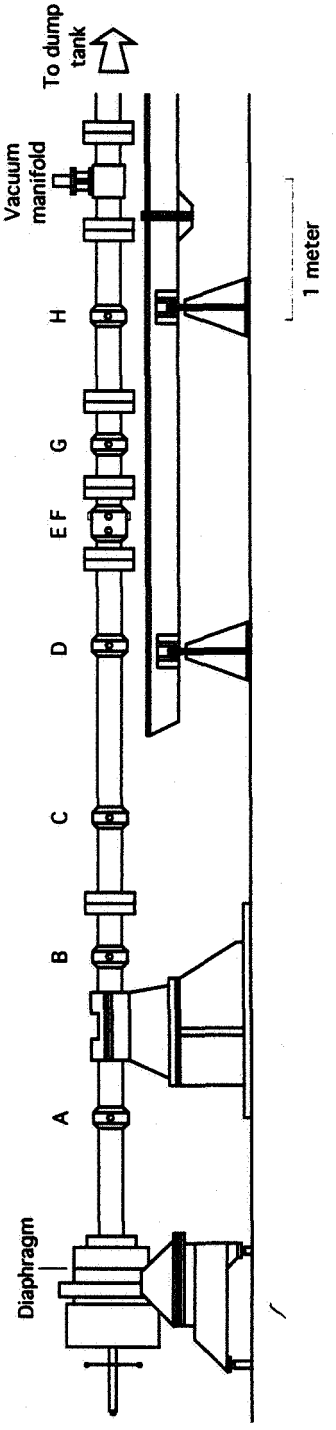

Figure 3.2 Layout of Electric Arc-driven Shock Tube showing relative position of instrumentation ports.

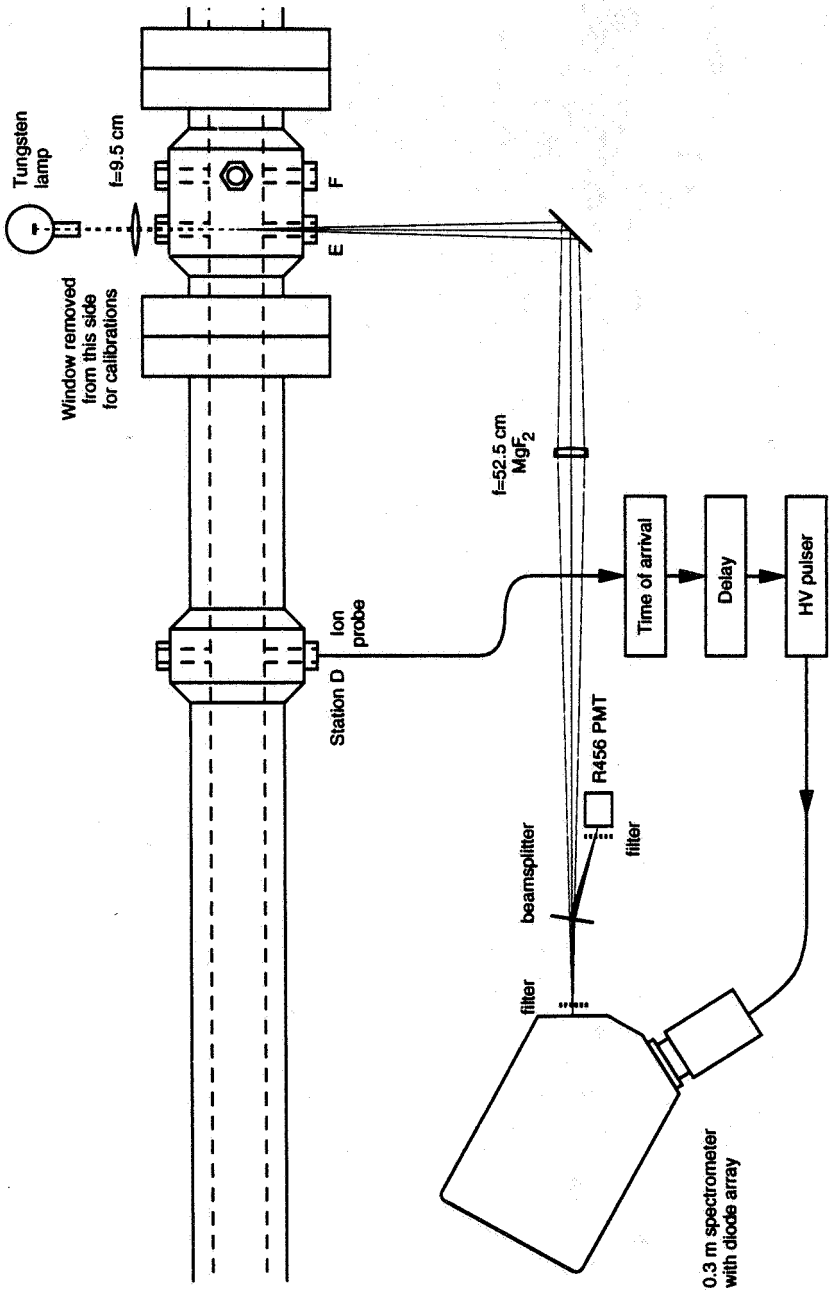

Figure 3.3 Layout for collecting spectra of test gas.

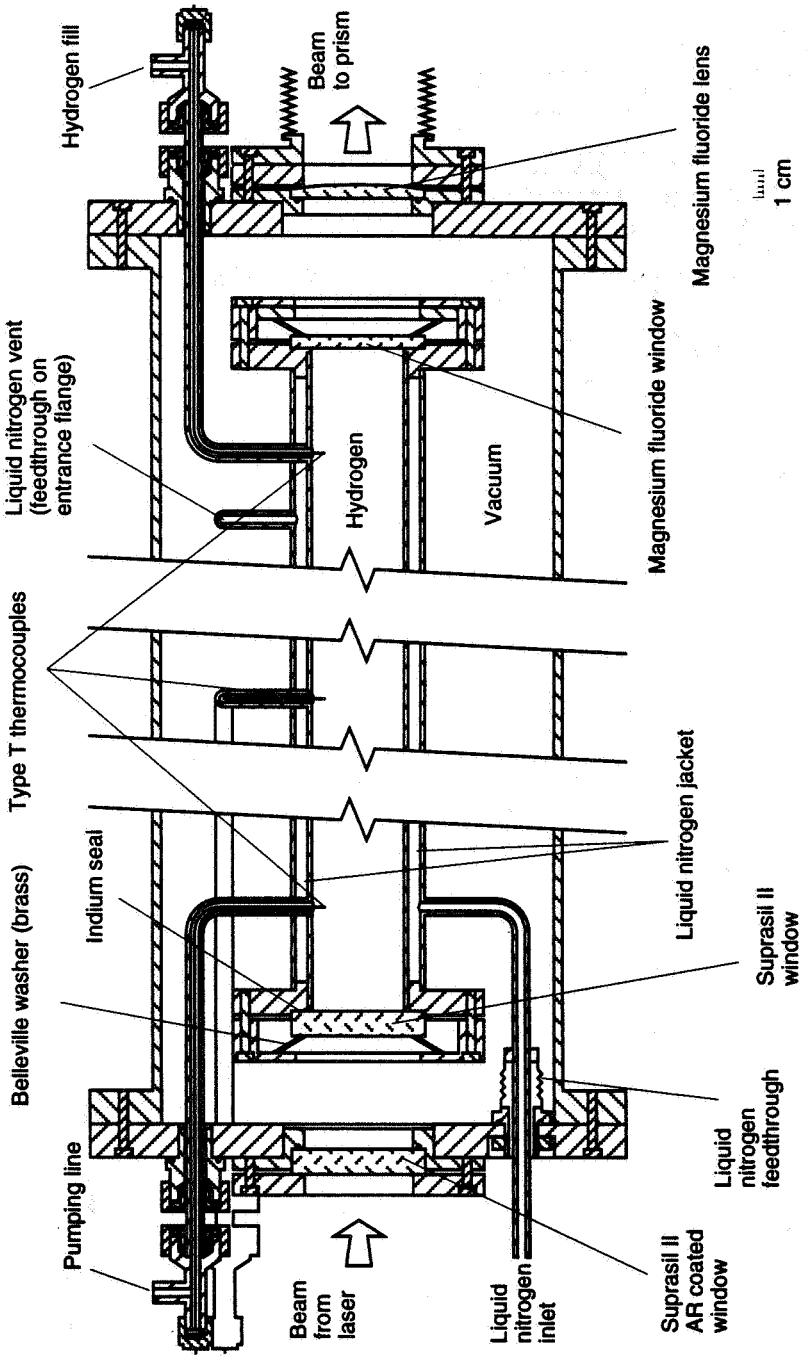

Figure 3.4 Schematic drawing of Raman cell and vacuum enclosure.

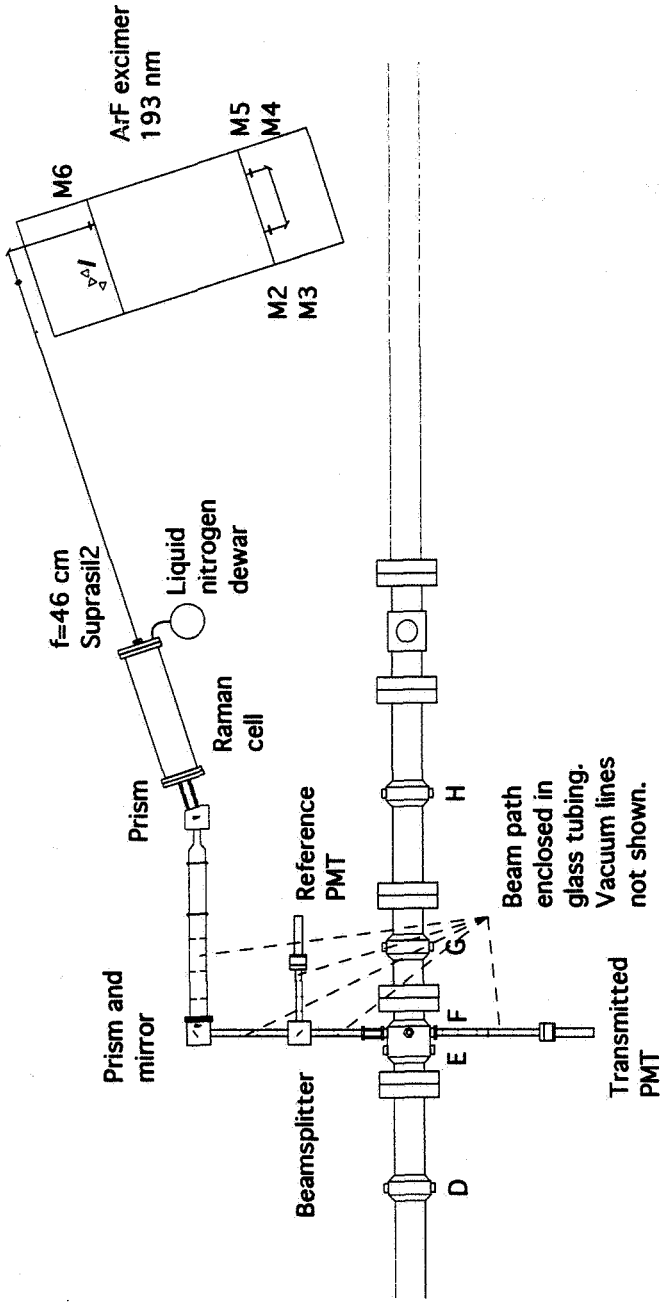

Figure 3.5 Schematic of vacuum ultraviolet absorption diagnostic showing layout of optics in relation to shock tube. Connections to vacuum pumps not shown.

Chapter 4
Experimental Measurements

Results of the experimental measurements are presented in this chapter. Characteristics of the vacuum ultraviolet light generated by the Raman-shifted laser are described first. Results of the shock tube measurements follow, with an evaluation of the flow properties followed by results of the transmission measurements.

4.1 VUV light source

4.1.1 Spectral purity

A monochromatic source of light is required for spectral absorption measurements. Before evaluating the wavelength and line width of the probe beam, the spectral purity of the beam must first be determined. The desired light is produced by the 6th anti-Stokes Q-branch for J=1. Light leaving the Raman cell, however, is far from monochromatic. It contains residual pump energy at 193 nm and various orders of Raman-shifted light at wavelengths both longer (Stokes) and shorter (anti-Stokes) than the pump wavelength. In the region near 130 nm, the Q-branch may be flanked by O and S branches, and contributions from J=0 and/or J=2 may also be present. Finally, the desired Q-branch contains contributions from both the narrowband (injection-locked) and broadband (amplified spontaneous emission, ASE) components of the ArF pump beam.

The spectral composition of the probe beam is analyzed with a 0.3 m scanning monochrometer. Measurements are performed by replacing the beamsplitter box with the monochrometer. Light from the Raman cell passes through two dispersing prisms and a 12 inch segment of glass tubing with the same apertures used for the absorption measurement. The entrance slit of the monochrometer is much smaller than the beam profile, so a MgF_2 diffuser is placed in front of the slit. The monochrometer is a 0.3 m McPherson 218 with

a 2400 ln/mm grating blazed at 150 nm. Although the spectral response of the monochrometer optics are not known, the peak response will be at a wavelength of 150 nm or longer. In addition, the grating reflectivity is almost certainly lower at 130 nm than at longer wavelengths, so that this is a conservative measurement. A KBr photomultiplier later used for the absorption measurement detects the light, so its spectral response does not affect the measurement.

The objective of these scans is to determine the presence of light at wavelengths other than that desired, that is, the J=1 Q-branch of the 6th anti-Stokes line. Data is collected by repeatedly firing the laser while scanning the spectrometer. A high resolution scan of the entire VUV region is extremely time-consuming. However, high resolution is only needed near 130 nm to discriminate between various features. At significantly shorter and longer wavelengths, less resolving power is required to differentiate between the desired light at 130 nm and stray light at any given wavelength.

Low, medium, and high resolution scans are performed. Noise in the spectral scans arises from shot-to-shot variations in Raman cell output; the scan speed is selected so that several shots are averaged at each wavelength. Spectral resolution for each scan is different, so the apparent width of the Q-branch is different in each scan. The Q-branch is in fact, more narrow than indicated by any of the scans. Neither residual pump energy nor anti-Stokes orders are visible in the low resolution scan shown in Fig 4.1. A medium resolution scan of the 6th anti-Stokes region shows that the Q-branch is much more intense than either the O or the S branch, which are not observed above the background level (Fig. 4.2). The high resolution scan in Fig. 4.3 shows that only the J=1 Q-branch is present, but also that a broadband pedestal lies beneath the narrowband component.

Comparison of the ArF beam to the VUV beam reveals that this pedestal is produced by the broadband ASE component of the laser. When the laser wavelength is changed, the narrowband VUV component moves with it (Figs. 4.4a-f). The broadband remains fixed, however, demonstrating that it is not an artifact of the monochrometer instrument function. A convenient parameter to describe the relative proportions of narrowband and broadband light is the locking efficiency. Locking efficiency is defined as the fraction of the total laser energy which is in the narrow bandwidth defined by the oscillator beam. The ratio of the broadband to narrowband VUV is correlated with the locking efficiency of the ArF beam. Figure 4.5a shows the ArF spectrum at 55% and 85% locking efficiency. Figure 4.5b shows that the Raman-shifted light follows the same trend. Thus, when the ArF beam is not completely injection-locked, it contains broadband ASE which produces a broadband component at 130 nm. Comparison of the broadband/narrowband ratio is difficult because of the dynamic range required to measure

the amplitudes of both components at 130 nm. Comparison of the spectrally-integrated intensities suggest that the ratio at 130 nm is the same as for the ArF pump beam at 193 nm. This comparison may not be valid, however, because the dynamic range of the oscilloscope may have been exceeded in a manner that does not lead to obvious saturation of the signal level (see Section 4.3.1). From these measurements, then, one concludes that both broadband and narrowband light are shifted to the VUV and that the ratio of the two is related to laser locking efficiency. However, neither this ratio nor its dependence on various pumping parameters, such as beam energy or hydrogen density, is determined from these measurements.

These measurements indicate that locking efficiency of the laser is an important parameter in determining the broadband component of the 130 nm beam. During the second series of measurements (Case B, low density), laser locking efficiency is measured with an OMA on every shock tube run. Atomic absorption measurements indicate, however, that broadband light is not a significant error source in the final absorption measurements.

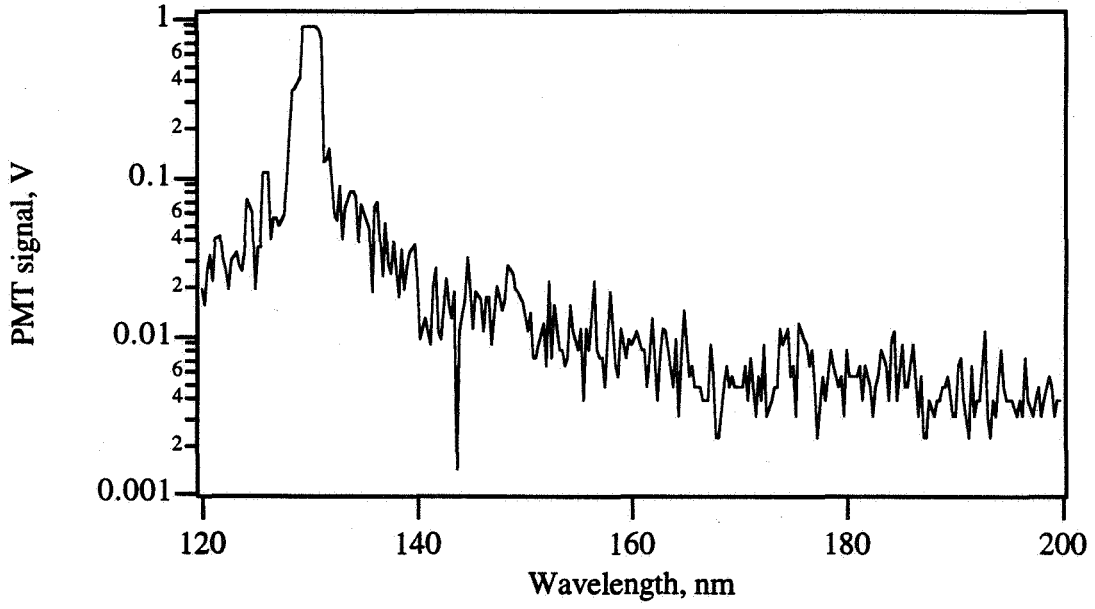

Figure 4.1 Low resolution scan of Raman-shifted light.

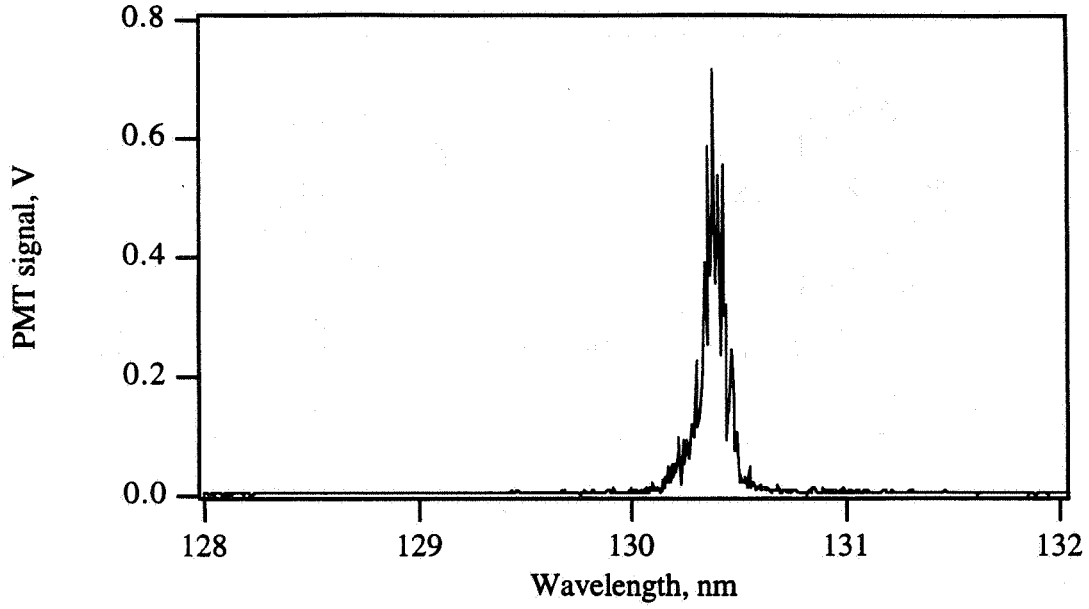

Figure 4.2 Medium resolution scan of Raman-shifted light.

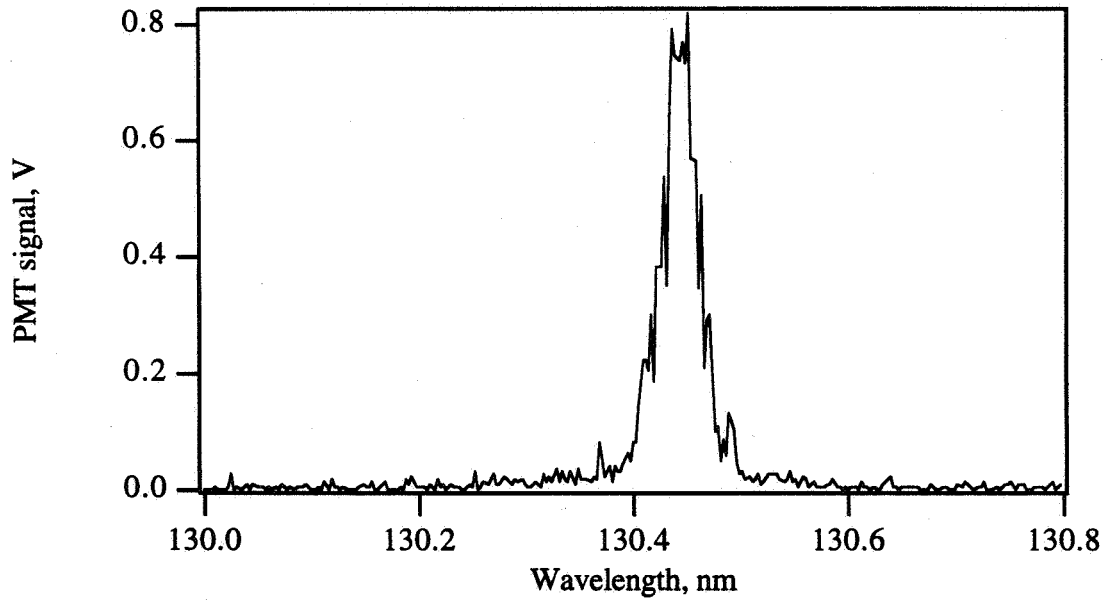

Figure 4.3 High resolution scan of Raman-shifted light.

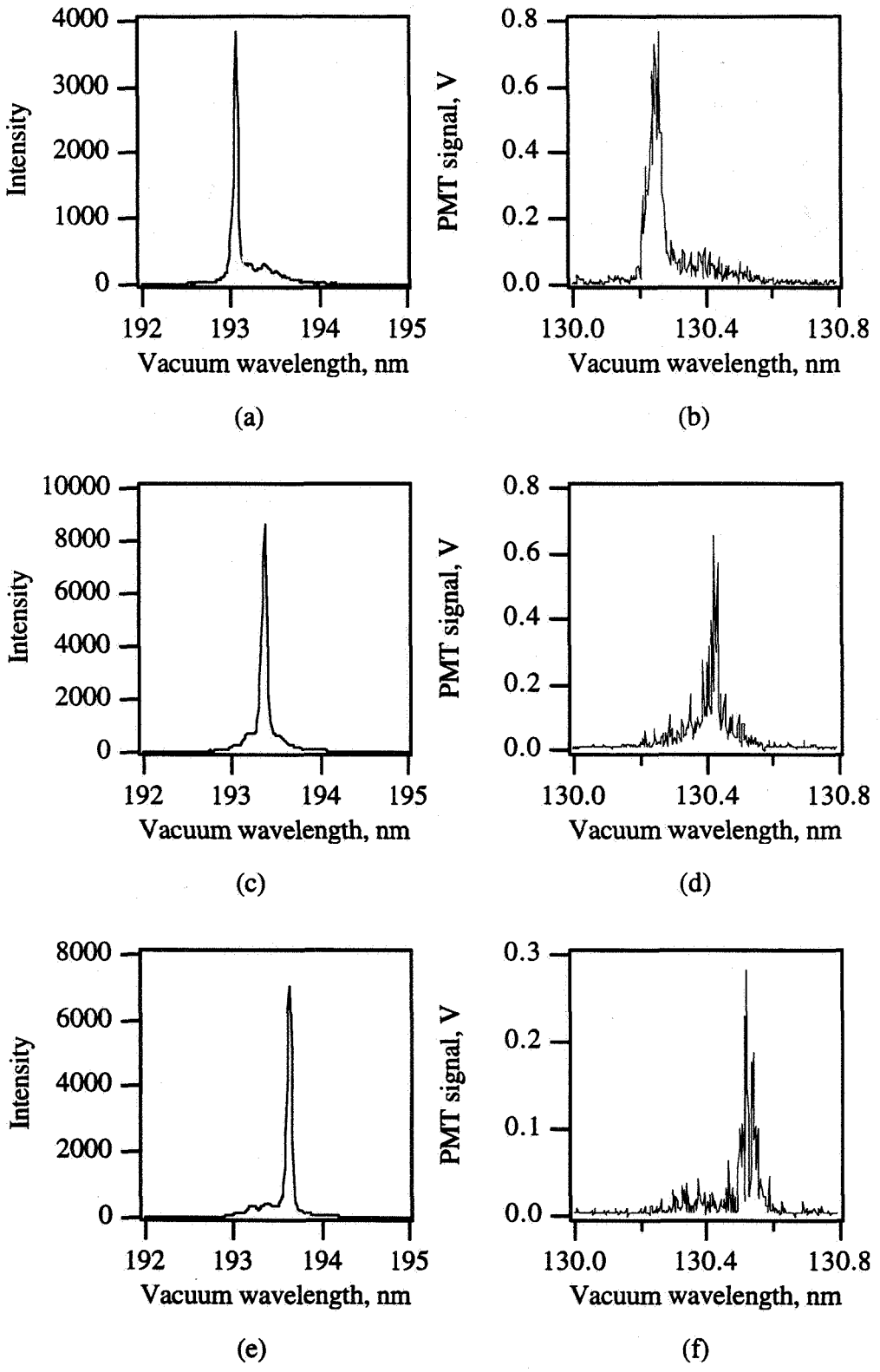

Figure 4.4 Comparison of 193 nm and 130 nm light at various wavelength tunings of the ArF pump laser.

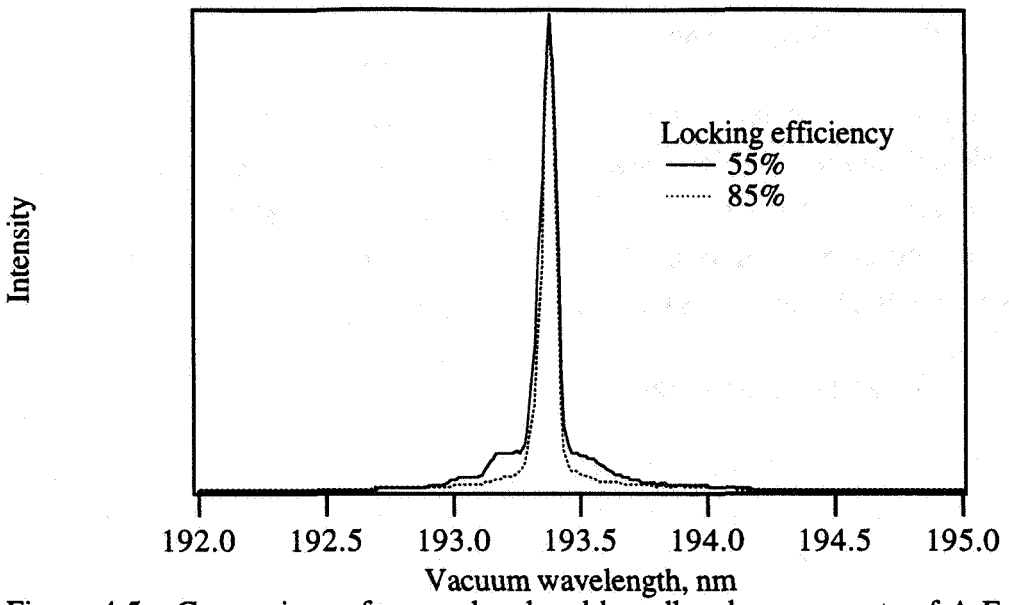

Figure 4.5a Comparison of narrowband and broadband components of ArF pump laser light at two different locking efficiencies.

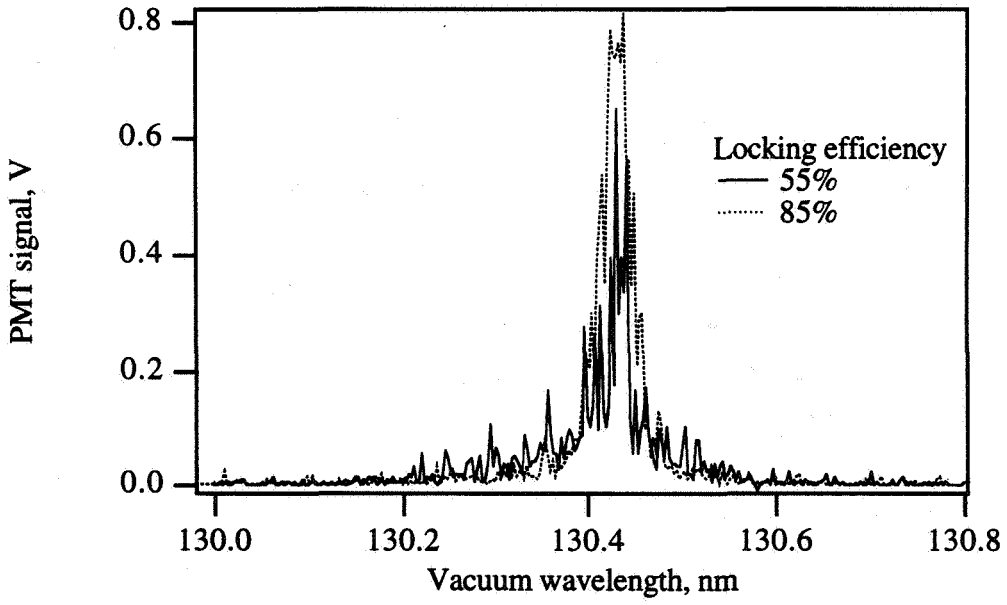

Figure 4.5b Comparison of narrowband and broadband components of 6th anti-Stokes light at two different locking efficiencies.

4.1.2 Wavelength calibration

Two types of wavelength calibration are performed. First, a calibration of the pump wavelength can be used in conjunction with the hydrogen Raman shift to calculate the wavelength of the VUV beam. Alternatively, the VUV wavelength can be found directly from an absolute calibration of the VUV wavelength. The first approach is simpler experimentally, but the second provides higher accuracy.

4.1.2.1 ArF pump wavelength

The wavelength of the pump beam at 193 nm can be determined from the absorption spectra of molecular oxygen in room air. A scan across the gain profile of ArF reveals several strong absorptions due to the Schumann-Runge band system, and a detailed photographic atlas of this system has been prepared by Yoshino, *et al* (1984). At room temperature, three features due to the (4,0) band are particularly suitable for wavelength calibration. Each feature consists of a line pair due to the P and R-branches. Although each of these lines is further split into hyperfine levels, they are not resolved by the laser.

Calibration scans are performed by measuring the laser output power after a path length of 2.6 m, as shown in Fig. 4.6. Absorption dips are related to the micrometer reading on the laser's tuning grating. The accuracy of this method is limited to approximately 0.5 cm^{-1} by several effects. Locking efficiency of the laser is not constant because the oscillator energy is lower at the absorption peaks. Additionally, fluctuations in the laser power and locking efficiency lead to uncertainty in the peak positions. These two difficulties can be overcome, but pre-dissociation broadening of these peaks is appreciable and limits the ultimate accuracy of this method. For more precise measurements of the 193 nm wavelength, other spectral features provide higher accuracy (Faris and Dyer, 1993). When required, precise wavelength calibration is performed directly in the VUV, as described in the next section.

After determining the pump wavelength, the 6th anti-Stokes wavelength is calculated from the hydrogen Raman shift. For the J=1 Q-branch, the shift is 4155.25 cm^{-1} per step, or 24931.5 cm^{-1}. This neglects small variations in the transition frequency caused by collisions or by high beam intensities in the focal volume (Bischel and Dyer, 1986(*a*), and Faris and Dyer, 1993). This method is applied to the high density case because it is simple and sufficiently accurate for this test condition.

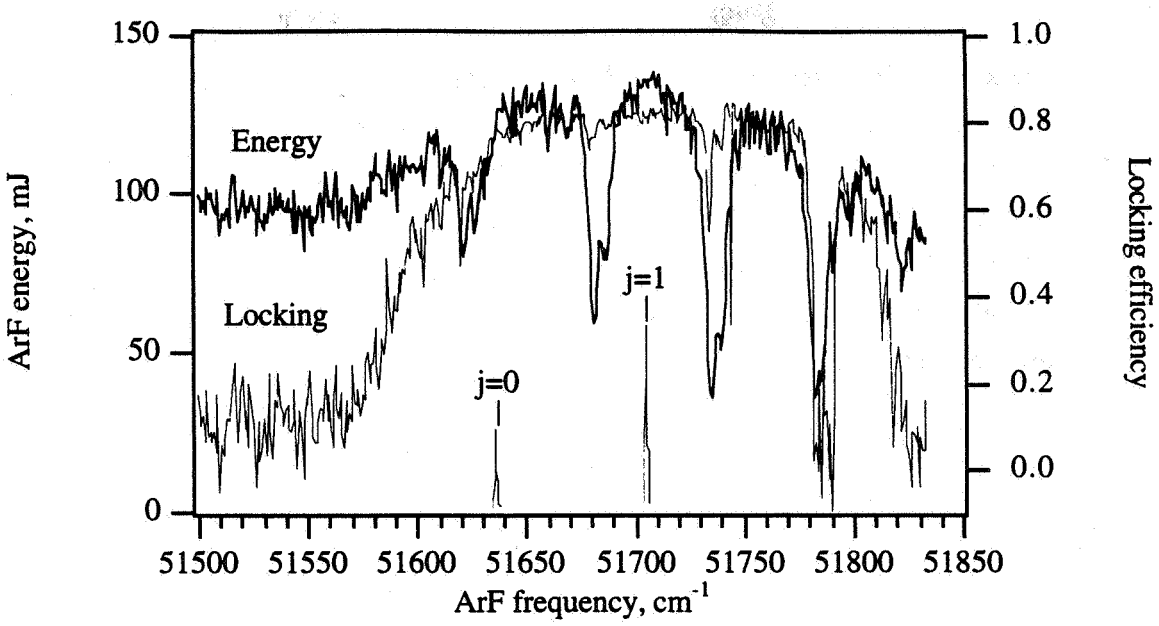

Figure 4.6 Pulse energy and locking efficiency of the ArF laser showing the positions of room air absorption (molecular oxygen) and the positions of two atomic oxygen emission lines detected by LIF in the flow cell.

4.1.2.2 VUV flow cell measurement

A direct measurement of the VUV wavelength is required for the low density case, and a microwave discharge flow cell provides a straightforward wavelength standard (Bischel, *et al*, 1982, and Döbele, *et al*, 1986). A 5% mixture of prepurified N_2 in Ar (99.999%) is excited by a microwave discharge, producing N atoms. A 5% NO/Ar mixture is introduced downstream of the discharge, producing O atoms by an exchange reaction. The NO flow rate is very low so that virtually all of the NO is consumed. This flow enters the top of a six-way cross which is pumped through the bottom port. The VUV beam travels horizontally, entering and exiting through MgF_2 windows, and a KBr PMT views the laser-induced fluorescence (LIF) signal at right angles to the beam. No baffles are placed in the flow cell, nor is the interaction volume imaged onto the PMT. However, the tube diameter is 2.5 times larger than the beam apertures, and the LIF signal is easily distinguished from the scattered light.

Flow cell calibrations of the absolute wavelength are performed before every test. By adjusting the oscillator grating on the ArF laser, an LIF scan is performed to locate the center of the 130.49 nm line (j=1 in Fig. 4.6). After finding this absolute wavelength reference, the laser is tuned the desired distance from the line center. To prevent hysteresis and backlash of the grating, the LIF scan is performed by approaching the line center from

the opposite side and continuing to the desired wavelength for each shock tube run. After the test, the laser scan is continued in the same direction to find the next absorption dip in ArF power due to atmospheric oxygen, which determines the relative wavelength calibration. Accuracy of this method is essentially limited only by the laser linewidth near the center of the line, with the uncertainty increasing with distance from the line center. Far from the line center, however, the absorption measurements are much less sensitive to the wavelength calibration errors, so this method provides sufficient accuracy for the absorption measurements.

Preliminary attempts to observe the lifetime of the upper state have been unsuccessful because the upper state lifetime is 2.5 nsec, and the acquisition rate of the oscilloscope is 2 nsec/sample. Additionally, the LIF signal is substantially larger than the scattered light signal, so different PMT voltages are required to observe the two signals. Voltage-dependent changes in the PMT pulse shape (transit-time spread) further complicate the lifetime measurement. However, observation of the lifetime is not required to identify the LIF signal, so this does not affect the wavelength calibration accuracy.

4.1.3 Probe beam linewidth

Like wavelength calibration, determination of the VUV linewidth can be approached by inferring the linewidth from ArF measurements or from a direct measurement at 130 nm. Direct measurement is preferable because pressure and power-broadening corrections to the ArF linewidth are not required.

Oxygen atoms generated in the flow cell provide a narrow reference line to scan. Typical discharge conditions are 70 W of power into 18 torr N_2/Ar, producing a faint orange glow downstream of the discharge. Variation of the LIF signal with the amount of NO/Ar added to the flow is shown in Fig. 4.7a. With only the N_2/Ar mixture, flow cell pressure is 18.07 torr. By slowly opening a needle valve, the NO/Ar flow rate is increased and the cell pressure rises. Initially the LIF signal increases, presumably due to an increase in the number density of O atoms. As more NO is added, the signal level plateaus, and then drops below the noise level. Disappearance of the signal is probably related to absorption of the beam before reaching the probe volume and trapping of the fluorescence. Although the number density of O atoms can be ascertained from titration measurements, a rough estimate is sufficient for the linewidth measurement. Assuming complete conversion of NO into O atoms, neglecting recombination at the walls, and assuming a uniform mixture leads to an upper limit estimate on the order of 10^{14} cm^{-3} O atoms.

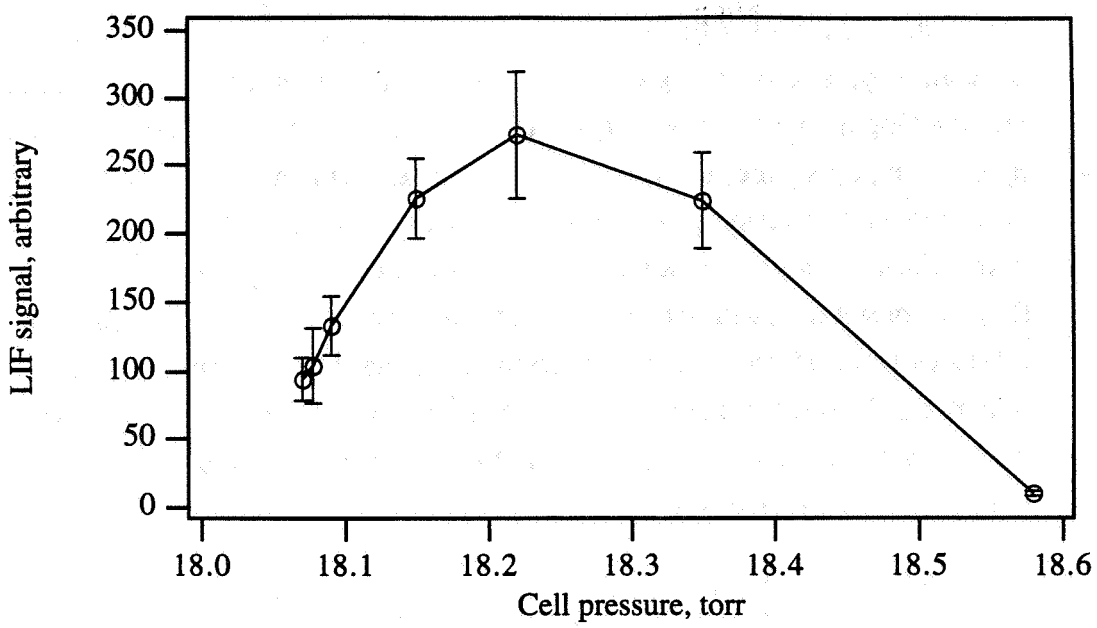

Figure 4.7a Variation of O atom LIF signal with various partial pressures of NO added. Initial pressure is 18.07 torr of Ar/N_2 mixture without NO.

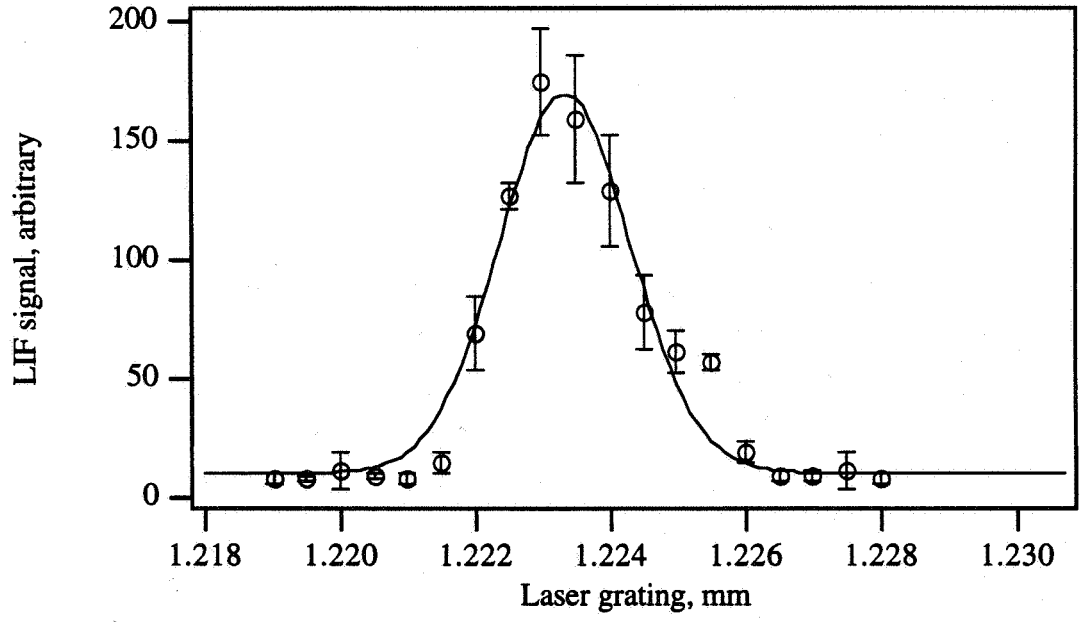

Figure 4.7b LIF scan of 130.49 nm atomic oxygen line in microwave discharge flow cell.

Scans across the line at 130.49 nm produce profiles like that shown in Fig. 4.7b. The profiles typically exhibit asymmetry, like that shown in the figure. Despite the asymmetry, a Gaussian profile is fit to the data to estimate the linewidth. This width is a

convolution of the VUV linewidth with the atomic resonance. At the operating pressure in the cell, Doppler broadening dominates. Assuming a translational temperature of 300 K yields a Doppler width of only 0.24 cm^{-1}. Since a convolution of Gaussians is performed by summing the squares of the widths, the Doppler width makes a small contribution to the measured width. Various optical effects, such as attenuation of the pump beam, saturation of the transition, and fluorescence trapping, will produce additional apparent broadening if they are present. As the concentration of NO/Ar is increased, the Gaussian linewidth increases from 0.9 to 1.1 cm^{-1}. Therefore, the measured width of 0.9 cm^{-1} is an upper limit to the linewidth of the probe beam. Since this value is consistent with expectations for the width of the original ArF beam at 193 nm, a value of 0.9 cm^{-1} is adopted for the linewidth of the probe beam.

4.1.4 Spectral tuning range

Pumping a Raman cell with a tunable laser produces tunable light in the various Raman orders. The tuning range of each Raman order is roughly the same as that of the pump laser, when the range is expressed in frequency or energy units. In practice, the observed tuning range of high-order lines is smaller because the output power of the pump laser is usually lower in the wings of the gain profile. For ArF, the locking efficiency is highest near the center of the gain profile, and decreases as one moves away from the center. An exception occurs at 51789 cm^{-1}, near one of the O_2 line pairs, which has been attributed to absorption by carbon atoms (Faris and Dyer, 1993). In the wings of the profile, the poor locking efficiency does not prohibit conversion, but it does lead to lower conversion efficiency and perhaps to a Raman-shifted beam with a larger broadband component. Total output power and locking efficiency are shown in Fig. 4.6. Noise in the measurements is produced by scatter in the power meter measurements and shot-to-shot fluctuations in laser output. Unfiltered results are shown to demonstrate the scatter involved in single-shot measurements of laser performance. Results of LIF scans of O atoms in the discharge cell are included also (on an arbitrary intensity scale). The tuning range is sufficient to excite fluorescence at 130.49 (j=1) and 130.60 nm (j=0), but not at 130.22 nm.

Tunability of the Raman cell is also limited by the oxygen absorption features in the ArF spectrum. The Schumann-Runge absorption features described previously produce gaps in the tuning range. Within the laser head, atmospheric oxygen attenuates the oscillator beam, reducing the locking efficiency of the laser. The output beam is further attenuated by absorption in the path from the laser to the Raman cell. In this experiment, laser placement is dictated by space considerations in the facility; consequently, this absorption is not trivial.

Several steps can be taken to increase the spectral tuning range. The width of the tuning range (and the locking efficiency as well) can be improved by increasing the oscillator beam energy. This can be accomplished by replacing the tuning grating with a mirror, seeding with a separate laser system, or converting from an unstable resonator to a multi-pass amplifier. These alternatives come at the price of increased linewidth or additional expense and complexity. Gaps in the tuning range can be reduced by purging oxygen out of the beam paths. A steady flow of clean nitrogen or argon within the laser head can improve the locking efficiency, and a purged beam path can reduce absorption of the output beam. Clean gases must be used, however, because contaminants impinging on the optics will be burned in by the laser beam.

4.1.5 Statistical intensity variations

The 6th anti-Stokes component is produced by a series of nonlinear processes, so that the beam intensity varies substantially from one pulse to the next. The range of fluctuations depends on a variety of parameters, such as focal intensity and hydrogen pressure. In the current experiments, the intensity varies over a factor of five to ten.

For a single-shot absorption measurement, the incident beam intensity must be known. A reference photomultiplier measures the intensity before the beam enters the shock tube. Calibration shots are performed before every test so that the incident signal intensity, I_o, can be deduced from the reference signal. Calibrations from Run 87 are typical; they are shown in Fig. 4.8. The calibration shots exhibit significant scatter, and the standard deviation is typically 10%. For each shock tube run, 100 shots are collected and averaged. This provides a statistically averaged value for the calibration factor. Scatter in this data, however, reflect an imperfect correlation and, thus, an uncertainty in the value of I_o for a single-shot measurement.

Uncertainty in I_o is the largest uncertainty in the absorption measurements. No specific mechanism for the scatter was determined, although several attempts have been made to eliminate it. Diffusers are placed several inches before the photomultiplier tubes to mitigate the effect of photocathode non-uniformities. An aperture of the same shape as the shock tube window is placed before the reference tube to eliminate the effect of spatial variations in the beam profile. Finally, the beamsplitter box and reference leg are rotated 90 degrees into a vertical tower to reduce fluctuations in the reference intensity produced by variations in the locking efficiency (and polarization) of the beam. However, none of these reduces the scatter below that shown in the plot.

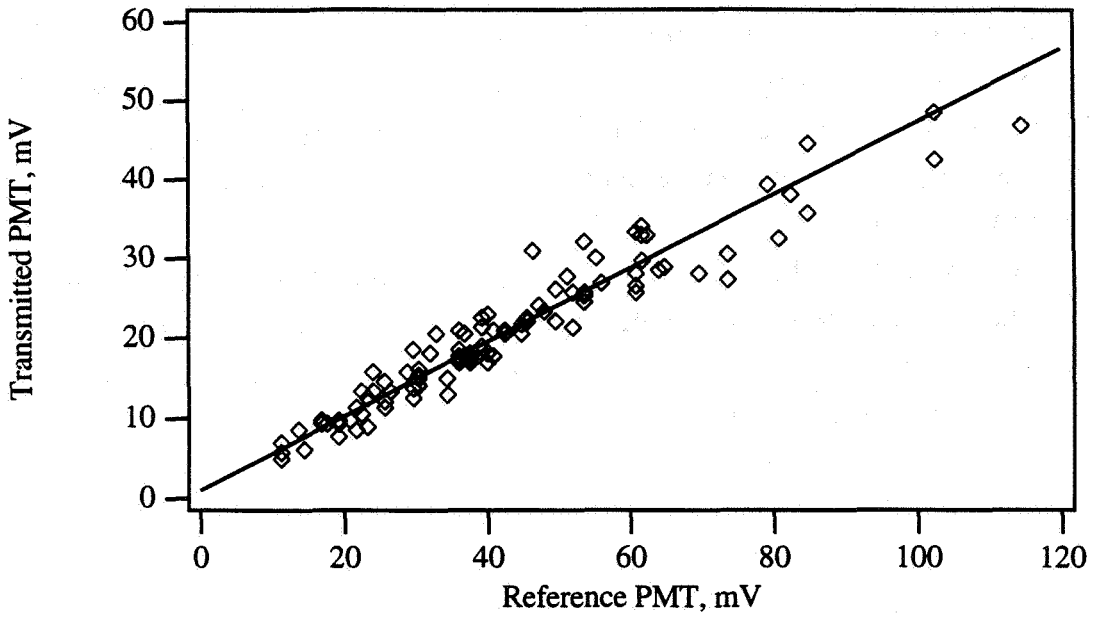

Figure 4.8 Typical calibration of reference signal levels for 100% transmission.

Non-ideal effects in the KBr photomultiplier tubes are one possible explanation for the scatter in calibration measurements. First, although the VUV conversion efficiency is small, it is sufficiently high that the tubes are operated at low gains and far from their design points. The relatively high current pulses drawn from the first several dynodes may lead to changes in the voltage divider distribution and in the secondary emission characteristics of the tubes. Second, the required operating voltage for the two tubes used in this experiment are significantly higher than that specified as "typical" for this type by the manufacturer. This may be indicative of problems with the secondary emission surfaces and could produce statistical variations in the apparent gain of the tubes.

This hypothesis has been tested by using the ArF pump beam with mixed results. In the first test, the incident laser beam is scattered by diffusers placed in front of the prisms to produce scattered light in the beam path. Correlation between the two photomultiplier tubes is no better than with the VUV beam. This test is not conclusive because there may be spatial inhomogeneities in the scattered light, but beam steering in the Raman cell is not a factor in these measurements. In the second test, the two tubes are compared directly by removing them from the system and illuminating them simultaneously. Single-pass ASE from the laser is attenuated and scattered from a Suprasil (quartz) diffuser. The two tubes are placed side-by-side, 4.5 m from the laser. Fluctuations in beam energy are detected by both tubes, and agreement between the two is limited only by digitization errors at 1%. This second test evaluates the performance of the

tubes alone at the voltage conditions of the experiments, but does not account for possible wavelength dependence of the photocathode and shorter pulse durations. The tubes alone appear suitable for accurate calibration, and the first test suggests a closer examination of the beam path.

Careful beam alignment and the aperture at the reference tube may not be sufficient to correct for variations in beam profile or beam pointing. The reference tube aperture is directly in front of the reference tube, but the transmitted tube is separated from the shock tube window apertures by glass tubing and the flow cell. Hot spots in the pump beam, angular variations in the anti-Stokes beam, or beam steering due to temperature gradients and local heating in the Raman cell may cause differences between the beams viewed by the two detectors.

Further attempts to eliminate the scatter should begin with an examination of the beam profile. Visualization of the beam allows optimization of alignment and aperture placement. Preliminary observations using sodium salicylate as the fluorescing medium and a single dispersing prism were successful only for lower order anti-Stokes lines; the 6th anti-Stokes at 130 nm was obscured by stray light at 193 nm. Although a second prism may be used to eliminate scattered light, it reduces the flexibility of the setup. An alternative approach using a fluorescing medium which is less sensitive at 193 nm might be more productive.

4.2 Shock tube flow validation

4.2.1 Flow requirements

Test conditions in the shock tube are selected to provide a sample of oxygen atoms for the absorption measurements. Initially, the shock tube is filled with molecular oxygen, so that the gas behind the shock can contain molecular and atomic oxygen, free electrons, and ions.

The test gas must meet several conditions for effective line shape measurements. Most importantly, the number density of atomic oxygen must be known to deduce the line shape function from absorption measurements. Additionally, the gas must contain a minimal number of other species, especially molecular oxygen and free electrons, for the experiment to be effective. Molecular oxygen absorbs at the same wavelengths as atomic oxygen, and substantial ionization causes Stark broadening to dominate the line shape. Thus, the presence of either O_2 or charged particles complicates interpretation of the data.

Equilibrium temperature and species compositions as a function of incident shock speed are shown in Figs. 4.9a and b with the EQGAS code (described in Section 4.2.2.2). The target shock speed selected was 6.8 km/sec because, as the figure shows, it provides nearly complete dissociation and only a small concentration of electrons.

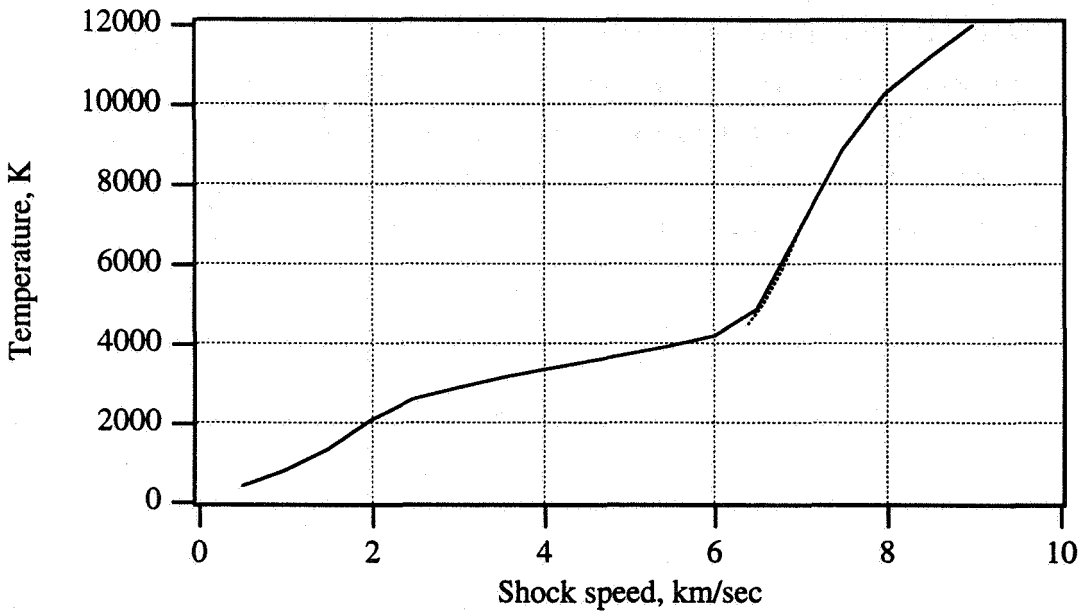

Figure 4.9a Equilibrium temperature behind a normal shock into 1.0 torr oxygen.

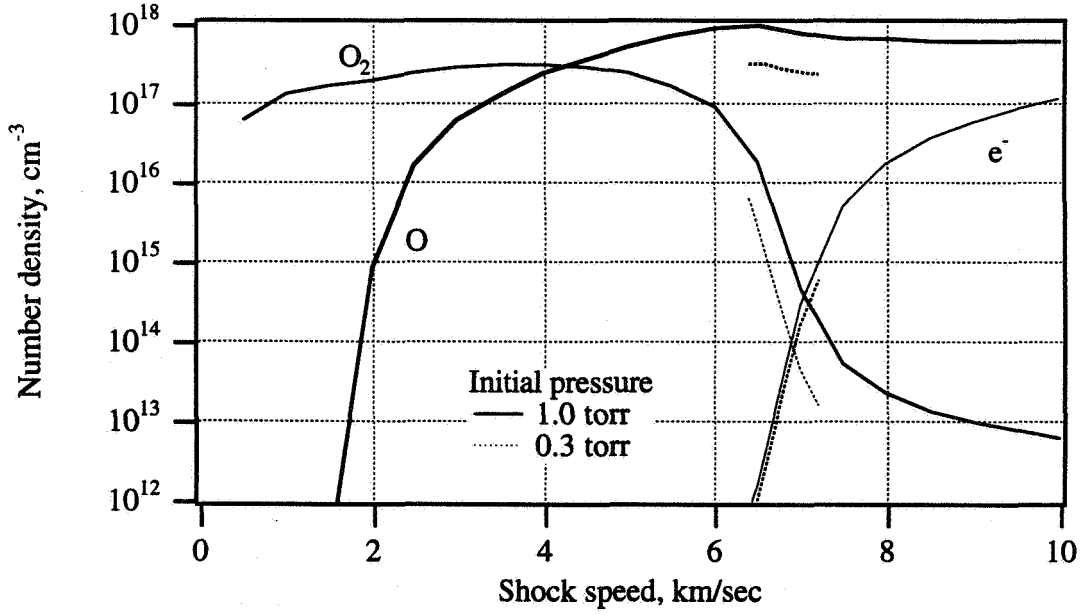

Figure 4.9b Equilibrium composition behind a normal shock into 1.0 and 0.3 torr oxygen.

Calculations for initial pressures of 1.0 and 0.3 torr are qualitatively very similar. For a given shock speed, the equilibrium temperature is identical to within about 200 K. The difference in pressure produces a slight change in composition. Lower pressure encourages dissociation and ionization, so that at the low density condition, O_2 density is reduced by a factor of ten and electron density is only reduced by a factor of two.

4.2.2 Flow characterization

Flow requirements are the same for both the high and low density measurements; however, characterization of the flow is performed slightly differently in the two cases.

4.2.2.1 Case A: High density (1.0 torr driven tube pressure)

In the first series of measurements, atomic density is deduced from shock speed measurements, and the effects of other species are inferred from emission measurements. Computations show that atomic density is a weak function of shock speed at 6.8 km/sec, so that uncertainty in atomic density is small. However, background absorption cannot be measured directly because atomic absorption is very strong. The triplet lines begin to merge together so that baseline measurements cannot be made between them. Therefore, concentration of O_2 and charged species are taken from equilibrium calculations, and radiation measurements are performed to verify this assumption.

Shock speed and shock attenuation are deduced from time-of-arrival measurements made with ionization probes and pressure transducers. The state of the gas passing the test section is a function of time, according to the shock speed at which it was shocked and any subsequent processes. The measured shock attenuation, dU_s/dL, is 600 sec^{-1}, corresponding to a gradient of equilibrium temperature, dT/dL, of 1700 K/m. The gradient of atomic oxygen number density is 7×10^{16} cm^{-3}/m.

Measured shock speed is corrected for attenuation with the following approximate model. Laboratory time is converted into particle time to determine the upstream location where the gas was shocked, and the shock speed, at that location, is determined from the measured shock attenuation, dU_s/dL,

$$\Delta U_s = \eta t_{lab} U_s \left(1 - \frac{1}{\eta}\right) \frac{dU_s}{dL} \tag{4.1}$$

$$U_{effective} \equiv U_{measured} + \Delta U_s \tag{4.2}$$

Shock speed, U_s, and attenuation, dU_s/dL, are measured, and the density ratio across the shock, ($\eta = \rho_2/\rho_1$), is calculated from the Rankine-Hugoniot relations. Temperature, pressure, and composition of the test gas are then computed for the effective shock speed, as shown in Figs. 4.9a and b.

Time-resolved emission measurements monitor the flow behind the shock wave. A typical trace from a photomultiplier sensitive over 125-165 nm is shown in Fig. 4.10. This spectral region contains emission from the O_2 Schumann-Runge bands and the atomic O triplet which is the subject of this study. Time resolution of the trace is limited to about 1 μsec by the window width. The initial spike is due to the nonequilibrium overshoot (Whiting and Park, 1990), which occurs during the dissociation process, and is followed by a quasi-steady state region before the arrival of the driver gas. The gradual increase in the intensity after the nonequilibrium spike is due to the gradual increase in the effective shock speed as given in Eqn. 4.2. The increase in intensity is indicative of only moderate changes in temperature because the excited state populations (and the emission intensity) depend strongly on temperature.

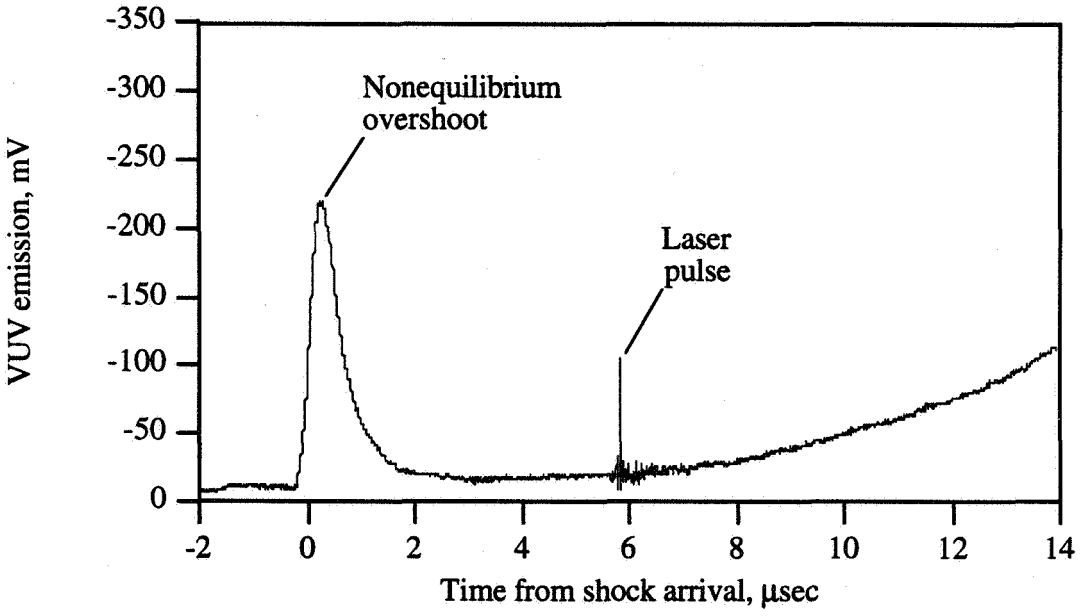

Figure 4.10 Measured VUV emission behind shock into 1.0 torr oxygen.

The reacting flow behind the incident shock is calculated with NONEQ (Whiting and Park, 1990) using chemical reaction rates derived for a two-temperature model. The model equates the rotational temperature to the translational temperature, and the free electron kinetic and electronic temperatures to the vibrational temperature. Vibrational

relaxation is treated with the modified Landau-Teller model, which limits the relaxation rate to the gas-kinetic collision rate at high temperatures.

Calculations of the reaction zone length are compared to radiometer measurements. Calculated gas temperature and gas composition both reach their equilibrium values in less than 2 μsec of laboratory time after the shock passes. This is consistent with the width of the intensity peak detected behind the shock wave, as shown in Fig. 4.10.

The condition of the test gas, after steady state is established, is checked with intensity-calibrated emission spectra. A typical spectrum is shown in Fig. 4.11. The less intense portions of the spectrum are also shown on an expanded scale (with the intensity multiplied by a factor of 10) to illustrate some of the low intensity values. The spectra are all qualitatively similar and consist primarily of atomic oxygen emission lines with a weak background. The 777 and 845 nm triplets are most intense, but other lines are detected, such as the multiplet at 616 nm.

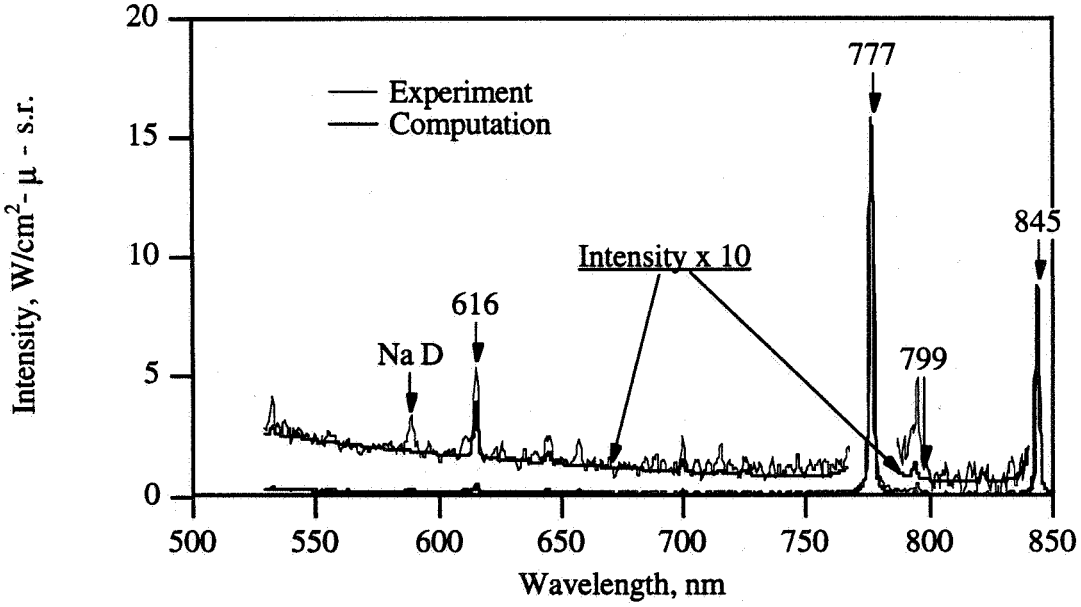

Figure 4.11 Comparison of measured and calculated emission spectra behind shock.

Atomic emission spectra are synthesized with the NEQAIR5 code (Park, 1985, and Sharma and Whiting, 1994). Individual atomic lines are calculated at sufficient resolution to account for self-absorption. The lineshape function includes contributions from

Doppler, lifetime, and collisional broadening. The collisional broadening model includes collisions with like atoms,* other heavy particles, and free electrons.

Excited state populations are calculated by using both the Quasi-Steady State (QSS) formulation and Boltzmann distributions. The QSS formulation provides a general approach for determining excited state populations from the relative rates for populating and depopulating each state. Collisional rates depend on the gas composition and collision frequency, but radiative decay rates do not. In the limit of high collisional frequency, excited state populations are determined from collisional rates, commonly producing a Boltzmann distribution. Calculations with Boltzmann distributions are preferable because they are easier to perform numerically, and, more importantly, because they do not require accurate knowledge of state-to-state collisional rates. The QSS formulation has the correct limiting behavior, *i.e.*, it predicts a Boltzmann distribution for high collisional frequency. Thus, QSS calculations provide verification that assumption of a Boltzmann distribution is warranted.

Boltzmann and QSS calculations are virtually identical for all lines except the 777 and 845 nm triplets. Using the QSS approximation, the 777 nm triplet is less intense by a factor of 4 to 7 than when using the Boltzmann calculation, and the 845 nm triplet less intense within a factor of 2. The difference is likely due to limitations in the present QSS calculation which only includes excitation by electrons. In the present test conditions, the number of electrons is on the order of 10^{14} cm^{-3} (see Table 4.1). Although collisions with heavy particles are less efficient than those with electrons, the number of heavy particles is several orders of magnitude higher than that for electrons. The QSS calculation, therefore, represents a lower bound to the line intensities. The calculation assuming a Boltzmann distribution is in better agreement with the measurements, and is shown in Fig. 4.11.

Intensity calculations for lines in the near infra-red are modified in two ways from that given in NEQAIR5. The three components of the 845 nm triplet are calculated individually, and some of the transition probabilities tabulated by the NBS (Wiese, *et al*, 1966) are replaced with recently calculated values (Hibbert, *et al*, 1991). Differences are small with the exception of the multiplet centered at 799 nm. The older transition probabilities for this multiplet were calculated from approximate hydrogen-like wavefunctions, and are about three orders of magnitude larger. Line intensity calculations with these theoretical A values predict that this multiplet should be observed.

---

* Resonance broadening is not included in NEQAIR5 for emission lines not terminating in the ground state although it is a potential broadening mechanism for certain lines. See discussion in Chapter 5.

Experimentally, however, this multiplet is not observed, indirectly supporting the more recently calculated values.

Temperature of the test gas is determined by changing the temperature until the calculated line intensities are in agreement with the measured values. This temperature corresponds to the conditions behind a shock wave of a given speed, as shown in Fig. 4.9. Thus, the shock speed is deduced from the temperature fit to the measured spectra, with a typical uncertainty of 0.05 km/sec.

Shock speeds deduced from spectra and derived from shock attenuation measurements are plotted as a function of time after shock arrival in Fig. 4.12. The effective shock speed is normalized by the incident shock speed. Horizontal bars on the data represent the gate width of the diode array, *i.e.*, the exposure time of the array. Agreement between these measurements verifies that test gas conditions agree well with those predicted by shock speed measurements. VUV absorption measurements are made 6.4 μsec after shock passage when the test gas is well characterized.

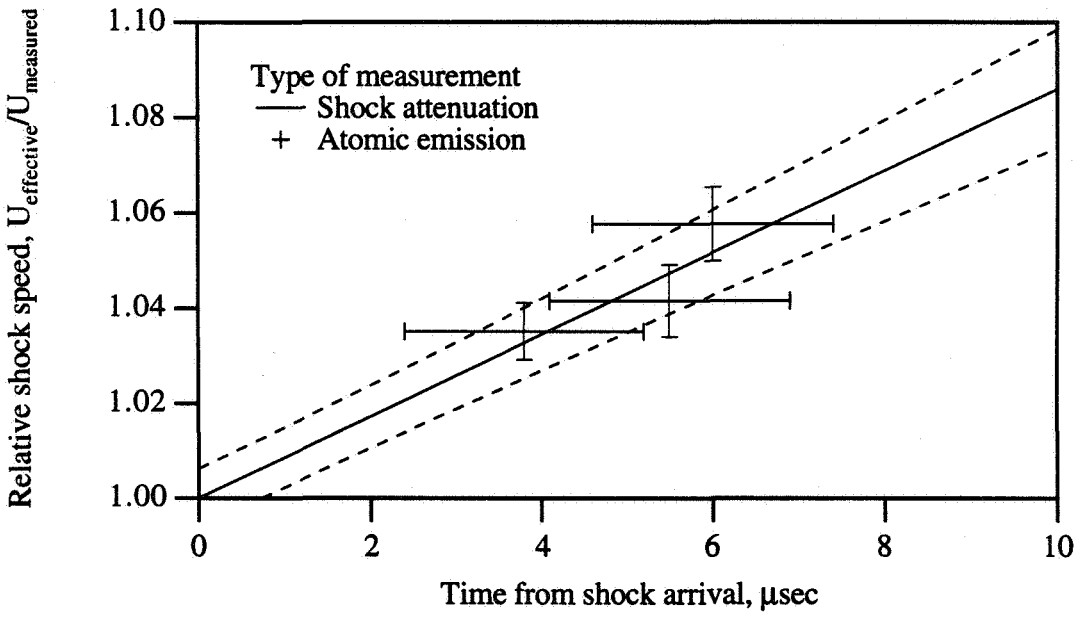

Figure 4.12 Effective shock speed deduced from emission spectra and shock speed measurements.

At this test condition, absorption data were collected on 11 shock tube runs, with a mean effective shock speed of 6.83 km/sec and a standard deviation of 0.16 km/sec. Equilibrium conditions behind the shock wave are calculated with the EQGAS code, which solves the one-dimensional shock wave equations for a real gas. Routines for calculating thermodynamic properties are extracted from the work of Liu *et al* (1990). Partition

functions of the atomic and molecular components are computed from tabulated values of spectroscopic constants. For diatomic molecules, the number of bound rotational and vibrational states are determined, and partition functions are calculated accordingly. The partition function for atomic oxygen includes 3055 energy levels for configurations $2p^3nl$, for n up to 10. Equilibrium compositions are found from thermodynamic properties derived from the partition functions. Interactions between particles are not included, and should be small for the moderate density and low ionization in the present test. Results of the computations are shown in Table 4.1 for the nominal shock speed, and for shock speeds one standard deviation higher and lower than nominal.

Table 4.1 Shock tube test conditions for Case A (1.0 torr initial pressure)

Shock speed, km/sec	6.83-0.16	6.83	6.83+0.16
Temperature, K	5400	6100	6800
O density, cm^{-3}	$9.6x10^{17}$	$9.0x10^{17}$	$8.4x10^{17}$
O_2 density, cm^{-3}	$6x10^{15}$	$2x10^{15}$	$5x10^{14}$
e^- density, cm^{-3}	$2x10^{13}$	$7x10^{13}$	$3x10^{14}$

4.2.2.2 Case B: Low density (0.3 torr driven tube pressure)

At this test condition reaction rates are slower, but more direct measurements are available to characterize the test gas. Atomic density is again deduced from shock speed measurements. The number density is lower, so background absorption can be measured directly in the region between the atomic lines. Flow characterization is therefore more empirical; calculations are used only to deduce atomic density and to infer an upper limit on Stark broadening.

Absorption measurements are performed at the same delay time behind the incident shock. Time-resolved ultraviolet emission recorded with a CsTe photomultiplier shows that the nonequilibrium overshoot ends well before the laser pulse (Fig. 4.13a). At this test condition virtually all of the O_2 dissociates, so that small deviations from equilibrium will not affect the atomic number density. The atomic density can thus be deduced from shock speed measurements. As before, shock speed is corrected to account for attenuation.

Background absorption is measured at several delay times to determine the optimum time to measure the line profile, and the results are shown in Fig. 4.13b. Background absorption, presumably due to O_2, decreases quickly behind the shock. Internal delays in the laser head and the finite width of the port plug windows prevent measurements directly

behind the shock; however, the earliest possible measurement shows that the absorption disappears quickly. Excessive corrections for background absorption are not required.

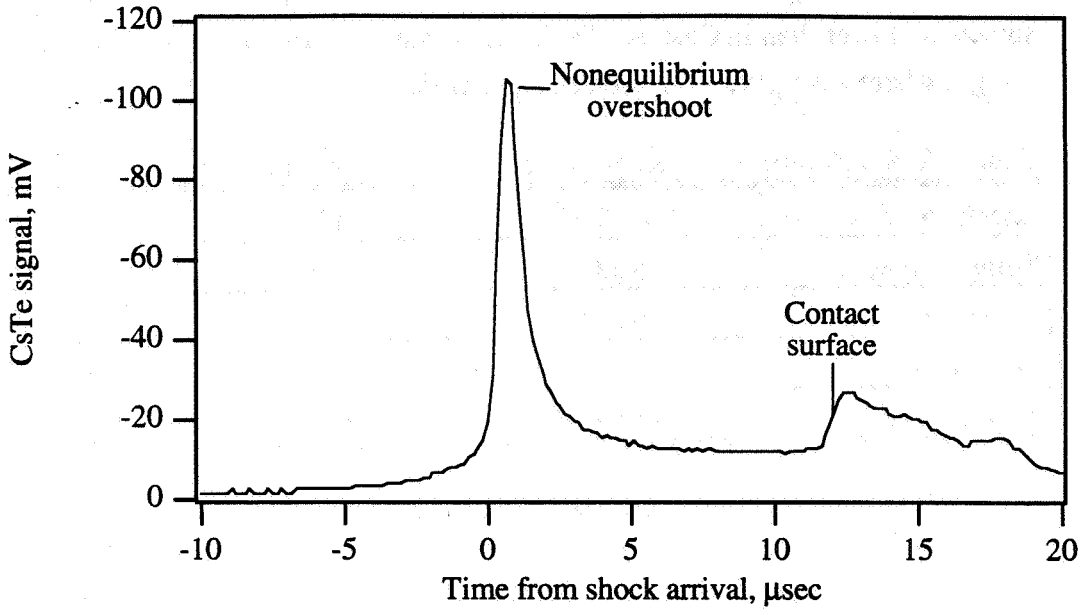

Figure 4.13a Measured UV emission behind shock into 0.3 torr oxygen.

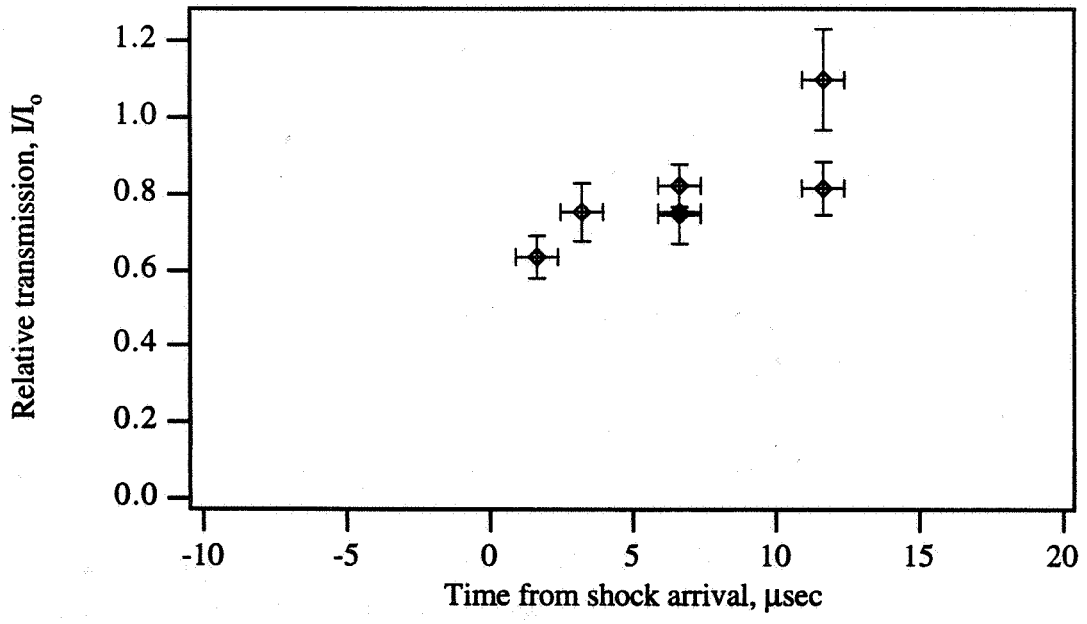

Figure 4.13b Background transmission at 130 nm at various delay times after shock arrival.

The test condition is chosen so that ionization is too low to cause substantial Stark broadening. The calculated Stark width for electron collisions is smaller than that for natural broadening. Standard deviations in the shock speed are 0.10 km/sec, a value somewhat lower than in Case A. Table 4.2 summarizes thermodynamic conditions of the test gas where absorption measurements are made.

Table 4.2 Shock tube test conditions for Case B (0.3 torr initial pressure)

Shock speed, km/sec	6.74-0.10	6.74	6.74+0.10
Temperature, K	5200	5600	6100
O density, cm^{-3}	$3.0x10^{17}$	$2.9x10^{17}$	$2.7x10^{17}$
O_2 density, cm^{-3}	$9x10^{14}$	$3x10^{14}$	$1.5x10^{14}$
e^- density, cm^{-3}	$4x10^{12}$	$1x10^{13}$	$4x10^{13}$

4.3 VUV absorption measurements

4.3.1 Photomultiplier traces

As described previously, the absorption measurement consists of measuring the incident and transmitted intensities of the probe beam. Individual traces for both channels are digitized, and typical traces are shown in Fig. 4.14. Width of the pulses depends on the voltage applied to the dynode chain, but a typical width is about 25 nsec. This relatively large width is due to transit time broadening of the tubes and to the 20 MHz filter at the digital oscilloscope. Filtering the traces reduces the noise without affecting the accuracy of the ratio of the incident and transmitted intensities. Dual pulses were observed in early measurements, but were not observed after diffusers were placed in front of the photocathodes. When two pulses appear, the first is more narrow than the second, and the delay between them depends on the tube voltage. The most probable explanation is that the first pulse is a "pre-pulse" caused by photons passing through the photocathode and generating photoelectrons at the first dynode. Measurements of the delay time and its variation with voltage are consistent with calculated values of the drift time of photoelectrons between the cathode and the first dynode. Additionally, only the second pulse is correlated with the beam intensity as measured by the other tube. Expanding the incident beam with a diffuser eliminates this effect because the active photocathode area is much larger than the collection area of the first dynode.

Traces are digitized with 8-bit analog-to-digital converters, providing a dynamic range of ±128 steps. Offsets are introduced to shift the zero level of the signals so that the

negative-going traces take advantage of the full dynamic range. With the Tektronix 2440 scope, however, full dynamic range is not available at high sampling rates. Although the amplifiers are sufficiently fast and linear, the A/D is operating at its upper limit. At 500 Msample/sec, the dynamic range is reduced to 226 steps. Signals that exceed this level are distorted, but are not clipped like those that exceed 256 steps. These distortions cause a nonlinearity in the response of the oscilloscope, and are avoided in the absorption measurements.

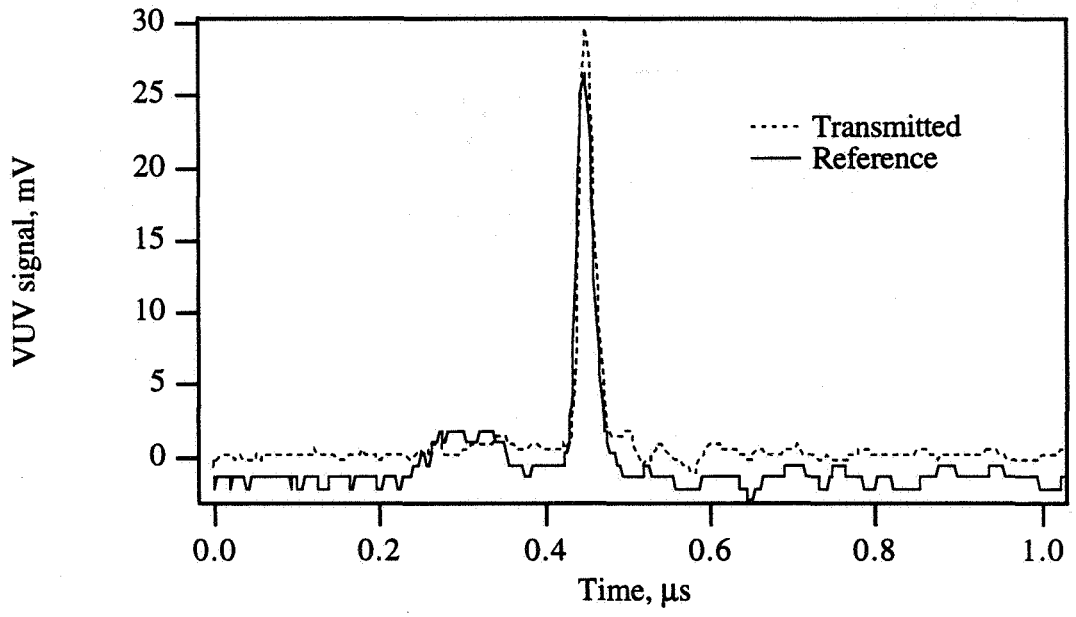

Figure 4.14 Typical traces from the reference and transmitted photomultipliers tubes.

Transmission measurements with a CaF_2 window verify that the photomultiplier tube operates in a linear operating range. A filter wheel for McPherson spectrometers is placed before the photomultiplier tube, and the transmission of a CaF_2 window is measured. Separate measurements with a discharge lamp and spectrometer show that the CaF_2 transmits 50% at 130.49 nm, in agreement with measurements made with the KBr photomultiplier tube. Thus, tube response is linear to within the scatter of the calibration measurements.

4.3.2 Absorption profiles

The theoretical and empirical absorption profiles for Case A (high density) are shown in Fig. 4.15. The theoretical profile is reproduced from Fig. 2.3, and details of the calculations are given in Section 2.6.3. Briefly, absorption profiles are calculated for each line with Beer's Law, Eqn. 2.36, and the line shape functions are calculated from

theoretical linewidths. Doppler, lifetime, and Stark linewidths are calculated from Eqns. 2.6, 2.4, and 2.37, respectively. The resonance width is calculated with the impact model, using Eqn. 2.28. Data analysis presented in the next chapter uses the same equations with the exception that the Lorentzian linewidth is a free parameter in the curve fits. As demonstrated in Chapter 2, resonance broadening is responsible for most of the Lorentzian width. Therefore, the empirical linewidth for resonance broadening is found from the empirical Lorentzian width by subtracting corrections for the other broadening mechanisms.

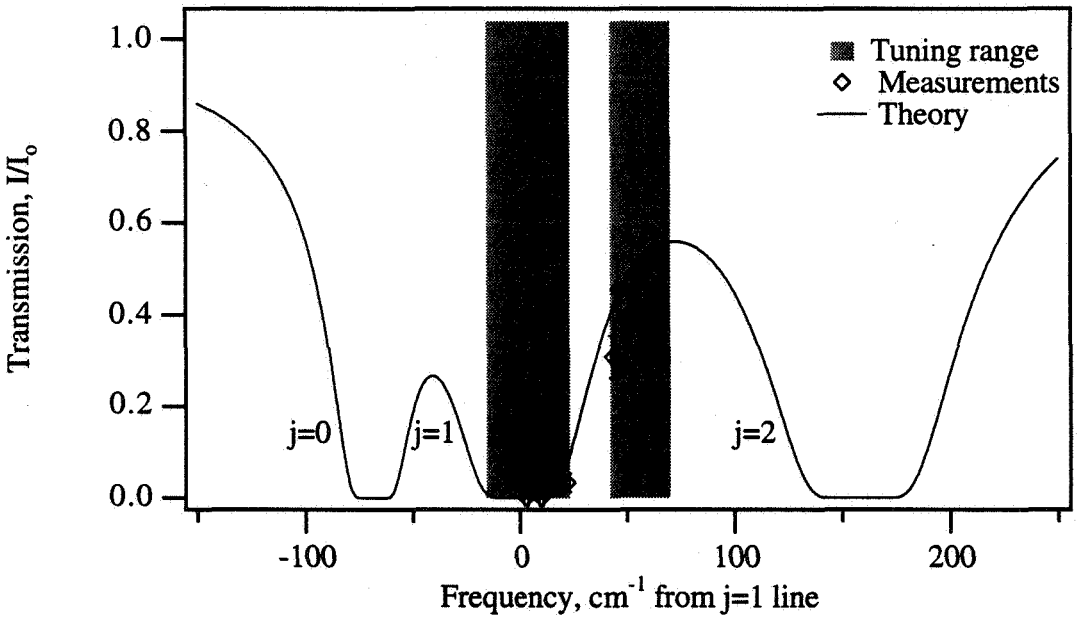

Figure 4.15 Measured transmission in the region of the j=1 transition (130.49 nm) for Case A (high density).

In Case A, the three lines overlap in the line wings and the peak measured transmission is less than 50%. Measurements in the two tuning bands indicated in the figure probe the absorption profile around the j=1 transition at 130.49 nm. Vertical error bars are produced by uncertainty in the reference intensity, and the horizontal error bars by the linewidth of the probe laser and by uncertainties in the line position. Absorption by the j=1 transition is clearly shown by the data. However, the background absorption level cannot be measured between the lines, so it is difficult to deduce an accurate linewidth from the data. The gap in the tuning band prevents measurements in the spectral region where the absorption profile varies most rapidly. Two experimental improvements would reduce uncertainty in the background absorption. First, thoroughly purging the beam paths of oxygen reduces width of the tuning gap, allowing measurements in part of that region.

Second, transmission below 10% can be measured more accurately by calibrating with an absorbing filter, such as a thick CaF_2 or MgF_2 window. A higher PMT voltage, and thus higher signals, can be used if the calibrations are performed for 10% transmission instead of 100% transmission.

Theoretical and empirical profiles for Case B are shown in Fig. 4.16. To evaluate the effect of number density on linewidth, measurements for Case B are at a lower density. From the results of Case A, the second test condition is chosen so that the lines are narrower and the overlap is reduced substantially. Although the lines are narrower, relative contributions from the various broadening mechanisms are similar, so these measurements are still dominated by resonance broadening. Background transmission is measured between the lines. At this condition, the atomic lineshape is contained in the available tuning bands and is not expected to vary substantially in the tuning gap. As a result of the narrower line, measurements are made on both sides of the line center. No asymmetry is observed within the uncertainty of the measurement.

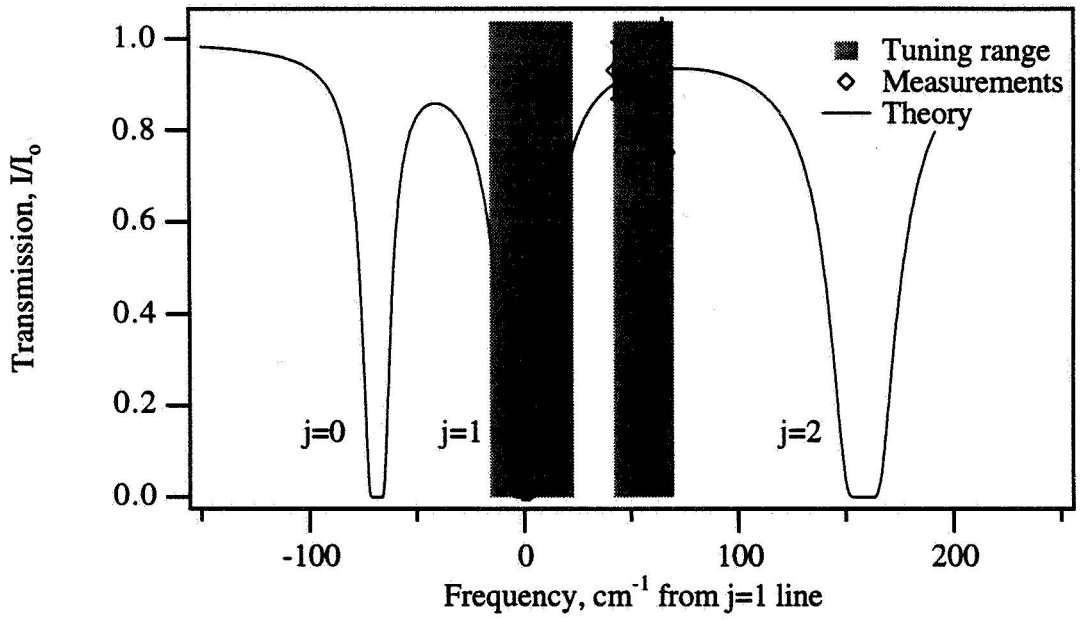

Figure 4.16 Measured transmission in the region of the j=1 transition (130.49 nm) for Case B (low density).

In Case B, Raman shifter performance was better, presumably due to cleaning and/or replacement of most optics, and LIF measurements in the flow cell demonstrated tuning out to j=0 (130.60 nm). Exploratory shock tube measurements in this region were unusable, however, because of excessive scatter in the calibrations. Error bars for the x-axis are smaller for Case B because wavelength calibration is performed with the

microwave flow cell. Error bars for the y-axis are similar for both cases, indicating that scatter in calibration measurements is not appreciably reduced by the experimental modifications described previously.

In both cases, the theoretical curves agree reasonably well with the measurements. Uncertainty in the line strengths is ±10%, and the experiments are designed so that both number density and path length are known. Therefore, the largest uncertainty in the calculated profiles lies in the approximate theories used to calculate the broadening widths. The figures demonstrate that the results of the resonance broadening model are in accord with the empirical measurements, although this agreement may be fortuitous given the approximate nature of the resonance model used here. In the next chapter, empirical linewidths and an empirical broadening coefficient are deduced, and interpretation of the empirical and theoretical results are discussed.

Chapter 5
Results and Discussion

Absorption line profiles have been measured at two atomic densities. In this chapter, the measurements are analyzed to deduce the resonance linewidth. Empirical values are compared to theoretical models presented in Chapter 2, and also to resonance broadening measurements for other atoms. This chapter concludes with a discussion of applications of VUV absorption as a concentration diagnostic.

5.1 Experimental results

5.1.1 Linewidth measurement

Applying the impact approximation to collision broadening produces a Lorentzian line shape, which is convolved with other mechanisms to produce a Voigt profile. The empirical data is analyzed by fitting to Voigt functions for the following reasons:

1) Various broadening mechanisms are accounted for and are easily separable.
2) Quasi-static model shows same frequency dependence as impact model.
3) Data is not sufficient to detect deviations from Lorentzian (quadratic) behavior.
4) Alternative line shapes based on higher order approximations are not available for direct comparison.

Analysis of data for Case A (high density) includes corrections for broadband absorption due to O_2, as well as contributions from the adjacent lines at 130.22 and 130.60 nm. In the high density case, background absorption due to residual O_2 in the test gas and in the boundary layers is estimated as 10±10%. Curve fits to the data are plotted in Fig.

5.1 for background absorptions of 0 and 20%. Contributions from the line at 130.22 nm are substantial at this test condition. Based on the theoretical models discussed in Chapter 2, broadening coefficients for all three lines are assumed equal. A Lorentzian width of 0.057 cm^{-1} is deduced for this test condition. As demonstrated in Chapter 2, self-broadening is the dominant component at this condition. Corrections of 0.0034 cm^{-1} and 0.0010 cm^{-1} for lifetime and Stark broadening, respectively, yield a self-broadening width of 0.052 cm^{-1}, FWHM.

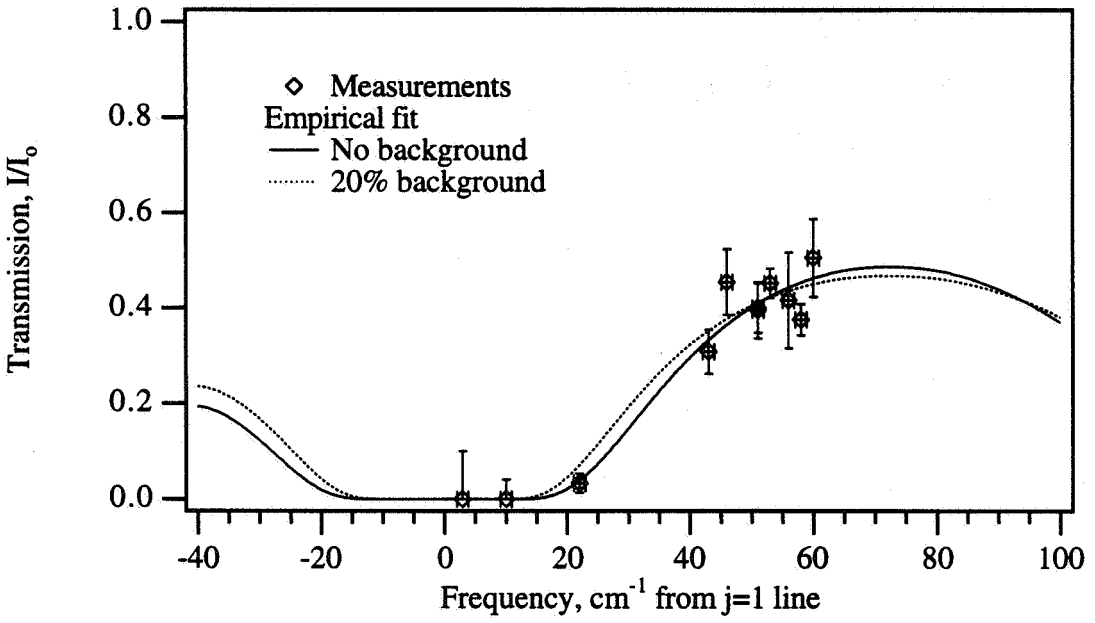

Figure 5.1 Lorentzian fit to absorption data for Case A (high density).

Baseline for Case B (low density) is included as a parameter in the curve fitting, and corrections for adjacent lines, while still included, are much smaller. Least squares curve fits are carried out with the Lorentzian width and background absorption as free parameters. Curve fits are performed first on the transmission data, and then on the logarithm of transmission (optical depth). The two fits provide different relative weightings to the data points, with the first placing more emphasis on the highest transmission points. The second fit places more emphasis on the points where absorption is strongest, and is more appropriate where uncertainty is proportional to the measured transmission at each point. The resulting linewidths differ by only 6%; the average value is 0.0160 cm^{-1} with a background absorption of 8%, and is shown in Fig. 5.2. After subtracting corrections of 0.0034 cm^{-1} and 0.0002 cm^{-1} for lifetime and Stark broadening, a self-broadening width of 0.0124 cm^{-1}, FWHM, is obtained for this condition.

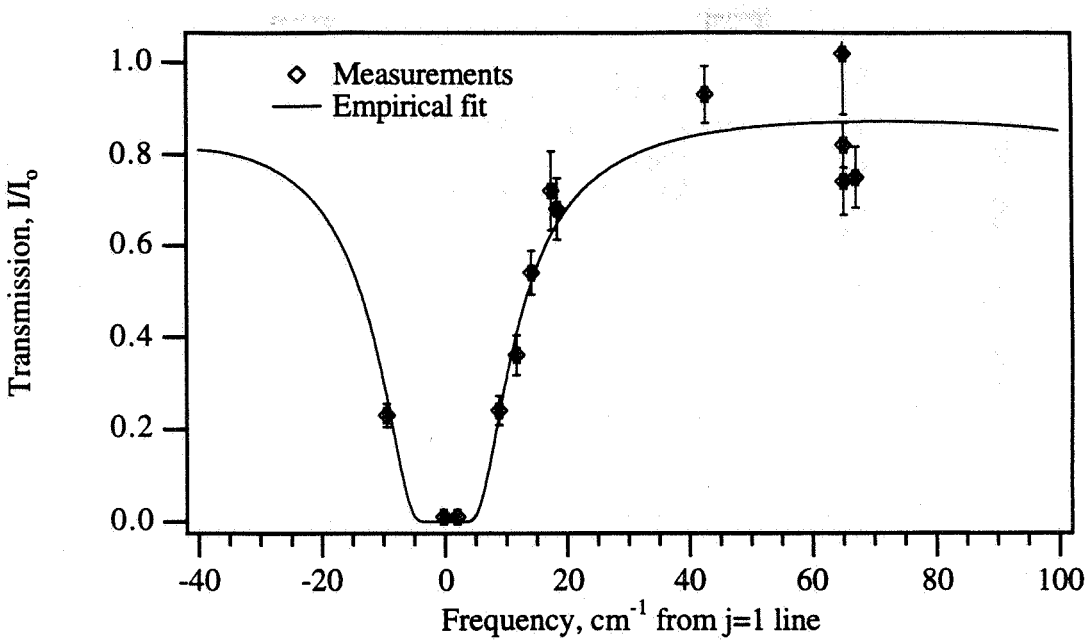

Figure 5.2 Lorentzian fit to absorption data for Case B (low density).

The measured linewidths are compared to theoretical models in Fig. 5.3. The measured linewidths and the impact model agree very well. The quasi-static model is calculated with results for hydrogen, and so is only approximate. Discrepancies between theory and measurements are within the estimated experimental error. A resonance broadening coefficient can be deduced from the data, assuming a linear dependence on atomic oxygen number density. The empirical linewidth (Lorentzian FWHM) is

$$_{Expt.}\overline{\nu}_{Resonance} = \left[4.9x10^{-20} cm^{-1} cm^{3}\right] n_L \tag{5.1}$$

where n_L is the number density of atoms in the ^{3}P state. The broadening coefficient predicted with the impact model in Chapter 2 agrees well with this value.

5.1.2 Experimental error sources

Imperfections in transmission measurements and uncertainties in data analysis lead to errors in the empirical linewidths. The important measurement uncertainties are discussed in the previous chapter, such as uncertainty in reference intensity, probe beam wavelength and linewidth, and spectral purity of the probe. These produce the vertical and horizontal error bars on the transmission data. Uncertainties in the data analysis include broadband absorption, other broadening mechanisms, and atomic number density.

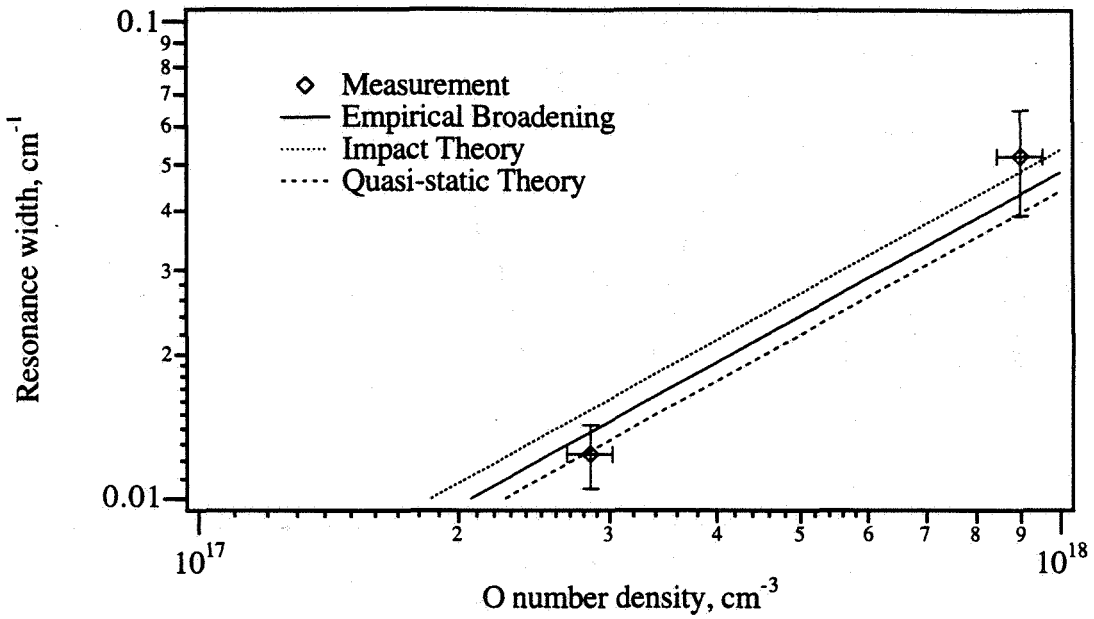

Figure 5.3 Comparison of linewidths predicted by impact and quasi-static theory to measured values.

Uncertainty in the reference intensity is the largest uncertainty in the transmission measurements. Despite experimental modifications described previously, this error source was not eliminated. The magnitude of the error is determined by evaluating the scatter in calibration measurements performed before each shot. Statistical analysis of 100 shots taken before each shot yield standard deviations of 7-13%. Although the average value of the calibration factor between reference and transmitted tubes is known accurately, a single shot transmission measurement is limited by the magnitude of this scatter. This statistical error is the source of the vertical error bars in the transmission measurements.

Wavelength calibration and beam linewidth are the sources of the horizontal error bars, which are not a significant error source in the experiment. Beam linewidth and wavelength calibration are measured with the microwave flow cell, and spectral transmission varies linearly over the range of 1 cm^{-1}, which typifies the resolution obtained in this experiment. At lower densities or shorter absorption paths than those encountered here, however, a deconvolution of probe beam and absorbing linewidths is required.

Spectral purity of the probe beam requires narrowband light at the desired wavelength and rejection of other Raman orders and stray light. Spectral measurements with a scanning monochrometer demonstrated that stray light is eliminated, but the sixth anti-Stokes Q-branch at 130 nm consisted of both narrowband and broadband

components. The ArF locking efficiency is measured during all shots at the lower density, so that corrections can be applied for this background.

During absorption measurements, however, the probe beam is completely attenuated when tuned to the center of the line. Based on locking efficiency measurements, the broadband component could produce an apparent transmission of roughly 10%. This is not observed, however, indicating that no broadband or stray light contaminates the measurements. The discrepancy between the preliminary spectral measurements and the absorption measurements might be explained by

1) substantial differences in the beam profile or divergence of broadband and narrowband components
2) dependence on the hydrogen pressure in the Raman cell
3) experimental errors in the scanning measurements, *i.e.* dynamic range limitations of the digital oscilloscope

Of these, the second and third explanations seem most probable. During the absorption measurements, conversion efficiency was initially so high that the resulting 130 nm light saturated the photomultipliers. Conversion efficiency, and thus intensity, was reduced by lowering the hydrogen pressure in the cell by 25%. If conversion efficiency is higher for narrowband than for broadband, the resulting decrease in hydrogen density would favor conversion of the narrowband component. Loree, *et al* (1979) cite studies of Raman shifting with broadband lasers which appear to contradict this hypothesis, concluding that the cross-section for forward Raman scattering is independent of the laser linewidth. In preliminary investigations with a room-temperature cell pumped by a KrF laser (248 nm), however, preferential conversion of the narrowband was observed. Other parameters, such as the temporal profile of narrowband and broadband components, may play a role, but a satisfactory explanation is lacking. Certainly, distortion of the signal by the digital scope during monochrometer scans of the narrowband peak produces an overestimate of the relative broadband background. Based on the results of absorption measurements at line center, the data is interpreted under the assumption that the probe beam is spectrally pure.

Several other potential measurement errors exist which are not expected to be significant. Broadband emission from the test gas is observed only in the high density case, where it appears as a slowly varying baseline beneath the VUV probe pulse. The probe pulse is time-resolved and background emission can be easily subtracted out. Atomic transitions can be saturated with an intense probe beam, but this is less likely when

collisional broadening, rather than Doppler broadening, is dominant. Strong saturation of the transitions would produce measurable transmission at line center, which is not observed. Beam steering by the test gas can potentially deviate the beam from the detector. Although the index of refraction is high near the transitions, gradients in atomic concentration should be relatively weak. The limiting aperture at the detector is wider than the shock tube window to minimize this effect, but no measurements are performed to quantify it.

The number of absorbers depends on the total number of atoms and on the *fraction* of atoms in the absorbing state, $2p^4\,{}^3P_1$. Uncertainties in atomic number density depend on both statistical and systematic errors. Atomic concentrations in the shock tube are reproducible to within ±9%, 2σ.* Two systematic error sources are expected. First, boundary layer effects reduce the effective pathlength, but estimated thicknesses are at most a few percent of the tube diameter and are not a significant error source. Second, atomic number density is deduced from corrected shock speed measurements. The correction results in a decrease in atomic density of about 10% from the value calculated behind the shock; the systematic error in the number density is expected to be significantly less than this correction. The *fraction* of atoms in $2p^4\,{}^3P_1$ depends on electronic temperature, and at 6000 K, the temperature dependence is extremely weak. A non-Boltzmann distribution, if present, primarily affects excited states which account for only a small fraction of all atoms; the $2p^4\,{}^3P_j$ population fraction should not be appreciably affected.

Deduction of the linewidth also depends on the total absorption cross-section or line strength. Numerous measurements of the transition probability for ${}^3P\text{-}{}^3S^\circ$ have been reported, and these values have converged to those listed in Chapter 2 (Jenkins, 1985). The transitions are strongly dipole-allowed, so reliable transition probabilities have been calculated which are in good agreement with experiment. Uncertainty in the absorption cross-section is therefore small, and is estimated at ±10%. This error source affects the measured broadening coefficient, but in practice does not affect calculations made with it. The cross-section is a physical constant, not an experimental parameter, so uncertainties in the cross section do not affect the *product* of the cross section and line shape function found in Beer's Law, as long as the two values used are internally consistent.

Background absorption by O_2 can be caused by undissociated oxygen in the core flow and recombined oxygen in the boundary layer. Direct measurements of the background are made in the low density case, and so the background can be accounted for

---

* Uncertainties denoted by "2σ" indicate that the range of possible values is assumed to lie within ±2 standard deviations of the nominal value.

directly. For the high density data, absorption is estimated subject to several uncertainties. The concentration of undissociated oxygen is determined from equilibrium composition calculations, and is a strong function of shock speed. High-temperature absorption cross-sections for O_2 are discussed in Appendix B. Data is sparse, especially at 130 nm. Absorption in the boundary layer is treated approximately, and is also discussed in Appendix B. The boundary layer correction can only be considered an estimate of the absorption expected. Some additional information might have been available from broadband absorption measurements at another wavelength, but uncertainties in absorption coefficients and boundary layer thicknesses still limit the usefulness of such data for estimating background absorption at 130 nm (see Appendix B).

The effect of baseline errors on the empirical width has been evaluated analytically and numerically. Taking partial derivatives in Beer's Law shows that the relative error depends on the transmission. At a typical transmission of 50%, a 2% change in baseline produces a 3% change in the apparent Lorentzian width. Numerical evaluation for Case A verifies this result, as shown in Fig. 5.4.

Competing broadening mechanisms must be separated out to deduce the resonance broadening linewidth. In the line wings, Doppler broadening is insignificant, so a Voigt profile can be treated as a Lorentzian. Corrections for other mechanisms are subtracted from the measured line width. Lifetime broadening is independent of thermodynamic properties and can be reliably subtracted out, assuming that the elementary theory is valid in the far line wings. Stark broadening effects are more difficult to calculate. Stark broadening due to electrons is calculated with the model in NEQAIR5 assuming equilibrium concentration of electrons. Stark broadening by ions is often modeled differently, but in this study it is treated approximately by setting it equal to the electron broadening for lack of a better model. An independent measurement of electron density generally improves the accuracy of Stark corrections. Although electron density was not measured directly, the current test conditions were chosen to minimize the effect of Stark broadening on the measured linewidth.

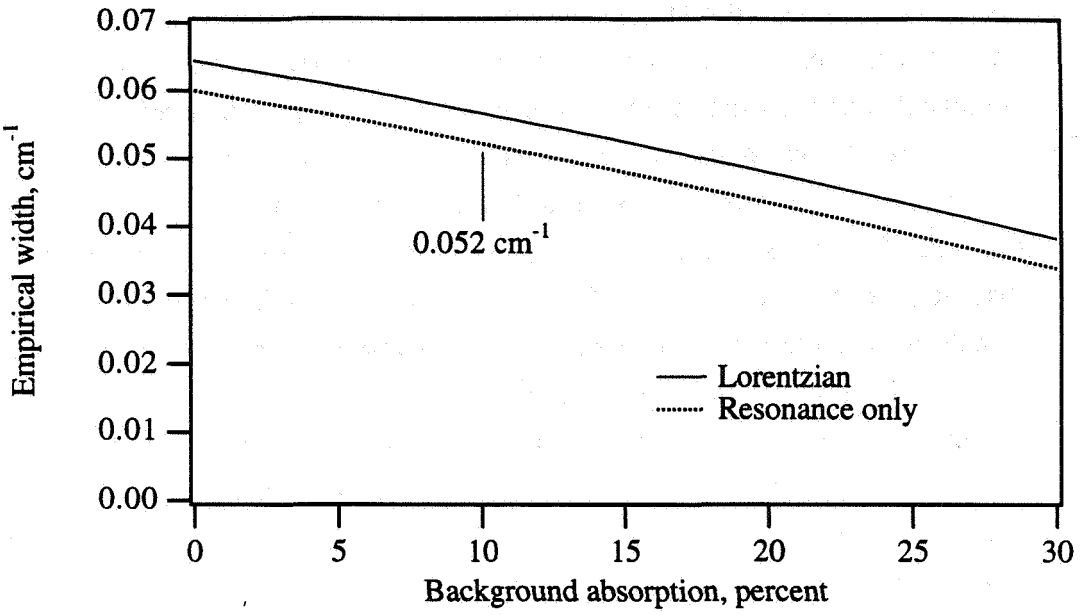

Figure 5.4 Effect of broadband background absorption on derived linewidth for Case A (high density).

Mapping out the line profile with a series of single-shot shock tube measurements produces most of the measurement uncertainty through the mechanisms described above. The effect of limited sample size and scatter is difficult to evaluate. However, it can be estimated by considering the statistical variation of the empirical linewidth with the number of measurements. The question, "How much would another data point reduce the uncertainty in linewidth?" can be answered approximately by taking away one of the data points and deducing the linewidth from the remaining points. Repeating this process for all data points produces an estimate of the scatter in the deduced linewidth. This analysis has been performed for the low density case, and the standard deviation in the deduced linewidths is 3.4%. Therefore, *non-systematic*, random errors produce an uncertainty of about 7% (2σ) in the measured linewidth. Systematic errors contribute as well, and the estimated uncertainty in the broadening coefficient is 20-30%, 2σ.

5.2 Discussion of results

Results of the line broadening measurements are evaluated in the context of other work on resonance broadening, followed by a discussion of possible refinements to the approximate models employed here.

5.2.1 Resonance broadening of other atoms

Resonance broadening has been studied extensively both experimentally and theoretically, although not with oxygen atoms. Previous research has focused on metallic vapors and noble gases because they are experimentally more convenient and theoretically simpler to model. Unlike oxygen, these species are readily obtained as free atoms, and transition wavelengths are in the visible or ultraviolet. Theoretical analysis is also more direct because the oxygen transitions are from a triplet lower state with more fine structure levels to consider. However, it is useful to discuss the present measurements in the context of previous work.

Hydrogen is a particularly simple system with only a single electron. King and Van Vleck (1939) evaluated the long-range resonance (or dipole-dipole) interaction between excited and ground state atoms. As the atoms approach each other, they become coupled and take on the character of molecular wavefunctions. Results for an S lower state and a P upper state are especially simple when spin is neglected, and the interaction for various m-values is easy to evaluate. Despite extensive study of this system, experimental verification faces the same obstacles as the current experiment of dissociating a molecular gas and probing a VUV transition. Kielkopf (1992) describes proposed experiments using a laser-produced plasma to study Lyman-α radiation, but only preliminary results are given.

Theoretical analyses of hydrogen have been applied to metallic vapors, which are more convenient to study experimentally. Atomic vapors are generated in ovens and the number densities determined from vapor-pressure curves. Niemax and Pichler (1975) studied absorption of Na, K, Rb, and Cs at densities that scaled several orders of magnitude. Accuracy of the experiments are limited by knowledge of number density, but high resolution scans can be performed on the static samples. Absorption in the wings generally exhibits a quadratic dependence consistent with quasi-static broadening theory. Deviations from quadratic behavior are found in the far wings. Initially this was attributed to the difference between Σ and Π potential curves (Niemax and Pichler, 1974), but trends in the data for all alkalis suggest that deviations are produced by distortions of the potentials by avoided crossings. Avoided crossings will occur at interaction energies related to the spacing of the atomic energy levels. For oxygen, this corresponds to energies in the range of about 20-80 cm^{-1}, but the current measurements are not sufficiently numerous or precise to detect such deviations.

Noble gases are also convenient sources of atoms. Resonance broadening affects not only the resonance lines which terminate in the ground state, but also lines whose *lower state is connected to the ground state* by a dipole-allowed transition. Hindmarsh and

Thomas (1961) and Kuhn and Lewis (1969) measured resonance broadening of emission lines in He, Ne, Ar, and Kr. Carefully designed discharges are required to eliminate other broadening mechanisms, but lines whose lower levels connect to the ground state are wider than other lines.

Similar results are expected for oxygen emission lines, so the effects of resonance broadening are also important for transitions other than the VUV triplet studied here. Numerous states are connected to the $2p^4\ ^3P$ ground state by appreciable dipole moments, and transitions terminating in these levels experience resonance broadening. The resonance width is calculated with the dipole moment of the transition to the ground state, not of the transition being considered. For example, the 845 and 437 nm transitions are resonance-broadened because they terminate in $3s\ ^3S°$. On the other hand, the 777 nm triplet terminates in $3s\ ^5S°$, and, as discussed by Chang, *et al*, (1993), is not subject to resonance broadening. Differences in Lorenztian widths between these types of lines depends on the ground state O density. In principle, the differences might be measured to deduce O density in a high temperature flowfield, although in practice this may be difficult to implement. Resonance broadening of lines between excited states should certainly be included in radiative transport calculations, especially for lines which become optically thick.

Resonance interactions are studied in a fundamentally different way with level-crossing measurements. Specifically, vapor atoms are optically pumped into excited states with polarized light, allowing selective excitation of specific m-sublevels of the excited state (Kastler, 1967). Various mechanisms, including resonance interactions with other atoms, cause transitions to other m-sublevels which can be monitored by observing the depolarization of fluorescence emitted from the system. Happer and Saloman (1967) studied resonance interactions with lead whose ground state is ^3P. The electron configuration is $6p^2\ ^3P$, and because the outer shell is less than half full, the order of j-levels is opposite that of oxygen. Splitting of the "ground state" levels is larger by a factor of 50, so only the j=0 level is appreciably populated; collisions with atoms in other j-levels are infrequent. Although measurements and theory agree very well in these measurements, direct comparison to oxygen is not possible. However, these measurements address the behavior of individual m-levels, providing an alternative approach to evaluating resonance interaction models.

5.2.2 Refinement of resonance broadening models

The resonance broadening model presented in Chapter 2 is in good agreement with the empirical broadening coefficient for oxygen. This model contains many approximations,

however, and the effect of these approximations should be evaluated before extrapolating the broadening calculation to substantially different thermodynamic conditions.

The broadening model determines the functional form of the lineshape (Voigt, Lorentzian, inverse power law, etc.). Limiting cases of impact and quasi-static approximations are assumed in the data analysis, although neither is strictly valid. Approximate validity criteria are available (Margenau and Watson, 1936, and Ali and Griem, 1965), but the true validity range of these models has yet to be established (Niemax and Pichler, 1975). Furthermore, the models assume interactions with only the nearest neighbor. Complications introduced by resonance interaction of more than two atoms were outlined by Margenau and Watson (1936), but resonance broadening models generally neglect these interactions which become important at high densities. Finally, the broadening model neglects inelastic collisions. Peach (1984) analyzed the behavior of the lineshape function in the region between the impact and quasi-static limits, including the effects of multiple perturbers. The line shape functions, however, are not valid for resonance interactions which are not additive for multiple perturbers.

Numerical analysis can improve line broadening models because approximations made to achieve closed-form solutions are no longer required. One-term approximations to interaction potentials, for example, can be replaced by more realistic models. King and Van Vleck (1939) pointed out long ago that determining the interaction potential between two atoms is related to calculating the potential curve for a diatomic molecule. Resonance interaction dominates at large interatomic separations, but higher order terms in the power series expansion become important at small separations. Effects of these terms manifest themselves as asymmetries and deviations from Lorentzian behavior in the far line wings. In fact, broadening by collisions with similar atoms is sometimes referred to as self-broadening to acknowledge that such interactions are not limited to dipole-dipole resonance forces.

Tremendous strides in computational chemistry have made calculations of interaction potentials very common, especially for air species like O_2. Saxon and Liu (1977) report *ab initio* potentials for all combinations of oxygen atoms in the lowest ^3P, ^1D, and ^1S states, including the $^3P + {}^3P$ combinations. They subsequently reported similar calculations on several Rydberg states of O_2, including two singlet states arising from the separated atom limit $3s\ {}^3S + {}^3P$ (Saxon and Liu, 1980); however, potentials for all states arising from this configuration are not available. Accuracy of the calculations is not sufficient for detailed broadening calculations, although the authors noted that accuracy was not limited by the state of the art (in 1977). Even without more sophisticated calculations,

judicious analysis with these potentials can provide insight into the limitations of the inverse power law potential.

Evaluation of line broadening with molecular potentials requires consideration of many details not explicitly treated in approximate models. For example, transitions are not allowed between all combinations of upper and lower states, but instead depend on transition probabilities between states of various symmetries. Furthermore, these states correlate with different separated atom limits (*i.e.*, j=2, 1, 0). In the approximate model, these effects are accounted for by an "empirical" factor in the resonance width. In the separated atom limit, the effect of individual m-levels must be determined by explicitly summing over all such levels. Extrapolation of these effects to a pair of interacting atoms is more complicated because angular momenta of the two atoms couple. Transition from the separated atom limit to molecular states, including the effects of degeneracies, has been described by Chang (1967), although excited states and resonance interactions are not considered.

5.3 Diagnostic applications

The original motivation of this work was to develop an optical diagnostic technique to determine the ground state number density of atomic oxygen. In this study, we focused on demonstrating VUV absorption measurements with a tunable laser system and studying the effect of resonance broadening on the absorption line shape. The following section discusses issues related to implementation of the diagnostic, including the applicable range of test conditions and additional technical issues to be resolved.

The appeal of this technique is the ability to measure ground state number density, which can easily be related to the total number density of oxygen atoms. Absorption measurements determine the number density in the j=1 state, and the population fraction in this state is shown as a function temperature in Fig. 5.5. At low temperatures, most of atoms are found in the j=2 level. With increasing temperature, the population ratio between the three levels approaches the 5:3:1 ratio of the degeneracies, and the partition function approaches nine. At much higher temperatures, other states become populated. The partition function increases and the Boltzmann fraction in the ground state gradually decreases. Over a large range of temperatures where oxygen dissociation is important, the Boltzmann fraction is a weak function of temperature. Specifically, the population fraction in j=1 is within 10% of 3/9 from 1100 to 14000 K.

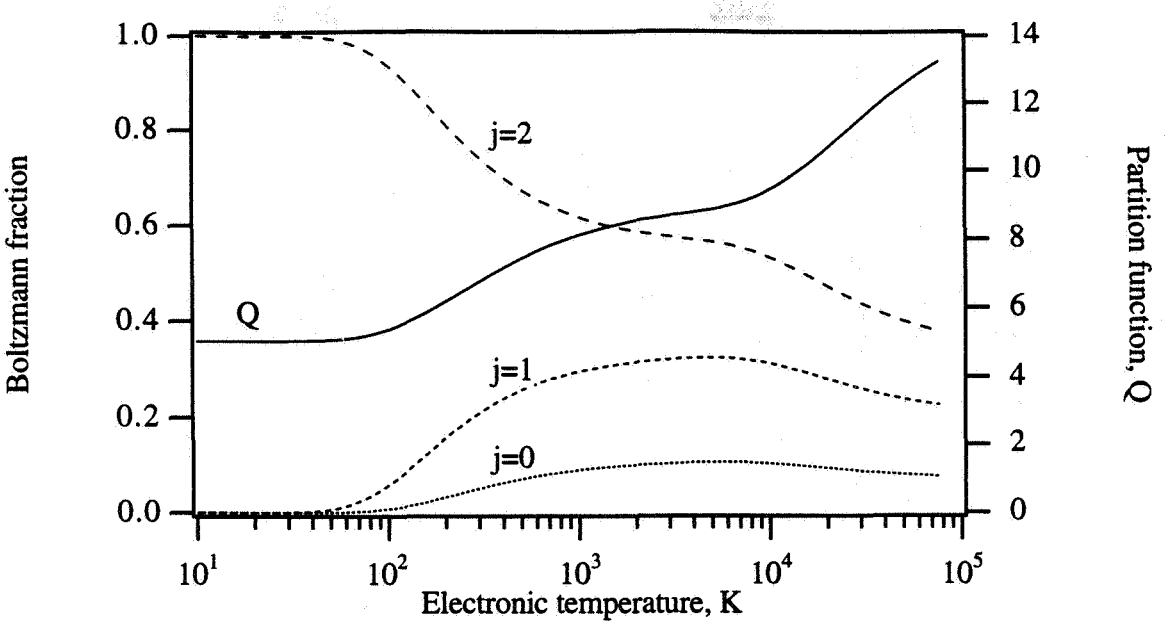

Figure 5.5 Variation of Boltzmann population fractions for the ground state sub-levels and the atomic partition function with electronic temperature.

Absorption measurements with a tunable light source have a larger dynamic range than those made with a fixed-wavelength source. Width of the j=1 (130.49 nm) absorption line is shown in Fig. 5.6 for a range of Lorentzian widths and density-pathlength products. Number density on the y-axis refers to the total atomic oxygen number density and is based on the assumption that the Boltzmann fraction for j=1 is one-third. Calculations assume a Lorenztian shape; Gaussian contributions are neglected, which is approximately valid for the conditions shown on this plot. For lines narrower than those shown, Doppler broadening must be included. The minimum Lorentzian width for which calculations are plotted corresponds to the lifetime linewidth. Absorption linewidths are defined as the full width between 50% transmission points on the j=1 profile. For very wide lines, contributions from the adjacent lines are no longer negligible, and actual widths will be larger than those shown. This plot indicates the relatively large range of density-pathlength products over which measurements can be made. At lower widths, the laser linewidth must be deconvolved from the absorption profile; at higher widths, adjacent lines must be accounted for and direct measurement of background absorption is difficult.

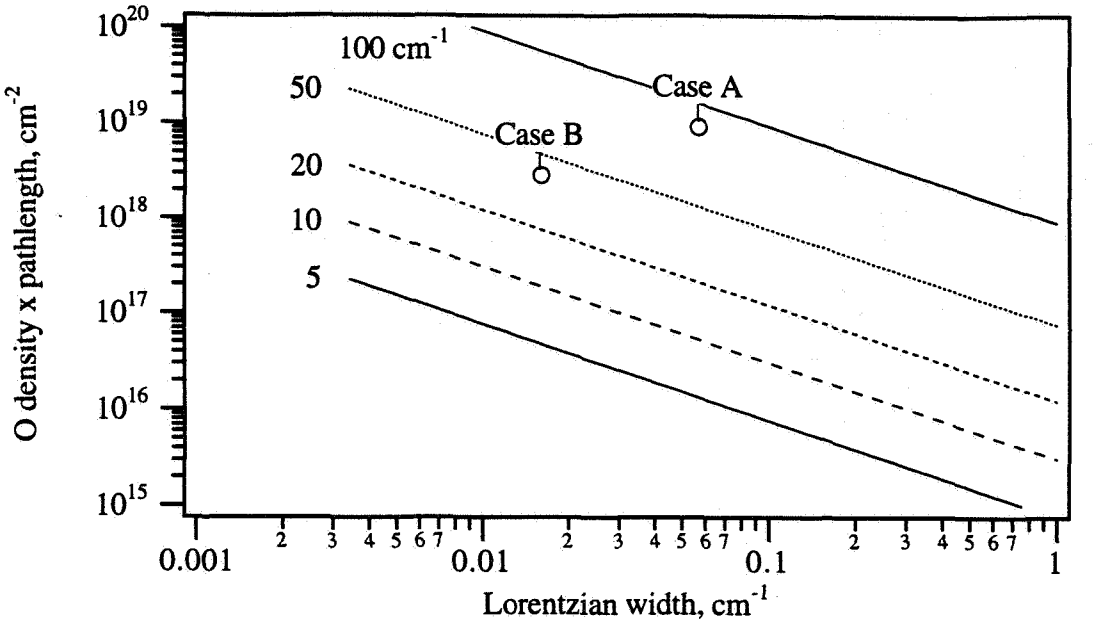

Figure 5.6 Full width at half maximum of absorption line produced as a function of the Lorentzian line width and the product of atomic number density and absorption pathlength.

Similar information can be displayed in an alternative style by plotting the atomic oxygen absorption cross-section as a function of laser frequency relative to the j=1 line. Cross-sections are calculated from Voigt profiles to show the large cross-section at the resonance frequencies, where Doppler broadening is dominant. These cross-sections are relative to total atomic oxygen number density. Results are shown for conditions with only lifetime broadening and for lifetime broadening plus a collisional width ten times larger than the lifetime width. Results are shown in Fig. 5.7a for Doppler widths and population distributions at 6000 K. Populations in j=0 and 1 are lower at room temperature, as shown in Fig. 5.7b.

The broadening coefficient for collisions with other oxygen atoms is deduced from measurements in this chapter, and widths for other colliders are given in Chapter 2. Collisional widths calculated from these coefficients are plotted in Fig. 5.8 as a function of collider density. The Stark interaction is relatively strong, so Stark broadening by electrons is significant for relatively low densities of electrons. Stark broadening by ions is commonly modeled with a quasi-static theory, and is not included in this figure. Resonance widths are calculated from the empirical broadening coefficient reported here. Extrapolation of this result assumes that a Lorentzian profile is a fair prediction of the actual line shape. Van der Waals broadening caused by collisions with other neutral particles is not included in the figure. For this transition, the dipole moment is relatively large, so van

der Waals interactions should be weaker than the resonance interaction. For a given collider density, broadening by a foreign gas should be much smaller than that due to resonance broadening. Sohns and Kock (1992) report a van der Waals interaction constant, C_6, of 6.50×10^{-38} m^6/sec for collisions with argon atoms. If this value is assumed to express the interaction energy in units of rad/sec, it predicts an interaction of 5400 cm^{-1} (0.7 eV) at a separation of 20 Å, which seems high. Other results in the paper are presented in wavelength units, however, so this interpretation may not be correct. Without further experimental data, van der Waals widths can only be estimated from theoretical results.

Broadband absorption is a major potential source of spectral interference. Continuum absorption can be important for a highly ionized test gas, or for one with molecular species that absorb strongly. Vacuum ultraviolet absorption by molecular oxygen is very strong. As discussed in Appendix B, the photodissociation continuum at room temperature passes through a minimum near 130 nm. Nevertheless, this absorption is still strong, and some experimental evidence indicates that it increases at higher temperatures. In Figs. 5.7a and b, continuum absorption coefficients for room temperature and 6400 K are included for reference. On resonance, atomic absorption is tremendously stronger than the photodissociation continuum. When the optical depth on resonance is extremely large, as in the current measurements, the photodissociation continuum is stronger than relevant portions of the atomic profile. Atomic absorption measurements are only possible where dissociation is virtually complete. A baseline measurement is a valuable way to correct for any background absorption, but this is difficult when the lines begin to merge together. Alternatively, a secondary source can measure the background just outside the triplet in the region near 129.5 nm. The photodissociation continuum due to Schumann-Runge contains structure in this whole spectral region, and interpretation of the signal may be somewhat ambiguous. With test conditions such as those encountered in Case A, however, this information may be useful to place an upper limit on the background absorption.

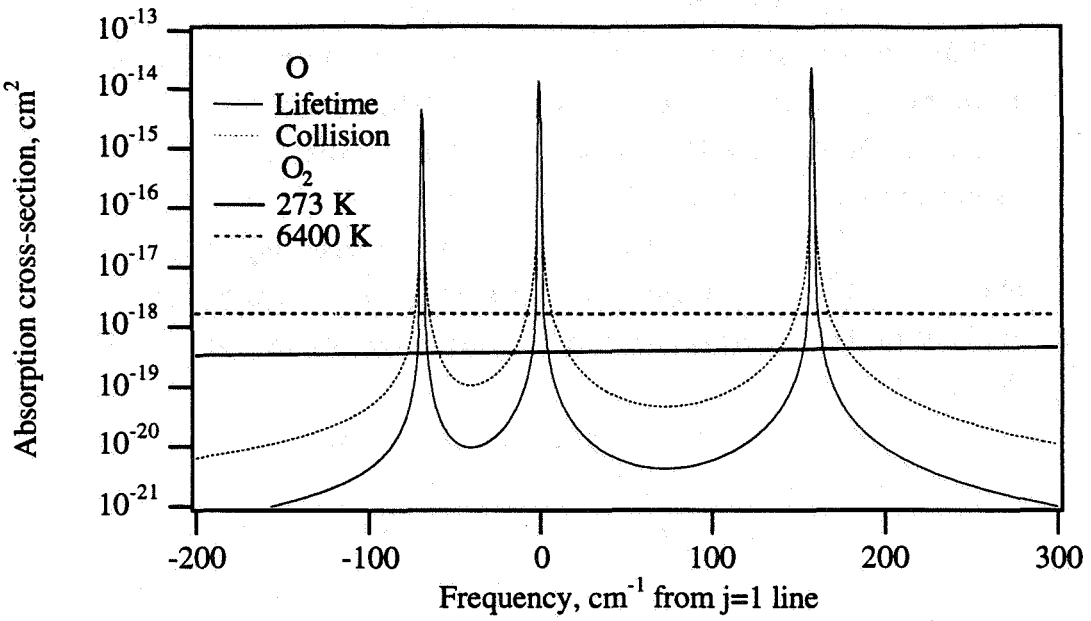

Figure 5.7a Calculated cross-sections for atomic absorption at 6000 K with Lorentzian width given by (1) only lifetime broadening and (2) with lifetime broadening plus a collisional width ten times larger. Molecular cross-sections are shown for comparison.

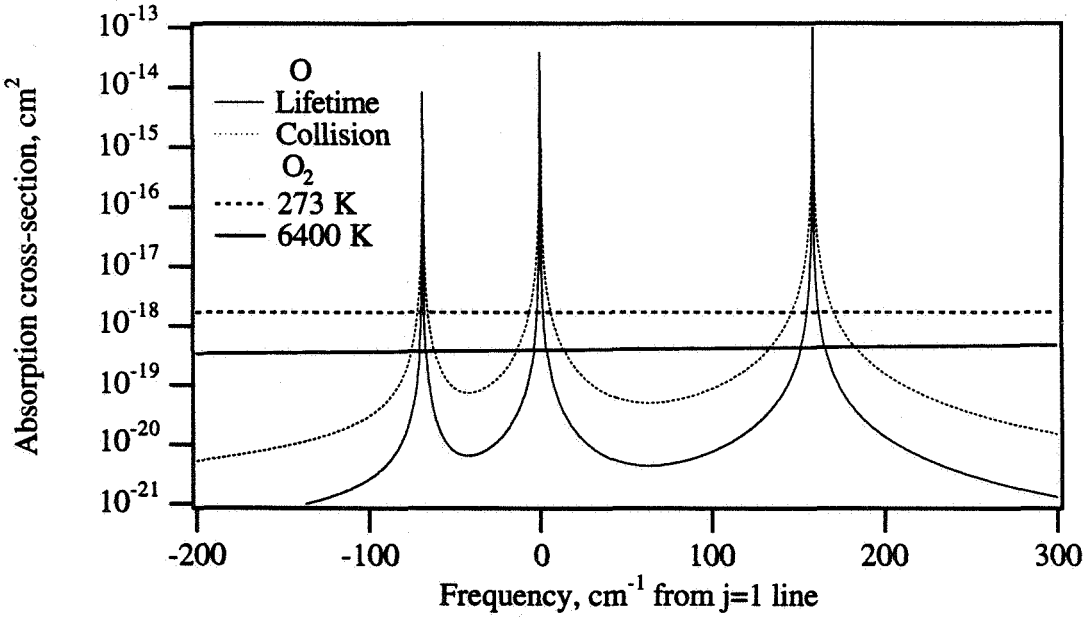

Figure 5.7b Atomic cross-sections with Doppler width and population distribution calculated at room temperature.

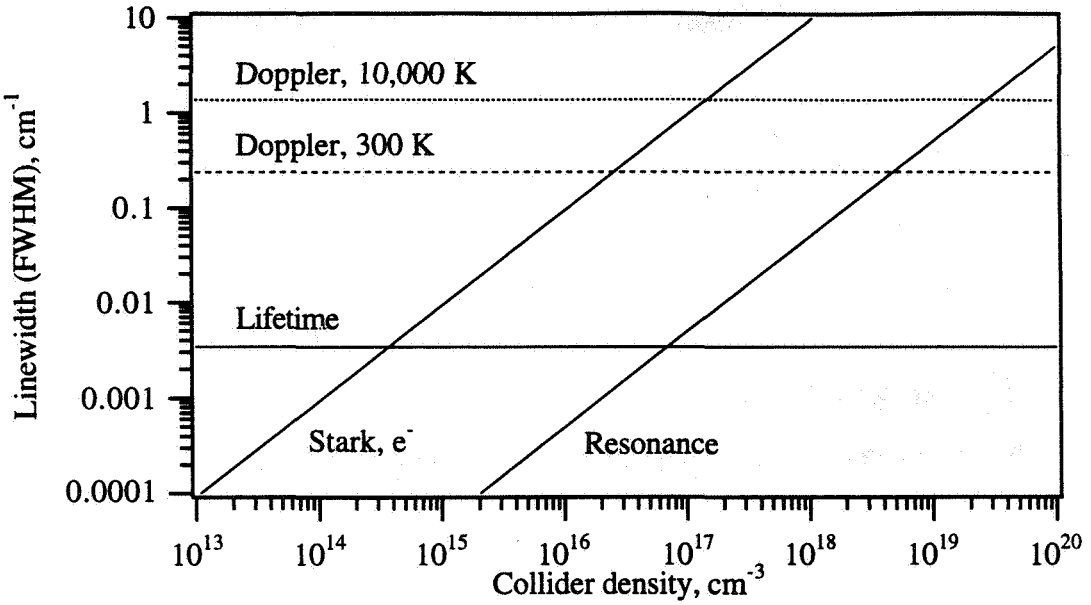

Figure 5.8 Relative importance of various broadening mechanisms at various conditions. Stark broadening caused by collisions with electrons, and resonance broadening by other oxygen atoms.

Chapter 6
Summary and Conclusions

In this chapter, results of this study are summarized. Motivation for this investigation and the experimental approach are reviewed, followed by a summary of the experimental results. Conclusions are presented, and avenues for future work are suggested.

6.1 Summary

This investigation was undertaken to evaluate the potential of atomic absorption measurements as an atomic oxygen concentration diagnostic. Atomic resonance absorption spectroscopy (ARAS) is a demonstrated technique to determine ground state number densities, suitable for single-shot measurements. In principle, ARAS can be performed in gases where collision rates are high. Narrowband resonance lamps limit this technique to low number densities, but a tunable VUV source can extend the technique to substantially higher densities. At these conditions, lifetime and collision broadening dominate the line shape, which had not previously been investigated.

An ArF-pumped Raman shifter is proposed as the tunable VUV source, and its performance has been characterized. By cooling the hydrogen in the Raman shifter with liquid nitrogen, reproducible quantities of 130 nm light were produced by pumping with a commercially available excimer laser. Wavelength and linewidth of this light were measured with laser induced fluorescence in a microwave discharge flow cell, with signals obtained at 130.49 and 130.60 nm. Two prisms and apertures separated the desired beam from other orders, which was detected by KBr solarblind photomultipliers which discriminated against residual laser light at 193 nm.

Performance of this system was demonstrated by measuring resonance line broadening caused by collisions with other oxygen atoms. Atomic oxygen was generated by 6.8 km/sec shock waves in molecular oxygen, producing dissociated test gas with very

little ionization. The absorption profile at 130.49 nm was measured at two test conditions, $3x10^{17}$ and $9x10^{17}$ cm^3 at 6000 K. Both profiles were fitted to Lorentzian profiles, and resonance linewidths deduced from the data compare favorably to theoretical values.

Finally, the potential of this technique as an atomic concentration diagnostic was discussed. The possible range of test conditions depends on a variety of parameters, and various combinations of these parameters were presented to explore the applicability of this technique to other test conditions. Improvements to the experimental hardware and technique, as well as deficiencies of model parameters, were identified.

6.2 Conclusions

The objective of this investigation was to evaluate the potential of atomic absorption measurements by demonstrating single-shot absorption measurements and using them to determine the line shape function under conditions dominated by resonance broadening. A Raman-shifted ArF laser is a suitable light source for single-shot VUV measurements requiring a limited tuning capability. High-order Raman shifting typically exhibits poor conversion efficiency and large shot-to-shot fluctuations. With a liquid nitrogen-cooled cell, however, light shifted to 130 nm is sufficiently bright and reproducible for single-shot absorption measurements.

Measured line shapes are adequately described by Lorentzian profiles, and the empirical linewidths are in accord with those predicted theoretically. These measurements have been made in the intermediate wing region, thousands of Lorentzian widths from the center of the lines. The theoretical models used are not strictly applicable in this region, but agreement between models for different spectral regions suggested that they might be useful here. Indeed, the measured results are in accord with these calculations. Nevertheless extrapolation of these results to other test conditions should be done cautiously. Finally, no shifts of the lines are detected, although the probe linewidth is much larger than any shift that might be expected at this test condition.

VUV absorption measurements appear to be a viable technique for measuring ground state oxygen atom concentrations under certain conditions. Measurements can be performed where spectral interferences are due to continua, not line spectra, and where such absorption is weak enough to allow transmission between the lines. In electronically and vibrationally excited molecules, additional transitions are important; in general the VUV region becomes more congested at high temperatures. At high ionization levels, other continua, such as free-free transitions, become important as well. Interpretation of absorption measurements requires knowledge of the line shape, which is tenuous for foreign gas broadening. Atomic oxygen density measurements are difficult, and the

various techniques available must be evaluated to determine the best approach for a specific test requirement.

6.3 Future work

Future work suggested by this investigation is divided into three categories: experimental improvements and/or refinements, determination of spectroscopic parameters, and applications.

Experimental technique and hardware can be improved in several ways. Measurement precision is primarily limited by uncertainty in the reference beam intensity, discussed at length in a previous chapter. The Raman cell was operated at a low pressure to keep the photomultipliers in a linear range, suggesting that the pump laser energy can be lower. Alternative laser configurations are possible which produce lower energy, but substantially better locking efficiency, tuning range, and/or beam profile. In addition, the laser and beam path should be purged of molecular oxygen to eliminate gaps in the tuning range. Parameters that control the ratio of narrowband to broadband in the VUV beam should be determined, or a monochrometer incorporated into the system to reject broadband light. Perhaps this monochrometer could be used in place of the second prism. Window seals can be improved by sealing the window to the outer flange of the Raman cell. Then, hydrogen pressure inside the cell maintains pressure on the window during thermal cycles. Finally, measurements of transmission below ten percent can be improved substantially by adding a known attenuator to calibrate at the same signal levels expected in the measurement.

Additional spectroscopic data is required to expand the range of applicable test conditions. Improved calculations of resonance broadening should be performed to determine the validity range of the broadening coefficient measured here. Other types of collision broadening must be evaluated as well, including Stark broadening by ions and van der Waals broadening for relevant air species. Broadband absorption by molecular oxygen is discussed in Appendix B, and variation of this important cross-section with temperature is poorly understood as well. Advances in computational chemistry offer the possibility of estimating many of these parameters from *ab initio* calculations.

Ongoing improvements in laser-based VUV generation techniques are opening up important possibilities for spectroscopic measurements. Despite the limitations discussed above, absorption measurements can be used to study ground state populations in other flows and to evaluate computations of these flows. Although the intrumentation is not yet a turn-key system, a laser-based VUV measurement was implemented in a medium-scale research facility. Interest in VUV spectroscopy is certainly not limited to high-enthalpy

flows; these experiments demonstrate that the technology is sufficiently mature that it is no longer limited to benchtop measurements.

Appendix A
Hydrogen Raman Shifting

Stimulated Raman scattering, or Raman shifting, generates the vacuum ultraviolet light required for the absorption measurements. Ultraviolet light at 193 nm from an excimer laser is shifted through a series of nonlinear steps to produce light at 130 nm. The shifting process can be understood by first considering spontaneous Raman scattering, and then stimulated Raman scattering.

A.1 Spontaneous Raman scattering

When a photon interacts with a molecule, several outcomes are possible. The interaction can scatter the photon elastically by Rayleigh scattering, and only the direction (or wave vector) of the photon changes. Alternatively, the molecule can absorb the photon, and the increase in internal energy raises the molecule into an excited state. Absorption occurs when the photon is resonant with the molecule, meaning that its energy matches that required to reach an excited state. Intermediate to these two outcomes is spontaneous Raman scattering.

Raman scattering is produced by inelastic collisions.* The interaction changes both the direction and energy of the incident photon. Figure A.1 illustrates the energy exchange process qualitatively. Like two-photon absorption or emission, Raman scattering occurs between two stationary states of the molecule with an intermediate, virtual state. The first case illustrated is Stokes scattering, in which the molecule is in state A when the incident photon arrives. The wavefunction evolves into a mixture of states A, B, and the virtual state V. The incident photon is annihilated and a second photon created, leaving the molecule in state B. This new photon has a lower energy, and the energy difference is

* Raman scattering is also observed with atoms, but the focus of this discussion is on molecules.

equal to the energy required to raise the molecule from A to B. Anti-Stokes scattering is essentially the reverse process. Interaction with the molecule in excited state B produces a more energetic photon and leaves the molecule in the lower state A. Anti-Stokes scattering occurs when molecules are found in excited states. Normally thermal or electrical excitation populates these states, but we see from the first case that Stokes scattering can populate them too.

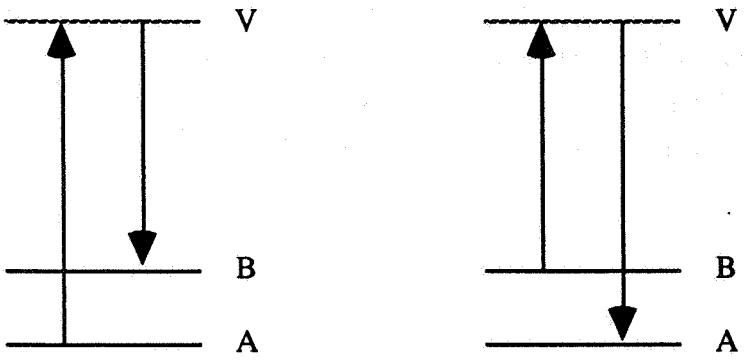

Figure A.1 Schematic illustration of Raman scattering for Stokes and anti-Stokes scattering.

This description explains qualitatively the wavelength shift observed in Raman scattering, but should not be taken too literally. Time-ordered processes in which the molecule is first excited into V by absorption and the second photon emitted do not occur. Behavior of the two photons cannot be separated, and evolution of the whole system must be considered together. The intermediate state V is a virtual state which represents the contribution of all possible intermediate states to the scattering. In special cases, a real state lies near the virtual state, resonantly enhancing the scattering. In general, however, resonant transitions are not involved.

Raman scattering provides valuable spectroscopic data for homonuclear molecules. Exchange symmetry of the nuclei eliminates any dipole moment for vibrational and rotational transitions, so conventional emission and absorption techniques are useless. These transitions are Raman-active, however, and rovibrational transitions can be observed with Raman scattering.

Spontaneous Raman scattering is a very weak process. Scattering intensity is described by the differential cross-section, $\partial\sigma/\partial\Omega$, which gives the scattering cross-section per unit solid angle. This parameter depends on incident polarization and on observation direction. Values are commonly reported for scattering at right angles to the incident beam.

Rovibrational selection rules for Raman scattering are similar to those for infra-red active molecules. The selection rule for vibration is the same as that for dipole-allowed transitions, $\Delta v=0,\pm1$. For rotation, however, the selection rule is $\Delta J=0,\pm2$. The selection rule on J produces a Q-branch ($\Delta J=0$) and O and S branches ($\Delta J=\pm2$). Relative intensity of these branches depends on polarization of the incident light.

A.2 Stimulated Raman scattering

The nature of the Raman process changes at high incident intensities. The incident beam generates a Raman gain medium which amplifies light at the Raman-shifted wavelength. Amplification depends on the intensity of the incident beam and on the Raman gain coefficient. Steady-state gain for plane waves is given by (see, for example, Faris and Dyer, 1993)

$$g = \frac{2\lambda_s^2 \Delta N}{h\nu_s n_s^2 \pi \Delta\nu} \frac{d\sigma}{d\Omega} \tag{A.1}$$

where λ_s, ν_s, and n_s are the wavelength, frequency, and index of refraction for the Stokes wave, ΔN is the population difference between initial and final levels, $\Delta\nu$ is the Raman FWHM, and $d\sigma/d\Omega$ is the differential Raman cross section. Gain increases with the density of the scattering media, and is inversely proportional to the transition linewidth. In many situations, pulsed lasers with moderate or poor beam quality produce the incident (or pump) beam, and the assumptions of steady-state and pure plane waves are not valid. Nevertheless, the expression for the gain coefficient predicts that Raman gain increases with density and increases as the linewidth decreases, in accord with observation. At sufficiently high densities, dispersion of the medium limits conversion efficiency. Phase matching of the various components breaks down, and conversion efficiency decreases with further increases in density.

In practical application of Raman-shifting, wavelength conversion follows several steps. First, the incident pump beam generates the gain medium, amplifying noise photons or Raman-shifted photons at the Stokes frequency. When this first Stokes beam becomes sufficiently intense, it generates a second Stokes beam, whose frequency has been shifted twice from the original pump frequency. This process can continue and produce a cascade of Stokes beams. Interaction between the first Stokes order and the initial pump beam can also produce an anti-Stokes beam, and a series of four-wave mixing processes generate additional anti-Stokes components. For a given Raman transition at frequency ν_R pumped by an incident frequency ν_P, a whole family of beams at wavelengths of $\nu_P \pm \nu_R$, $\nu_P \pm 2\nu_R$,

$\nu_P \pm 3\nu_R$, etc., are produced. Several rovibrational Raman transitions are possible, but one transition frequently dominates all others.

A.3 Raman shifting in hydrogen

Hydrogen is the lightest molecule and has several properties that make it a very convenient medium for Raman scattering. The light nuclei produce a high vibrational frequency, corresponding to large vibrational quanta. Hydrogen's moment of inertia is also small, so energy spacing between rotational levels is unusually large. Available rovibrational states are widely spaced and relatively few states are populated at room temperature. The dominant transitions, and thus frequency of the Raman-shift, depends on the initial state. Competition between various shift frequencies forces shifting to primarily occur from molecules in a single state, which is often the most populated one. Concentrating population in a few states produces a large fraction of available molecules in the dominant state and enhances conversion efficiency. Shifting into the vacuum ultraviolet is further aided by the electronic structure of hydrogen. The absence of transitions not only prevents absorption of photons, but also minimizes dispersion in this region.

Like other homonuclear diatomics, hydrogen has its rotational state populations modified by nuclear exchange symmetry. Specifically, odd levels have an additional degeneracy factor of three and even levels a factor of one. The expression for the Boltzmann fraction is modified so that odd levels have an additional factor of three, and the summation for the partition function is modified accordingly. At room temperature, roughly 3/4 of the molecules are in odd levels. At 77 K and complete equilibrium, population is evenly split between the J=0 and 1 levels. However, conversion of the nuclear spin state is extremely slow, and occurs over several weeks unless special steps are taken to enhance the conversion. Hydrogen in the Raman cell is cooled from room temperature to 77 K in about an hour, so it retains the room temperature ratio of odd to even levels. Consequently, the population distribution cannot be calculated from Boltzmann equilibrium. Most of the population collapses into the J=0 and 1 levels, with about one-fourth in J=0 and three-fourths in J=1.

Raman-shifting in the cell is dominated by transitions from J=1 rather than J=0 because of the non-Boltzmann distribution. Values of the various parameters which determine the Raman gain coefficient are summarized by Faris and Dyer (1993) for H_2, HD, and D_2 for different temperatures. The reported population fractions and calculated gain coefficients in this reference correspond to complete equilibrium. In the cell, the gain coefficient is higher for J=1, although the Raman linewidth for J=0 is smaller.

Raman-shifted wavelengths can be calculated assuming J=1 Q-branch transitions with a spacing of 4155.25 cm^{-1} (Döbele, *et al*, 1987). The sixth anti-Stokes component from 51706 cm^{-1} (193.4 nm) is 6x4155.25 cm^{-1} away at 76637.8 cm^{-1} (130.48 nm). Sidebands produced by O and S-branches can appear about 600 cm^{-1} on either side of the Q-branch, although they are not observed with the current experimental setup. Finally, 2-photon transitions in hydrogen can be accessed by certain specific wavelengths in the ArF tuning band. These transitions can interfere with the Raman conversion when the laser is tuned to these wavelengths, but these regions are relatively small and were avoided in the experiment. Further details on these transitions are given by Faris and Dyer (1993).

Appendix B
Molecular Oxygen Absorption

The vacuum ultraviolet absorption of molecular oxygen is a potential source of interference in absorption measurements of atomic oxygen. The concentration of O_2 places a constraint on the flow conditions in which such absorption measurements can be made. Two types of constraints are possible. The O_2 absorption may contribute a baseline absorption which can be subtracted out. Alternatively, the O_2 absorption may be so strong that the probe beam is completely absorbed, and no measurements are possible. Knowledge of the O_2 absorption cross section at 130 nm is therefore important for planning and analysis of O absorption measurements. These measurements are typically performed at high temperatures, where substantial dissociation occurs.

B.1 Absorption at room temperature

The absorption spectrum of O_2 at room temperature has been studied extensively, and a brief discussion of the general features is helpful in understanding the molecular absorption at higher temperatures. The Schumann-Runge band system ($B^3\Sigma_u^- - X^3\Sigma_g^-$) consists of a line spectrum from about 205 nm to the dissociation limit at 175 nm and a continuum absorption at shorter wavelengths (Hébert, *et al*, 1967). Equilibrium internuclear spacings of the two states are substantially different. The spacing is 1.21 Å for the $X^3\Sigma_g^-$ ground state, and 1.60 Å for the $B^3\Sigma_u^-$ state. Therefore, the $X^3\Sigma_g^-$, v"=0 and $B^3\Sigma_u^-$, v'=0 wavefunctions do not overlap significantly, and absorption from v"=0 increases with the vibrational quantum number of the upper state v'.

Absorption of photons with wavelengths shorter than 175 nm leads to photodissociation (Fig. B.1). Strength of the photodissociation continuum depends on the overlap integral between vibrational wavefunctions of the upper (repulsive) and lower (bound) states. The vibrational wavefunction of the unbound upper state is concentrated

near the classical turning point, and that of $X^3\Sigma_g^-$, v"=0 is concentrated near the equilibrium distance of 1.21 Å. Therefore, the peak in the overlap integral is expected at the same internuclear distance on the upper state potential curve, i.e. in the absorption continuum. This peak is observed experimentally at about 145 nm.

Below 145 nm, the absorption continuum becomes more complicated. The measured absorption coefficient decreases with wavelength, until a strong absorption peak at 124.4 nm (Ogawa and Ogawa, 1975), attributed to the $E^3\Sigma_u^-$ state* by Buenker and Peyerimhoff (1976) and Yoshimine, *et al* (1976). The measurements of Ogawa and Ogawa also show a peak at 135.6 nm and subsidiary maxima at 134 and 129 nm.

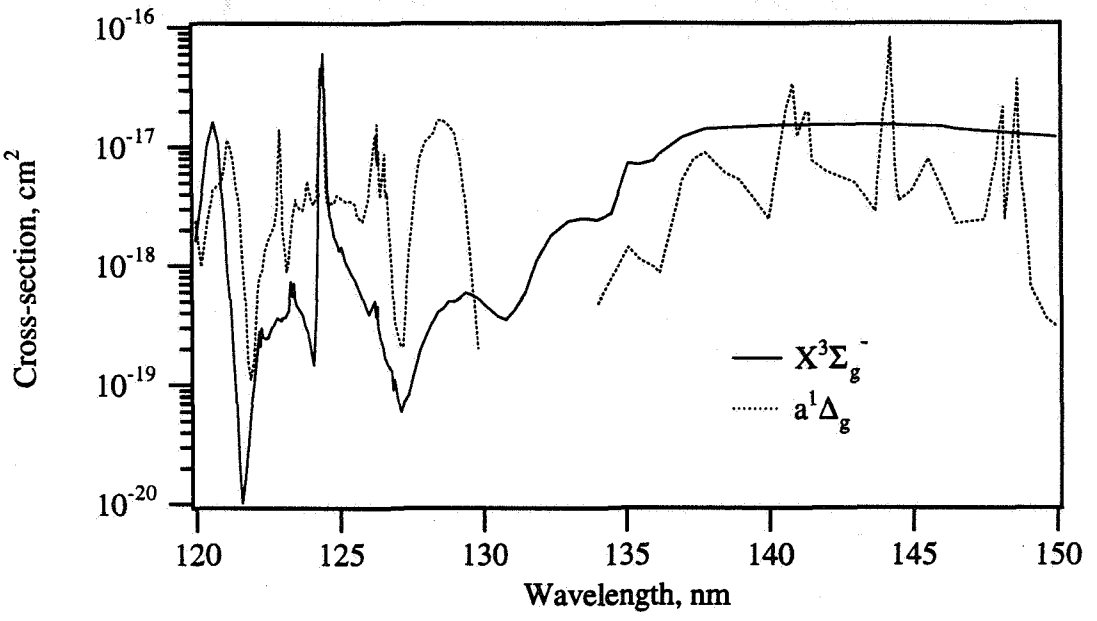

Figure B.1 Absorption cross-section for oxygen ground state and first excited electronic state as reported by Ogawa and Ogawa (1975).

Based on molecular structure calculations, two effects have been suggested to account for the behavior in the region between 125 and 145 nm. The first effect is due to a change in the $B^3\Sigma_u^-$ state at internuclear separations less than 1.2 Å. The $E^3\Sigma_u^-$ state responsible for the peak at 124.4 nm has an avoided crossing with the $B^3\Sigma_u^-$ state, changing the character of $B^3\Sigma_u^-$ from valence to Rydberg. The avoided crossing leads to an abrupt decrease in the transition moment and to changes in the shape of the $B^3\Sigma_u^-$ potential curve. These changes account for the decrease in absorption and for some of the structure observed in the continuum. The second effect is absorption into another state, the repulsive

* The $E^3\Sigma_u^-$ state has also been denoted $2^3\Sigma_u^-$ and $B'^3\Sigma_u^-$.

$1^3\Pi_u$ state. Assignment of the 135.6 nm peak to the $1^3\Pi_u$ state is supported by the measurements of Lee, *et al* (1977) and by the calculations of Allison, *et al* (1982). Experimental measurements have been approximately reproduced by Allison, *et al* (1986) by empirically adjusting the potential curves and transition moments, including absorption into both the $B^3\Sigma_u^-$ and $1^3\Pi_u$ states. Therefore, the room temperature absorption continuum at wavelengths longer than 145 nm can be predicted reliably, but our understanding of the continuum at shorter wavelengths is restricted to empirical models.

B.2 Absorption at elevated temperature

The description of the absorption continuum at higher temperatures is less satisfactory. An approximate analysis of the continuum between a bound lower state and an unbound upper state shows that absorption from v">0 occurs at wavelengths both longer and shorter than from v"=0 alone (Herzberg, page 393, 1950). If the transition moment is relatively insensitive to internuclear spacing, the continuum is expected to broaden with increasing temperature. As indicated by the room temperature continuum, however, the transition moment for the Schumann-Runge band changes drastically at close internuclear separations. Therefore, the Schumann-Runge continuum is expected to increase at longer wavelengths with increasing temperature, but not necessarily at shorter wavelengths.

Evans and Schexnayder (1961) report high-temperature absorption measurements made in a shock tube, as well as calculations of Schumann-Runge absorption for v">0. The data were collected immediately behind the shock front, before significant dissociation occurred, at wavelengths from 130 to 175 nm with a resolution of 1.1 nm FWHM. Absorption cross-sections were calculated twice, first assuming a constant transition moment, and then with a "corrected" transition moment empirically derived from room temperature cross-sections. The calculated values agree with the measurements at wavelengths above 140 nm. For the data points at 130, 135, and 137.5 nm, the agreement is less satisfactory. In this spectral region, the measured values lie between the two calculated values. Due to a lack of further information about the potential curves, a "best estimate" was obtained by taking the average of the "corrected" and "uncorrected" calculations in this region.

Subsequent study of the absorption continuum at room temperature has shown that the transition moment is *not* constant, so there is no physical significance to the "uncorrected" calculation based on it. Thus, there is no longer any basis for the "best estimate" values. No mechanism has been demonstrated to explain the increase in the absorption cross-section measured by Evans and Schexnayder, and the experimental data

must instead be used directly. The objective of the following discussion is to determine if plausible mechanisms exist to explain the experimental values.

Temperature variation of the absorption coefficient at 130 nm depends on at least three factors:

1) Cross-sections for the transitions observed at room temperature ($B^3\Sigma_u^-$-$X^3\Sigma_g^-$ and $1^3\Pi_u$-$X^3\Sigma_g^-$) depend on the vibrational and rotational population distribution.
2) Transitions to other, higher energy electronic states may be possible for $X^3\Sigma_g^-$ with v">0.
3) Transitions can occur from other low-lying electronic states, such as $a^1\Delta_g$ and $b^1\Sigma_g^+$, which become increasingly populated at higher temperatures.

Allison, *et al* (1971) report calculated cross-sections for Schumann-Runge absorption from v"=0, 1, and 2. As expected, the dissociation continuum limit moves to longer wavelengths with increasing v". The broad continuum of v"=0 is split by one node for v"=1 and by two nodes for v"=2, but all give roughly the same value at 130 nm. However, as v" increases from 0 to 2, the first peak of the absorption curve moves from 145 to 137 nm. If this trend continues to higher vibrational states (v">2), then the observed increase in the absorption coefficient might be explained by this mechanism. Calculations for temperatures of 295 and 575 K by Wang, *et al* (1987) demonstrate the importance of both rotational and vibrational quantum numbers of the absorbing molecule in predicting the structure observed in the photoabsorption continuum. Results published to date are insufficient to determine if this transition is responsible for the observed increase in the cross-section.

The transitions (v'=0, 1, 2 $\leftarrow$ v"=0) of $E^3\Sigma_u^-\leftarrow X^3\Sigma_g^-$ have been observed at room temperature (see, for example, Chan, *et al*, 1993). The (0,0) transition is found at 124.4 nm, so the (0,3) transition is energetically accessible at 130 nm. Importance of this transition depends on the transition moment and on the vibrational wavefunctions for the relevant transitions. Although the equilibrium internuclear distances for the two states are similar, the upper state potential is much steeper (Yoshimine, *et al*, 1976). Consequently, Franck-Condon factors for transitions where v' < v" are small. As discussed below, however, the transition moment varies dramatically with internuclear distance, and relative intensities cannot be predicted by Franck-Condon factors.

Approximate calculations show that absorption cross-sections from $E^3\Sigma_u^-\leftarrow X^3\Sigma_g^-$ at high temperature may be comparable to those due to the Schumann-Runge system near

130 nm. Oscillator strengths of the bands (v'=0, 1, 2 ← v"=0, 1, 2,3, 4) have been calculated with the transition moments reported by Yoshimine, *et al* (1976) and Li, *et al* (1992), as illustrated in Fig. B.2. Results of these calculations are tabulated in Table B.1. Approximate values for the transition moments are read from figures in the original publications. The resulting errors can be evaluated by comparing the oscillator strengths calculated here with those presented in the original publications, which are also listed in the table. Calculated oscillator strengths are sensitive to the form of this moment, especially for high vibrational levels whose wavefunctions have rapid oscillations. As expected from the relative positions of the potential curves, the $\Delta v = 0$ sequence is strongest. Variation of the oscillator strengths with v" ($X^3\Sigma_g^-$ levels) is consistent with observations of the hot bands by Black, *et al* (1985). For the absorption v'← v", Black, *et al* (1985) report that the (0,1) and (1,1) hot band transitions are slightly stronger than the corresponding (0,0) and (1,0) "parent" transitions, but that the (2,1) transition is about seven times stronger than (2,0). This result is qualitatively consistent with the calculated oscillator strengths in Table B.1

Absorption cross sections are estimated from oscillator strengths by assuming a rotational envelope with a FWHM of 0.5 nm, which is consistent with the width of the (1,0) band. The resulting cross sections for $E^3\Sigma_u^- \leftarrow X^3\Sigma_g^-$ at 6000 K are compared to the room temperature continuum in Fig. B.3. The cross-section calculations are very sensitive to errors in the transition moment function which is not known accurately. However, these calculations give an order-of-magnitude estimate of the importance of the $E^3\Sigma_u^- \leftarrow X^3\Sigma_g^-$ system, and suggest that this system should be considered in the calculation of absorption cross-sections at high temperatures.

Molecular oxygen has two low-lying electronic states arising from the same configuration as the ground state, and transitions from these states may also contribute to absorption at high temperatures. Absorption cross sections for $a^1\Delta_g$ measured by Ogawa and Ogawa (1975) are smaller than cross sections for transitions from $X^3\Sigma_g^-$ at wavelengths greater than 129.8 nm (see Fig. B.1). The vibrational temperature in these measurements may not have been far above room temperature since $a^1\Delta_g$ is a metastable state and these measurements were conducted in the afterglow of a microwave discharge. This data suggests that lower vibrational levels of $a^1\Delta_g$ do not contribute significantly to absorption at 130.4 nm, although absorption from other vibrational levels may be significant. Above $a^1\Delta_g$ lies $b^1\Sigma_g^+$, whose v=0 level is at nearly the same energy as v=9 of the ground state $X^3\Sigma_g^-$. The degeneracy of this state is smaller than that of the other two states, so its relative population is small. The absorption cross-section must be large for this state to contribute significant absorption at 6000 K.

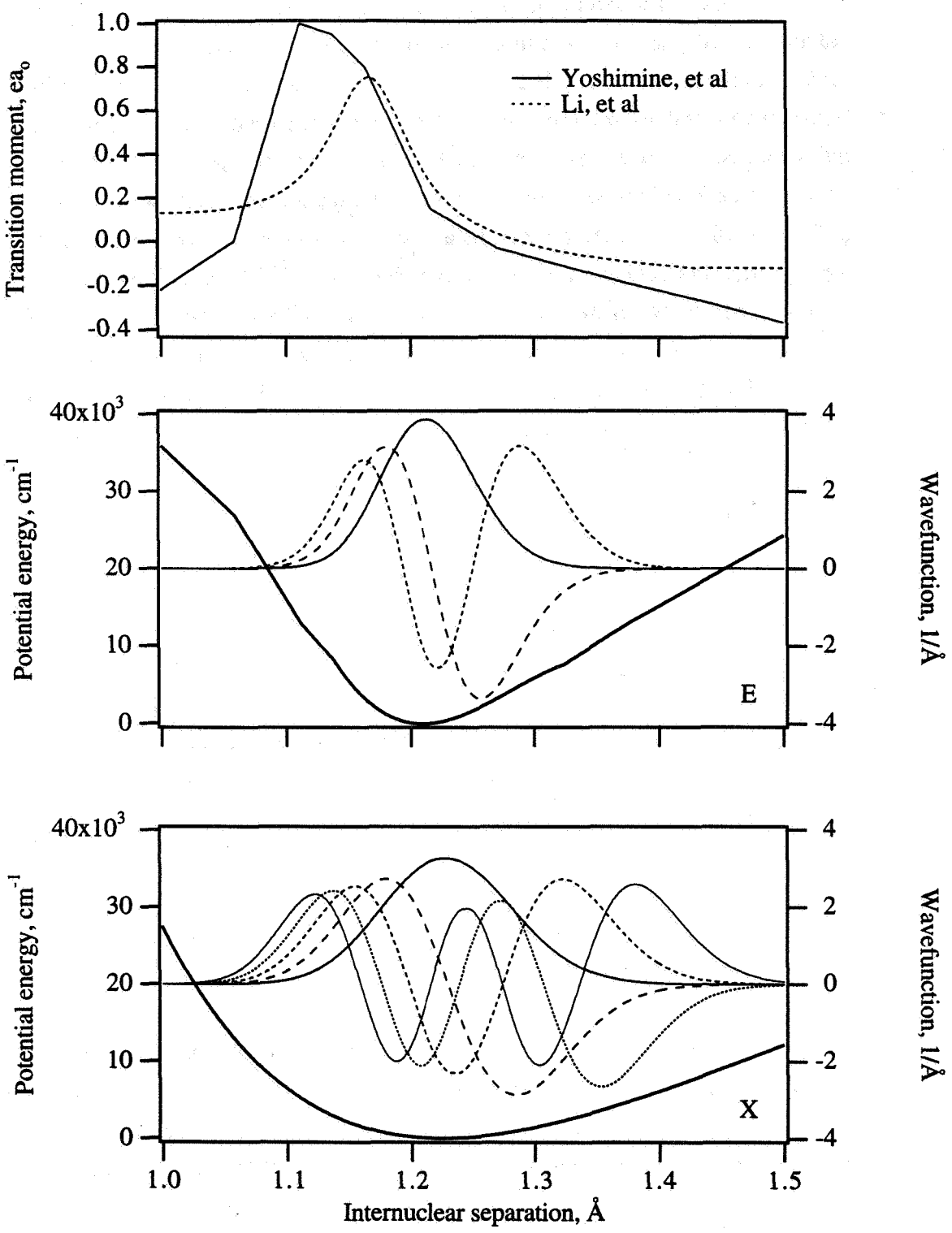

Figure B.2 Transition moment for E-X transition, and potential curves and vibrational wavefunctions for upper and lower levels.

Table B.1 Calculated band oscillator strengths for E-X transition. Values reported in original publications are listed in parenthesis.

	X, v"=0	v"=1	v"=2	v"=3	v"=4
E, v'=0	124.5 nm	127.0 nm	129.5 nm	132.1 nm	134.7 nm
Yoshimine, *et al*	.0127 (.0103)	.0120	.0020	.0001	.0009
Li, *et al*	.0210 (.0174)	.0124 (.0125)	.0007 (.0023)	.0008	.0014
v'=1	120.6 nm	122.9 nm	125.3 nm	127.7 nm	130.2 nm
Yoshimine, *et al*	.0092 (.0124)	.0169	.0144	.0018	.0007
Li, *et al*	.0067 (.0056)	.0193 (.0189)	.0112 (.0159)	.0001	.0025
v'=2	117.3 nm	119.5 nm	121.7 nm	124.0 nm	126.4 nm
Yoshimine, *et al*	.0015 (.0041)	.0167	.0149	.0114	.0012
Li, *et al*	.0007 (.0006)	.0083 (.0088)	.0119 (.0167)	.0064	<.0001

Thus, four mechanisms can be proposed to explain the increase in the absorption cross-section of O_2 with temperature:

1) $B^3\Sigma_u^- \leftarrow X^3\Sigma_g^-$: The perturbation of the $B^3\Sigma_u^-$ state appears to reduce the cross-section at 130 nm below the expected values at room temperature, but absorption from v">2 may still be important.
2) $1^3\Pi_u \leftarrow X^3\Sigma_g^-$: Contributions from v">0 levels may be important.
3) $E^3\Sigma_u^- \leftarrow X^3\Sigma_g^-$: Approximate extension of room temperature measurements and ***ab initio*** calculations to 6000 K suggest that contributions from this transition may be of the same order of magnitude as the room temperature cross section at 130 nm.
4) $? \leftarrow a^1\Delta_g$: Absorption from $a^1\Delta_g$(v"=0) is weak at 130 nm, but strong features nearby suggest that absorption from $a^1\Delta_g$(v">0) may contribute to high-temperature absorption at 130 nm.

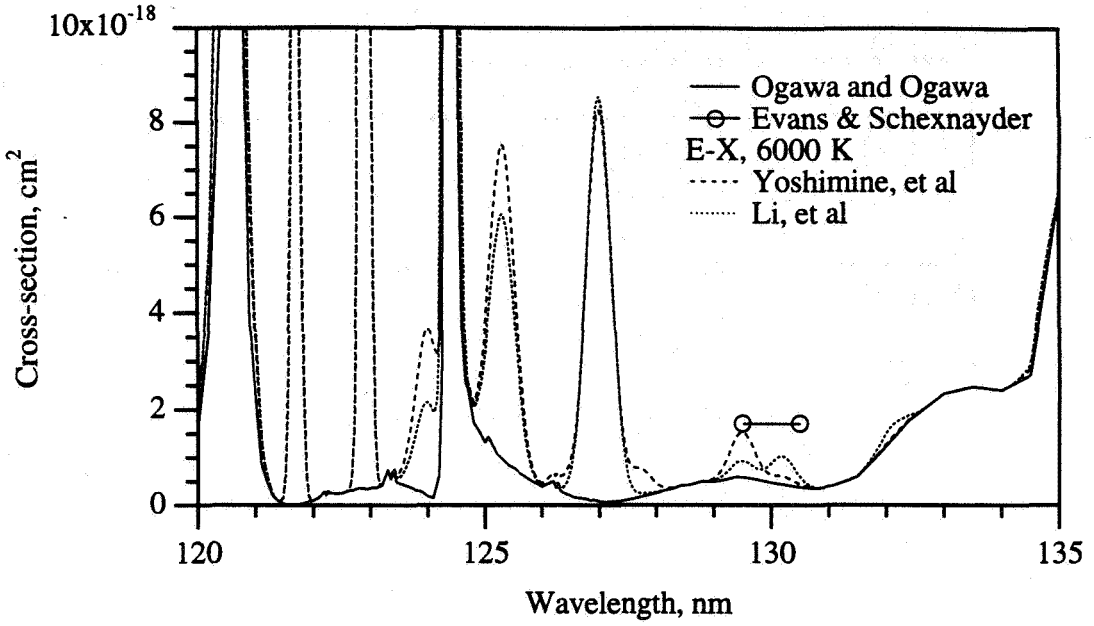

Figure B.3 Estimated absorption by E-X transition at 6000 K showing possible contribution to absorption at 130 nm.

B.3 Boundary layer absorption

High speed flow of the shock-heated test gas produces a boundary layer. Friction and heat transfer at the wall create gradients in the temperature, density, and composition in the boundary layer. Recombination of atomic oxygen near the wall produces a thin layer of molecular oxygen, which produces a background absorption at 130 nm. Background absorption is measured directly in the low density measurements (Case B), but not in the high density measurements (Case A). Absorption by molecular oxygen in the boundary layer is estimated for Case A by calculating boundary layer profiles and then using the temperature-dependent absorption cross-section to find the total absorption through the boundary layer.

A criteria for transition from laminar to turbulent boundary layer is given by Mirels (1971) based on the Reynolds number defined as

$$\mathrm{Re} = \frac{\rho_e u_e (W-1)^2 l}{\mu_e} \tag{B.1}$$

where W is the density ratio across the shock, and the subscript "e" denotes conditions in the "external" flow (see Fig. B.4). Characteristic velocity is the relative velocity of the

flow to the wall, $u_e(W-1)$, and the characteristic length is the distance that the freestream fluid has traveled, $l(W-1)$. Viscosity of dissociated oxygen at 6000 K is 1.79×10^{-3} g/cm sec (Gupta, *et al*, 1990). For the conditions of Case A, absorption measurements are made 6.4 μsec after the shock passes, so that $l = 44$ mm. This corresponds to a Reynolds number of 0.49×10^6. Mirels (1971) cites a transition criteria of $0.5 \times 10^6 < Re < 4 \times 10^6$ for $1 < M_s < 9$. Transition Reynolds number increases with shock Mach number. Since Case A is at $M_s = 20$, the boundary layer is laminar when the absorption is measured.

Ideally the boundary layer profile is found by solving for the complete shock tube flow (for example, Wilson, 1995), but such a calculation is beyond the scope of this work. Instead, the boundary layer profile is determined in two steps. Thickness is estimated from Mirels' (1966) laminar results, and then the molecular oxygen profile is approximated by a flat plate boundary layer calculated for similar conditions. Mirels (1966) tabulated boundary layer thicknesses for ideal gases and for real air (assuming chemical equilibrium). Three thicknesses are tabulated: displacement and momentum thicknesses, corresponding to equivalent density and momentum, respectively, and the velocity thickness, corresponding to the point at which the difference from the freestream velocity is 1% of the total velocity difference across the boundary layer. Results of calculations 44 mm behind the shock are shown in Table B.2, and differences due to chemistry effects (oxygen vs. air) are discussed below.

Table B.2 Boundary layer thickness for Case A (1.0 Torr initial pressure)

Boundary layer thickness	Mirels	Flat plate		
		Eqbm.	Fin. rate	Frozen
Momentum, δ	5.0 mm	9.0 mm	7.3 mm	6.5 mm
Displacement, δ_ρ	0.24 mm	0.62 mm	0.36 mm	0.23 mm
Velocity, δ_u	0.83 mm	0.72 mm	0.84 mm	0.93 mm

The concentration profile of molecular oxygen is required to determine absorption through the boundary layer. Mirels' tabulates results for boundary layer thicknesses only, so profiles are approximated by calculations of a flat plate boundary layer. The two flowfields are illustrated in Fig. B.4. Mirels' shock tube flow is in shock-fixed coordinates with the wall moving away from the shock at $u_w = U_s = 6800$ m/sec, the shock speed. Speed of the external flow relative to the wall is $u_w - u_e = 6314$ m/sec. The flat plate analogy is for a fixed wall. Free stream flow speed is still $u_w - u_e$, and thermodynamic conditions in the free stream are identical to the shock tube external flow. Computations of the boundary

layer are performed with GASP, a commercially-available fluid dynamics software package by Aerosoft, Inc. (Blacksburg, Virginia). Laminar boundary layer calculations are performed for equilibrium, finite rate chemistry, and frozen chemistry for a mixture of atomic and molecular oxygen. A second-order implicit scheme is used with Roe flux splitting, and several grid refinements verify grid independence of the solutions. The Sutherland model is used for temperature dependence of the coefficient of viscosity.

The flat plate boundary layer calculation matches relative speeds and thermodynamic conditions, but the velocity transformation changes the relative direction of the boundary layer flow. Gas in the flat plate boundary layer decelerates, but in the shock tube model, it accelerates. At a given position behind the shock, gas in the shock tube boundary layer is from upstream of that position. In other words, gas in the shock tube flow has spent less time in the boundary layer than in the flat plate flow. Consequently, there is no direct relation between distance behind the shock and distance from the leading edge of the flat plate. The most important consequence of this difference is that finite rate chemical calculations from the flat plate are not directly applicable to the shock tube flow. Boundary layer thickness for equilibrium flow along the flat plate is compared to that calculated by Mirels. Boundary layer thicknesses 44 mm from the leading edge are shown in Table B.2. Displacement and momentum thicknesses for the flat plate are both significantly larger, but the velocity thickness (99% velocity point) is nearly the same. At this station, the flat plate boundary layer is a fair approximation to that in the shock tube.* Although the thicknesses due to Mirels are for real air, thicknesses for pure oxygen should be similar. Flat plate calculations with finite rate chemistry and frozen flow (fully dissociated) give similar results for momentum and velocity thicknesses, and smaller values for displacement thickness. Since the velocity thickness indicates the physical extent of the boundary layer in the flow, the similarity in values for the different flat plate calculations suggest that chemical reactions have a limited effect on the velocity boundary layer. Therefore, the flat plate solution for this boundary layer thickness provides a conservative estimate of the molecular oxygen profile in the shock tube boundary layer.

Absorption by molecular oxygen in the boundary layer is found by integrating through the boundary layer, and multiplying by two to account for boundary layers at both the entrance and exit shock tube windows. Temperature in the boundary layer varies from 300 K at the wall to 6000 K in the external flow, but variation of the absorption cross-

---

* The distance from the leading edge should be of the same order of magnitude as the distance behind the shock, and was selected as a first approximation. However, the agreement between the two distances seems to be fortuitous.

section with temperature is not known. Several approximate models of the temperature variation are evaluated to determine their effect on boundary layer absorption.

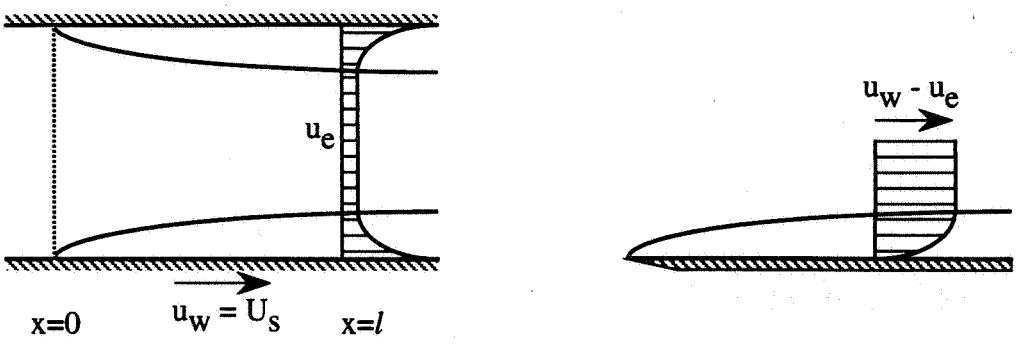

Figure B.4. Boundary layer flow geometries. (a) Flow in a shock tube with shock-fixed coordinates. (b) Flow over a flat plate with same relative flow speed.

The various models, and resulting boundary layer absorptions, are summarized in Table B.3. Cross sections at 300 K (σ_{cold}) and 6000 K (σ_{hot}) are 3.7×10^{-19} cm^2 and 1.6×10^{-18} cm^2, respectively (see Sections B.1 and B.2). Calculations assuming $\sigma=\sigma_{hot}$ and $\sigma=\sigma_{hot}$ for T>1000 K are the least realistic, because they imply a dramatic change in absorption without substantial changes in the electronic or vibrational population distributions. While very approximate, the model $\sigma=\sigma_{hot}$ for T>4000 K is more realistic because excited electronic and vibrational states are becoming populated at 4000 K. In any case, these approximate models place probable upper and lower limits on the boundary layer absorption. These calculations demonstrate that molecular oxygen in the boundary layers produce a background absorption of about 5%±5%, consistent with values assumed in analysis of the absorption data.

Table B.3 Background absorption for equilibrium boundary layer

Cross section model	Functional form	Absorption
Constant, cold	$\sigma=\sigma_{cold}$	1.9%
Linear	$\sigma=\sigma_{cold} + \frac{T-300}{6000-300}(\sigma_{hot} - \sigma_{cold})$	4.0%
Step at 4000 K	$\sigma=\sigma_{cold}$, T<4000 K $\sigma=\sigma_{hot}$, T>4000 K	2.6%
Step at 1000 K	$\sigma=\sigma_{cold}$, T<1000 K $\sigma=\sigma_{hot}$, T>1000 K	6.5%
Constant, hot	$\sigma=\sigma_{hot}$	7.8%

Appendix C
Data Analysis Macros

Data is analyzed by the following series of macros for Igor, an analysis package from Wavemetrics (Lake Oswego, Oregon). Various physical constants and spectroscopic parameters are defined by Initialize. Line shape functions are calculated from MakeVoigt, MakeDoppler, and MakeStatic. Radiative transfer through a uniform slab is calculated by RadTransfer, with an incident spectrum in the wave Incident and the emerging spectrum in the wave Transmission. Black body radiation is also included at the specified electronic temperature. Sample calculations for all three atomic oxygen lines are performed by ThreeLines.

```
Macro Initialize()
        | Initializes constants and parameters used throughout these macros
        | Units are cgs unless otherwise noted and intensity (as well as lineshapes, absorption coeff's,
        | half-widths, etc.) are in wavenumbers.
        | Omass in a.m.u.'s
        | Einstein coeff's from Hibbert, et al.

        Variable/G light=2.9978e10,Avogad=6.0220e23,Boltz=1.38066e-16,Planck=6.6262e-27
        Variable/G charge=1.60219e-19,permitv=8.85419e-21
        Variable/G hck,sigA21,Omass=15.9994
        Variable/G lambda0=1306.0286e-8,Einstein0=.706e8,Elower0=226.977,glower0=1,center0
        Variable/G lambda1=1304.8576e-8,Einstein1=2.12e8,Elower1=158.265,glower1=3,center1
        Variable/G lambda2=1302.1685e-8,Einstein2=3.55e8,Elower2=0,glower2=5,center2
        Variable/G n0,n1,n2
|       Variable/G lambda=7771.9e-8,Einstein=3.55e7,Elower=73764.,glower=5
        Variable/G Starkgam=7.840e-4,Starkexpn=0.380    |Starkgam is in Å, changed to wavenumbers
before use.

        center2=Elower1-Elower2
        center1=Elower1-Elower1
        center0=Elower1-Elower0

        sigA21=(3.6+2.1+0.71)*1e8
        hck=Planck*light/Boltz
        EndMacro
```

```
        Function Q(Temperature)
```

```
	| Partition function for O atom at electronic temperature
	Variable Temperature
	Variable dum
	dum=glower2*exp(-hck*Elower2/Temperature)	| 3P states
	dum+=glower1*exp(-hck*Elower1/Temperature)	| 3P states
	dum+=glower0*exp(-hck*Elower0/Temperature)	| 3P states
	dum+=5*exp(-hck*15867.862/Temperature)	|add 1D states, next term @ 33793 cm-1
	return dum
	End
```

```
	Function Q3P(Temperature)
	| Summation for 3P at electronic temperature
	Variable Temperature
	Variable dum
	dum=5+3*exp(-hck*158.29/Temperature)+exp(-hck*226.99/Temperature)	| 3P states
	return dum
	End
```

```
	Macro MakeDoppler(Ttrans)
	Variable/G light,lambda,Boltz,Omass,Avogad
	Variable Ttrans,width,normalize
	| cgs units are used to get the values in cm-1

	|width is the FWHM in this macro
	width=light*lambda/sqrt(8*ln(2)*Boltz*Ttrans*Avogad/Omass)
	width=1/width
	normalize=sqrt(4*ln(2)/(pi*width^2))
	doppler=normalize*exp(-4*ln(2)*(x/width)^2)
	print width
	EndMacro
```

```
	Macro MakeVoigt(Opercc,Telect,Ttrans,epercc,factor)
	Variable Opercc,Telect,Ttrans=-5,epercc,SigJ,factor
	Variable/G light,Avogad,Boltz,Planck,hck,Omass
	Variable/G lambda,Einstein,Elower,glower,Starkgam,Starkexpn,center
	Variable wnatural,wstark,wresonance,wl,nlower,C3
	Variable wl,wg,wv,d,alpha,beta,lv,normalize

	if(Ttrans<0)	| Ttrans < 0 for single temperature model
		Ttrans=Telect
	endif

	| Line widths for lorentzian components in wavenumbers (wl):
		wnatural=(Einstein2+Einstein1+Einstein0)/(2*pi*light)	| Sum of rates out of upper
level
		| wnatural=1.18e-4*58.7303 | STRAD1 method for comparison only

		wstark=2*(1e-8*Starkgam/lambda^2)*(Telect*1e-4)^Starkexpn*(epercc*1e-16)

		n2=glower2*exp(-hck*Elower2/Telect)	| 3P states
		n1=glower1*exp(-hck*Elower1/Telect)	| 3P states
		n0=glower0*exp(-hck*Elower0/Telect)	| 3P states
		SigJ=(sqrt(5/3)*n2+n1+sqrt(1/3)*n0)*Opercc/Q(Telect)
		|print n2,n1,n0,SigJ/Opercc, "compare to 1.1147"
		wresonance=sqrt(7/3)*lambda1^3*Einstein1/(16*pi^3*light)*SigJ	| Lochte-
Holtgreven, pp. 120-124
		wl=factor*(wnatural+wstark+wresonance)

	| Line width for gaussian component in wavenumbers (wg).
	| In short, wg=1/(18.2249*sqrt(M/Temperature))
	wg=(2*sqrt(ln(2)))/(light*lambda/sqrt(2*Boltz*Ttrans*Avogad/Omass))

	print "wnatural=",wnatural,"wstark=",wstark,"wresonance=",wresonance
	print "Lorentzian and Gaussian FWHM in wavenumbers=",wl,wg
```

```
        | This approximation to Voigt follows the notation of Whiting and Park, TM102829,
        | entitled, "Radiative Heating at the Stagnation Point of the AFE Vehicle"
        | cgs units are used to get the values in cm-1

        d=(wl-wg)/(wl+wg)
        alpha=0.18121
        beta=0.023665*exp(0.6*d)+0.00418*exp(-1.9*d)
        |R=wv/(wg+wl)=1-alpha*(1-d*d)-beta*sin(pi*d) is used for wv
        wv=(wg+wl)*(1-alpha*(1-d*d)-beta*sin(pi*d))
        | Alternative form in Park's STRAD1:  wv=wl/2+sqrt(wl*wl/4+wg*wg)
        | The two agree to at least 1% for all ratios of wl/wg
        lv=wl/wv

        Duplicate Voigt xc2 xc225
        xc2=((x-center)/wv)^2
        xc225=(abs((x-center)/wv))^2.25
        Voigt=(1-lv)*exp(-2.772*xc2)+lv/(1+4*xc2)+0.016*(1-lv)*lv*(exp(-0.4*xc225)-10/(10+xc225))
        normalize=wv*(1.065+0.447*lv+0.058*lv^2)
        Voigt/=normalize
        KillWaves/F xc2 xc225

        EndMacro
```

```
Macro MakeStatic(Opercc,Telect)
        Variable Opercc,Telect
        Variable/G lambda,Einstein,light
        Variable n3P,C3,delw0

        n3P=Opercc*Q3P(Telect)/Q(Telect)
        delw0=lambda^3*n3P*Einstein1/(72*pi^3*light)
        static=(delw0/x)^2*exp(-delw0/abs(x))/delw0
EndMacro
```

```
        Macro RadTransfer(Opercc,Telect,pathlength,lineshape,inlight)
        Prompt lineshape,"Enter wave with the lineshape", popup "Voigt;Static;Doppler;Lorentz"
        Prompt inlight,"Enter wave with incident radiation", popup "incident"
        Variable/G light,Planck,hck
        Variable/G lambda,Einstein,glower,Elower
        Variable Opercc,Telect
        Variable pathlength=10.,nlower,xsection
        Variable/D black
        String lineshape,inlight

        nlower=Opercc*glower*exp(-hck*Elower/Telect)/Q(Telect)
        xsection=(1/4)*(3/glower)*lambda^2*Einstein  | cm^2 rad/sec
        xsection/=(2*pi*light) |cm^2 wavenumber
        print "xsection=",xsection,nlower,Opercc,Telect,pathlength,glower,Elower

        black=2*Planck*light^2/(lambda^5*(exp(hck/lambda/Telect)-1)) | Planck in erg/sec/cm^3 s.r.
        black*=1e-7*1e-4            | Planck in W/cm^2 um s.r.

        opdepth=exp(-nlower*xsection*pathlength*$lineshape)
        transmission=$inlight*opdepth+black*(1-opdepth)

        EndMacro
```

```
Macro ThreeLines(Opercc,Telect,Ttrans,epercc,factor)
        Variable Opercc,Telect,Ttrans=-5,epercc,SigJ,factor=1
        Variable/G light,Avogad,Boltz,Planck,hck,Omass,center
        Variable/G lambda,Einstein,Elower,glower,center,Starkgam,Starkexpn
        print factor
        lambda=lambda2
        Einstein=Einstein2
```

```
        glower=glower2
        Elower=Elower2
        center=center2
        MakeVoigt(Opercc,Telect,Ttrans,epercc,factor)
        incident=1e8
        RadTransfer(Opercc,Telect,10,"Voigt","incident")

        lambda=lambda1
        Einstein=Einstein1
        glower=glower1
        Elower=Elower1
        center=center1
        MakeVoigt(Opercc,Telect,Ttrans,epercc,factor)
        incident=transmission
        RadTransfer(Opercc,Telect,10,"Voigt","incident")

        lambda=lambda0
        Einstein=Einstein0
        glower=glower0
        Elower=Elower0
        center=center0
        MakeVoigt(Opercc,Telect,Ttrans,epercc,factor)
        incident=transmission
        RadTransfer(Opercc,Telect,10,"Voigt","incident")
EndMacro
```

List of References

Ali, A. W., and Griem, H. R., "Theory of Resonance Broadening of Spectral Lines by Atom-Atom Impacts," Phys. Rev., Vol. 140, No., 4A, pp. A1044-1049, Nov. 1965.

Allison, A. C., Dalgarno, A., and Pasachoff, N. W., "Absorption by Vibrationally Excited Molecular Oxygen in the Schumann-Runge Continuum," Planet. Space Sci., Vol. 19, pp. 1463-1473, 1971.

Allison, A. C., Guberman, and S. L., Dalgarno, A., "Photoabsorption Into the $^3\Pi_u$ State of O_2," J. Geophys. Res., Vol. 87, pp. 923-25, Feb. 1982.

Allison, A. C., Guberman, and S. L., Dalgarno, A., "A Model of the Schumann-Runge Continuum of O_2," J. Geophys. Res., Vol. 91, pp. 10193-98, Sept. 1986.

Baer, D. S., Chang, H. A., and Hanson, R. K., "Semiconductor Laser Absorption Diagnostics of Atomic Oxygen in an Atmospheric-pressure Plasma," JQSRT, Vol. 50, No. 6, pp. 621-633, 1993.

Bamford, D. J., Jusinski, L. E., and Bischel, W. K., "Absolute two-photon absorption and three-photon ionization cross sections for atomic oxygen," Phys. Rev. A., Vol. 34, No. 1, pp. 185-198, July 1986.

Bischel, W. K. Perry, B. E. and Crosley, D. R., "Two-photon Laser-induced Fluorescence in Oxygen and Nitrogen Atoms," Chem. Phys. Letters, Vol. 82, No. 1, pp. 85-88, Aug. 1981.

Bischel, W. K., Perry, B. E., and Crosley, D. R., "Detection of fluorescence from O and N atoms induced by two-photon absorption," Appl. Opt., Vol. 21, No. 8, Apr. 1982.

Bischel, W. K. and Dyer, M. J., "Temperature dependence of the Raman linewidth and line shift for the Q(1) and Q(0) transitions in normal and para-H_2," Phys. Rev. A, Vol. 33, No. 5, pp.3113-23, May 1986. *(a)*

Bischel, W. K. and Dyer, M. J., "Wavelength dependence of the absolute Raman gain coefficient for the Q(1) transition in H_2," J. Opt. Soc. Am. B, Vol. 3, No. 5, pp. 677-682, May 1986. *(b)*

Black, G., Sharpless, R. L., Slanger, T. G., and Taherian, M. R., "The 1150-1300 Å Absorption Spectrum of O_2 at 930 K," Chem. Phys. Lett., Vol. 113, No. 3, pp. 311-313, Jan. 1985.

Brink, D. J. and Proch, D., "Efficient tunable ultraviolet source based on stimulated Raman scattering of an excimer-pumped dye laser," Optics Letters, Vol. 7, No. 10, pp. 494-496, Oct. 1982.

Brown, M. S. and Jeffries, J. B., "Measurement of atomic concentrations in reacting flows through thte use of stimulated gain or loss," Applied Optics, Vol. 34, No. 6, pp. 1127-1132, Feb. 1995.

Buenker, R. J., Peyerimhoff, S. D., and Perić, M., "*Ab-Initio* Vibrational Analysis of the Schumann-Runge Bands and the Neighboring Absorption Region of Molecular Oxygen," Chem. Phys. Lett. Vol. 42, No. 2, pp. 225-231, Sept. 1976.

Celii, F. G. Thorsheim, H. R., Hanratty, M. A., and Butler, J. E., "Oxygen atom detection using third harmonic detection," Appl. Opt., Vol. 29, No. 21, pp. 3135-3142, July 1990.

Chan, W. F., Cooper, G., and Brion, C. E., "Absolute optical oscillator strengths for the photoabsorption of molecular oxygen (5-30 eV) at high resolution," Chem. Phys. Vol. 170, pp. 99-109, 1993.

Chang, H. A., Baer, D. S., and Hanson, R. K., "Semiconductor Laser Diagnostics of Atomic Oxygen for Hypersonic Flowfield Measurements," AIAA 93-0628, 31st Aerospace Sciences Meeting, Reno, NV, Jan. 1993.

Chang, T. Y., "Moderately Long-Range Interatomic Forces," Rev. Mod. Phys., Vol. 39, No. 4, pp. 911-942, Oct. 1967.

Dannenberg, R. E. and Humphry, D. E., "Microsecond Response System for Measuring Shock Arrival by Changes in Stream Electrical Impedance in a Shock Tube," Rev. Sci. Inst., Vol. 39, No. 11, 1692-1696, Nov. 1968.

Dannenberg, R. E., "A Conical Arc Driver for High-Energy Test Facilities," AIAA Journal, Vol. 10, No. 12, pp. 1692-1694, Dec. 1972.

Dasch, C. J. and Bechtel, J. H., "Spontaneous Raman scattering by ground-state oxygen atoms," Optics Letters, Vol. 6, No. 1, pp. 36-38, Jan. 1981.

Demtröder, W., "Laser Spectroscopy," pg. 84, Springer-Verlag, New York, New York, 1982.

Döbele, H. F., Hörl, M., Röwekamp, M., and Reimann, B., "Detection of Atomic Oxygen by Laser-Induced Fluorescence Spectroscopy at 130 nm," Appl. Phys. B., Vol. 39, pp. 91-95, 1986.

Döbele, H. F., Hörl, M., Röwekamp, M., and Reimann, B., "Tuning Ranges of KrF and ArF Excimer Laser Amplifiers and of Associated Vacuum Ultraviolet Anti-Stokes Raman Lines," Appl. Phys. B., Vol. 42, pp. 67-72, 1987.

Dyer, M. J., Pfefferle, L. D., and Crosley, D. R., "Laser-induced fluorescence measurement of oxygen atoms above a catalytic combustor surface," Appl. Opt., Vol. 29, No. 1, pp. 111-118, Jan. 1990.

Evans, J. S., and Schexnayder, C. J. Jr., "An Investigation of the Effect of High Temperature on the Schumann-Runge Ultraviolet Absorption Continuum of Oxygen," NASA Technical Report R-92, 1961.

Faris, G. W. and Dyer, M. J., "Raman-shifting ArF excimer laser radiation for vacuum-ultraviolet multiphoton spectroscopy," J. Opt. Soc. Am. B, Vol. 10, No. 12, pp. 2273-86, Dec. 1993.

Fujii, N., Sato, T., Miyama, H., Shin, K. S., and Gardiner, W. C. Jr., "Shock Tube Studies of Rate Constant For H + O_2 - O + OH By Measuring O and OH Absorption in Rich H_2-O_2 Mixtures," Proceedings of the17th International Symposium on Shock Tubes and Waves, pp. 456-461, 1989.

Goehlich, A., Röwekamp, M., and Döbele, H. F., "Determination of the velocity distribution of sputtered atomic oxygen by laser-induced fluorescence in the vacuum-ultraviolet (130 nm)," Surface Science, Vol. 248, pp. 271-275, 1991.

Griem, H. R., Plasma Spectroscopy, Chapter 4, McGraw-Hill, New York, 1964.

Gupta, R. N., Yos, J. M., Thompson, R. A., and Lee, K., "A Review of Reaction Rates and Thermodynamic and Transport Properties for an 11-Species Air Model for Chemical and Thermal Nonequilbrium Calculations to 30,000 K," NASA Reference Publication 1232, pp. 20-21, 55, August, 1990.

Happer, W. and Saloman, "Resonant Collision Broadening of the $(6s26p7s)^3P_o^1$ State in Lead," Phys. Rev., Vol. 160, No. 1, pp. 23-34, Aug. 1967.

Harris S. J. and Weiner A. M., "Detection of atomic oxygen by intracavity spectroscopy," Optics Letters, Vol. 6, No. 3, pp. 142-144, Mar. 1981.

Hébert, G. R., Innanen, S. H., and Nicholls, R. W., "Identification Atlas of Molecular Spectra, 4. The O_2 $B^3\Sigma_u^-$ - $X^3\Sigma_g^-$ Schumann-Runge System," York University, Toronto, Ontario, Jan. 1967.

Herzberg, Gerhard, "Molecular Spectra and Molecular Structure: I. Spectra of Diatomic Molecules," second edition, D. Van Nostrand Company, Inc., Princeton, N. J., 1950.

Hibbert, A., Biémont, E., Godefroid, M., and Vaeck, N., "E1 Transitions of astrophysical interest in neutral oxygen," J. Phys. B: At. Mol. Opt. Phys., Vol. 24, pp. 3943-3958, 1991.

Hilborn, R. C., "Einstein coefficients, cross sections, *f* values, dipole moments, and all that," Am. J. Phys., Vol. 50, No. 11, pp. 982-986, Nov. 1982.

Hindmarsh, W. R. and Thomas, K. A., "Collision Broadening in the Argon Spectrum," Proc. Phys. Soc., A 77, pp. 1193-96, 1961.

Jenkins, D. B., "Oscillator Strength of the 130 nm OI Triplet," J. Quant. Spectrosc. Radiat. Transfer, Vol. 34, No. 1, pp. 55-58, 1985.

Kastler, A., "Optical Methods For the Study of Radio-Frequency Resonances," Physics Today, pp. 34-41, Sept. 1967.

Kielkopf, J., "The Lyman-alpha Wing," Spectral Line Shapes, Vol. 7, Proc. Eleventh International Conference, Carry le Rouet, France, June, 1992.

King, G. W. and Van Vleck, J. H., "Dipole-Dipole Resonance Forces," Phys. Rev., Vol. 55, pp. 1165-72, June 1939.

Konjevic, N. and Roberts, J. R., "A Critical Review of the Stark Widths and Shifts of Spectral Lines from Non-Hydrogenic Atoms," J. Phys. Chem. Ref. Data, Vol. 5, No. 2, pp. 209-253, 1976.

Kuhn, H. G. and Lewis, E. L., "Resonance Broadening of Spectral Lines," in Polarisation Matiére et Rayonnement, pp. 341-356. Presses Universitaires de France, Paris, France, 1969.

Lee, L. C., Slanger, T. G., Black, G., and Sharpless, R. L., "Quantum Yields for the Production of $O(^1D)$ From Photodissociation of O_2 at 1160-1770 Å," J. Chem. Phys., Vol. 62, No. 12, pp. 5602-06, Dec. 1977.

Li, Y., Honigmann, M., Bhanuprakash, K., Hirsch, G., Buenker, R. J., Dillon, M. A., and Kimura, M., "Coupled Diabatic Configuration Interaction Treatment of the O_2 B'-X Transition Including Computation of Predissociation Linewidths, Optical f Values, and Generalized Oscillator Strengths," J. Chem. Phys., Vol. 96, No. 11, pp. 8314-23, June 1992.

Liu, Y., Shakib, F. and Vinokur, M., "A Comparison of Internal Energy Calculation Methods for Diatomic Molecules," Phys. Fluids A, Vol. 2, No. 10, Oct. 1990, pp. 1884-1902.

Loree, T. R., Sze, R. C., Barker, D. L., and Scott, P. B., "New Lines in the UV: SRS of Excimer Laser Wavelengths, IEEE Journal of Quantum Electronics, Vol. QE-15, No. 5, pp. 337-342, May, 1979.

Margenau, H. and Watson, W. W., "Pressure Effects on Spectral Lines," Rev. Mod. Phys., Vol. 8, pp. 22-53, Jan. 1936.

Margenau, H. and Kestner, N. R., Theory of Intermolecular Forces, 2nd ed. Chapter 2, Pergamon Press, New York, 1971.

Milton, B. E. and Dannenberg, R. E., "Optimized Performance of Arc Heated Shock Tubes," Proceedings of the 14th International Symposium on Shock Tubes and Waves, New South Wales, Australia, 1983.

Minck, R. W. Terhune, R. W. and Rado, W. G., "Laser-stimulated Raman Effect and Resonant Four-photon Interaction in Gases H_2, D_2, and CH_4," Appl. Phys. Letters, Vol. 3, No. 10, pp. 181-183, Nov. 1963.

Mirels, H., "Correlation Formulas for Laminar Shock Tube Boundary Layer," Phys. Fluids, Vol. 9, No. 7, pp. 1265-1272, July, 1966.

Mirels, H, "Boundary Layer Growth Effects in Shock Tubes," Proceedings of the 8th International Shock Tube Symposium, ed. Stollery, J. L., Gaydon, A. G., and Owen, P. R., Chapman and Hall, London, England, 1971.

Miziolek, A. W. and DeWilde, M. A., "Multiphoton photochemical and collisional effects during oxygen-atom flame detection," Optics Letters, Vol. 9, No. 9, pp. 390-392, Sept. 1984.

Moore, C. E., "Tables of spectra of hydrogen, carbon, nitrogen, and oxygen atoms and ions," pp. 204, 212, CRC Press, Boca Raton, Florida, 1993.

Niemax, K., and Pichler, G., "Asymmetric self-broadening of Cs principal lines," J. Phys. B: Atom. Molec. Phys., Vol. 7, No. 10, pp. 1204-13, 1974.

Niemax, K., and Pichler, G., "New aspects in the self-broadening of alkali resonance lines," J. Phys. B: Atom. Molec. Phys., Vol. 8, No. 2, pp. 179-184, 1975.

Ogawa, S., and Ogawa, M., "Absorption Cross Sections of O_2 ($a^1\Delta_g$) and O_2 ($X^3\Sigma_g^-$) in the Region from 1087 to 1700 Å," Can. J. Phys., Vol. 53, pp. 1845-52, 1975.

Pamidimukkala, K. M., Lifshitz, A., Skinner, G. B., and Wood, D. R., "Resonance absorption measurements of atom concentrations in reacting gas mixtures. VI. Shapes of the vacuum ultraviolet oxygen (^3S-^3P) resonance triplet from microwave sources and empirical calibration in a shock tube," J. Chem. Phys., Vol. 75, No. 3, pp. 1116-1122, Aug. 1981.

Park, C., Nonequilibrium Air Radiation (NEQAIR) Program: User's Manual. NASA TM-86707, 1985. (see also Park, C., "Calculation of Nonequilibrium Radiation in the Flight Regimes of Aeroassisted Orbital Transfer Vehicles," *Thermal Design of Aeroassisted Orbital Transfer Vehicles*, edited by H. F. Nelson, Vol. 96, Progress in Astronautics and Aeronautics, AIAA, New York, 1985, pp. 395-418.)

Patterson, P. M., Sutherland, J. W., and Klemm, R. B., "High Temperature Study of the Reaction of $O(^3P) + NH_3$," Proceedings of the17th International Symposium on Shock Tubes and Waves, pp. 444-449, 1989.

Peach, G., "Unified theories of the pressure broadening and shift of spectral lines: 1. General formulation for multipole interactions," J. Phys. B: Mol. Phys., Vol. 17, pp. 2599-2618, 1984.

Saxon, R. P. and Liu, B., "*Ab initio* configuration intertaction study of the valence states of O_2," J. Chem. Phys., Vol. 67, No. 12, pp. 5432-41, Dec. 1977.

Saxon, R. P. and Liu, B., "*Ab initio* configuration intertaction study of the Rydberg states of O_2," J. Chem. Phys., Vol. 73, No. 2, pp. 870-880, July 1980.

Sharma, S. P., Park, C., and Dannenberg, R. E., "Operating Characteristics of a 60 cm and a 10 cm Electric Arc-driven Shock Tube," AIAA-88-0142, 26th Aerospace Sciences Meeting, Reno, NV, Jan. 11-14, 1988.

Sharma, S. P., and Whiting, E. E., "Modeling of Nonequilibrium Radiation Phenomena: An Assessment," AIAA paper 94-0253, Reno, NV, Jan. 1994.

Smith, W. C., Leiweke, R. J., and Beeson, H., "Response of a Piezoelectric Pressure Transducer to IR Laser Beam Impingement," Instrument Society of America #92-0211, 1992.

Snelling, D. R., Smallwood, G. J.; Sawchuk, R.A, "Nonlinearity and Image Persistence of P-20 Phosphor-based Intensified Photodiode Array Detectors Used in CARS Spectroscopy," Appl. Opt., Vol. 28, No. 15, pp. 3226-32, Aug. 1989.

Sohns, E. and Kock, M., "Plasma Diagnostics Based On Self-reversed Lines - II. Application to Nitrogen, Carbon, and Oxygen Arc Measurements in the Vacuum Ultraviolet," J. Quant. Spectrosc. Radiat. Transfer, Vol. 47, No. 5, pp. 335-343, 1992.

Teets, R. E. and Bechtel, J. H., "Coherent anti-Stokes Raman spectra of oxygen atoms in flames," Optics Letters, Vol. 6, No. 10, pp. 458-460, Oct. 1981.

Traving, G., "Interpretation of Line Broadening and Shift" in Plasma Diagnostics, ed. Lochte-Holtgreven, W., Wiley Interscience Division, John Wiley and Sons, New York, 1968.

Wang, J., McCoy, D. G., Blake, A. J., and Torop, L., "Effects of the Close Approach of Potential Curves in Photoabsorption by Diatomic Molecules. II. Temperature Dependence of the O_2 Cross-section in the Region 130-160 nm," J. Quant. Spectrosc. Radiat. Transfer, Vol. 38, No. 1, pp. 19-27, 1987.

Westblom, U., Agrup, S., Aldén, M., Hertz, H. M., and Goldsmith, J. E. M., "Properties of Laser-Induced Stimulated Emission for Diagnostic Purposes," Appl. Phys. B, Vol. 50, pp. 487-497, Dec. 1990.

Whiting, E. E., and Park, C., "Radiative Heating at the Stagnation Point of the AFE Vehicle," NASA TM-102829, Nov. 1990.

Wiese, W. L., Smith, M. W., and Glennon, B. M., National Bureau of Standards NSRDS-NBS 4, Vol. 1, 1966.

Wilke, V. and Schmidt, W., "Tunable Coherent Radiation Source Covering a Spectral Range from 185 to 880 nm," Appl. Phys., Vol. 18, pp. 177-181, 1979.

Williams, M. W. and Arakawa, E. T., "Optical properties of crystalline MgF_2 from 115 nm to 400 nm," Appl. Optics, Vol. 18, No. 10, pp. 1477-78, May 1979.

Wilson, G. J., "Numerical Simulation of High Enthalpy Impulse Facilities," *Proceedings of the 20th International Symposium on Shock Waves*, Pasadena, CA, 1995. In press.

Yoshimine, M., Tanaka, K., Tatewaki, H., Obara, S., Sasaki, F, and Ohno, K, "The Second $^3\Sigma_u^-$ State of O_2," J. Chem. Phys., Vol. 64, No. 5, pp. 2254-55, Mar. 1976.

Yoshino, K., Freeman, D. E. and Parkinson, W. H., "Atlas of the Schumann-Runge Absorption Bands of O_2 in the Wavelength Region 175-205 nm," J. Phys. Chem. Ref. Data, Vol. 13, No. 1, 1984.